

**MAX PLANCK INSTITUTE**  
FOR DYNAMICS AND  
SELF-ORGANIZATION



JOSÉ-AGUSTÍN ARGUEDAS-LEIVA

---

---

Physical modeling of motile and  
sedimenting plankton: from simple  
flows to turbulence

---

---

DISSERTATION





# Physical modeling of motile and sedimenting plankton: from simple flows to turbulence

## Dissertation

for the award of the degree  
"Doctor rerum naturalium"  
of the Georg-August-Universität Göttingen

within the Physics doctoral program  
of the Faculty of Physics  
of the Georg-August University School of Science (GAUSS)

submitted by

**José–Agustín Arguedas–Leiva**

from San José, Costa Rica  
Göttingen, 2022

Thesis advisory committee:

**Prof. Dr. Michael Wilczek**

Max Planck Research Group Turbulence, Complex Flows and Active Matter,  
Max Planck Institute for Dynamics and Self-Organization  
Department of Physics, University of Bayreuth

**Prof. Dr. Andreas Tilgner**

Institute of Astrophysics and Geophysics,  
Faculty of Physics, University of Göttingen

**Prof. Dr. Ramin Golestanian**

Department of Living Matter Physics,  
Max Planck Institute for Dynamics and Self-Organization

Members of the examination board:

**Referee: Prof. Dr. Michael Wilczek**

Max Planck Research Group Turbulence, Complex Flows and Active Matter,  
Max Planck Institute for Dynamics and Self-Organization  
Department of Physics, University of Bayreuth

**2<sup>nd</sup> Referee: Prof. Dr. Andreas Tilgner**

Institute of Astrophysics and Geophysics,  
Faculty of Physics, University of Göttingen

Further members of the examination board:

**Prof. Dr. Ramin Golestanian**

Department of Living Matter Physics,  
Max Planck Institute for Dynamics and Self-Organization

**Prof. Dr. Stefan Klumpp**

Institute for the Dynamics of Complex Systems,  
Faculty of Physics, University of Göttingen

**PD Dr. Olga Shishkina**

Max Planck Research Group Theory of Turbulent Convection,  
Max Planck Institute for Dynamics and Self-Organization

**Dr. David Zwicker**

Max Planck Research Group Theory of Biological Fluids,  
Max Planck Institute for Dynamics and Self-Organization

**Date of oral examination:** 16 May 2022



# Abstract

Planktonic microorganisms play a fundamental role in oceanic ecology and chemical cycles. Different planktonic species are found at various levels of the oceanic trophic chain, ranging from photosynthetic organisms to grazing species higher in the food chain. Many planktonic species have developed migration strategies to aid their survival. This includes motility and density regulation. Physical aspects, such as transport and collision rates, have a direct impact on planktonic survival and are influenced by the planktonic migration strategies. Furthermore, collision rates between planktonic organisms also play an important role in the formation of macroscopic plankton blooms. These have a direct effect on the ecology of oceans and lakes. In this dissertation we use physical modeling to study motile and sedimenting microorganisms in a fluid flow. We aim at shedding light on the key features of microorganism dynamics in fluid flows as a function of their key parameters: shape, motility, and density offset.

In chapter 1 we introduce the biological setting of plankton, and give a very brief overview of the physical modeling approaches for plankton in fluid flows. Subsequently in chapter 2 we introduce the theoretical framework of turbulence and the methodology of our numerical simulations.

In chapter 3 we start by examining microswimmers in a simple two-dimensional toy-model. We use methods from dynamical systems theory to uncover the role played by shape and motility in determining the microorganism dynamics in this simple setting. We explicitly identify the Hamiltonian dynamics followed by spherical microswimmers. Additionally, we find that elongated microswimmers more easily escape simple vortex structures than other shapes.

In chapter 4 we then move on to ellipsoidal microswimmers in realistic mild turbulent flows. We analyze transport and rotation rates of motile ellipsoids. We find that elongated microswimmers have an advantage in transport, which is in part due to shape-dependent rotation rates. We also investigated the collision rates of motile spheres, and we were able to extract a master curve interpolating between the passive and motile limits for different sized spheres. We quantified the effect of motility and found that even very small motility greatly enhances collision rates.

In chapter 5 we study of sedimentation of elongated microorganisms in mild turbulence. We measure the collision rates of elongated microorganisms in terms of size, energy dissipation rate, and aspect ratio. We then find a master curve interpolating between a passive particle and a sedimentation dominated limit. We characterize the role played by shape, which increases collision rates of elongated microorganisms in comparison with equal-volume spheres. This shape-induced enhancement helps to explain the timescales for formation of blooms of elongated planktonic species.

In summary, in this dissertation we study the effect of shape, motility, and density regulation on physical models of planktonic microorganisms. Our findings help to shed light on the interplay between these planktonic parameters, the role of oceanic turbulence, and biologically

relevant physical measures, such as transport, collision rates, and planktonic bloom formation times.

# Contents

<b>Abstract</b>	<b>ii</b>
<b>Contents</b>	<b>iv</b>
<b>1 Introduction</b>	<b>2</b>
<b>2 Theory and Methods</b>	<b>6</b>
2.1 Turbulent flows . . . . .	6
2.2 Particles in turbulence . . . . .	11
2.3 Particle collisions . . . . .	14
2.4 Ghost collision algorithms . . . . .	15
2.5 Details on numerical simulations . . . . .	17
<b>I Manuscript I</b>	<b>21</b>
<b>3 Microswimmers in an axisymmetric vortex flow</b>	<b>22</b>
3.1 Microswimmers in a vortex flow . . . . .	25
3.2 Fixed-point analysis . . . . .	28
3.3 Hamiltonian dynamics and phase-space contraction . . . . .	30
3.4 Impact of rotational noise . . . . .	33
3.5 Summary and conclusions . . . . .	35
<b>II Dispersion and collision of motile ellipsoids</b>	<b>37</b>
<b>4 Dispersion and collision of motile ellipsoids</b>	<b>38</b>
4.1 Introduction . . . . .	38
4.2 Theory and methods . . . . .	40
4.3 Rotation statistics . . . . .	45
4.4 Dispersion statistics . . . . .	47
4.5 Collision rates . . . . .	53
4.6 Discussion . . . . .	56
<b>III Manuscript II</b>	<b>57</b>
<b>5 Elongation enhances encounter rates between phytoplankton in turbulence</b>	<b>58</b>

5.1 Supporting information . . . . .	66
<b>IV Conclusions</b>	<b>75</b>
<b>6 Summary &amp; discussion</b>	<b>76</b>
<b>V Appendix</b>	<b>79</b>
<b>A A minimal model for turbulent intermittency</b>	<b>80</b>
A.1 Introduction. . . . .	81
A.2 The model . . . . .	84
A.3 Numerical results on real-space and phase dynamics & statistics. . . . .	85
A.4 Synchronization. . . . .	87
A.5 Chaos characterization. . . . .	87
A.6 Conclusions. . . . .	89
<b>B Shape- and scale-dependent spheroid rotations rates</b>	<b>90</b>
B.1 Introduction . . . . .	91
B.2 Direct numerical simulations . . . . .	93
B.3 Discussion . . . . .	99
<b>Backmatter</b>	<b>101</b>
<b>Bibliography</b>	<b>102</b>





# Introduction

Microscopic organisms are an integral part of the oceanic ecosystem [1, 2]. Phytoplankton, for example, are photosynthetic planktonic microorganisms that absorb nutrients and solar energy to grow and multiply [3]. These small organisms form the base of the oceanic food chain. A vast and complex trophic web of grazing microorganisms (see figure 1.1), called zooplankton, then carries nutrients up to the level of macroscopic organisms, such as fish, birds, and whales. This collection of microscopic organisms plays a critical role in the carbon cycle of the ocean [4], photosynthesizing basic chemicals into usable nutrients for higher trophic levels. Within this picture, different planktonic species have developed migration strategies to maximize their survival.

Phytoplankton can generate their own food by means of photosynthesis, and their survival greatly depends on being in nutrient rich regions and having access to sunlight. Some species do this by regulating their buoyancy and sinking during night to nutrient rich waters, while surfacing during the day to carry out photosynthesis. Zooplankton are predatory and in order



Figure 1.1: Plankton are microscopic organisms present in the ocean. They are an integral part of the oceanic food chain and chemical cycles. These microorganisms come in a wide spectrum of shapes, sizes, and have a variety of mechanistic strategies to maximize their survivability, for example motility and sedimentation. Taken from [5].

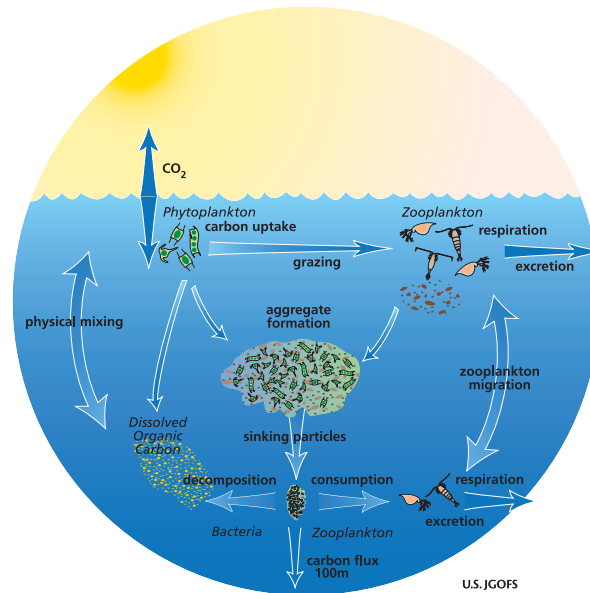


Figure 1.2: The microscopic oceanic ecosystem is complex and plays a fundamental role in the oceanic chemical cycles and trophic chain. Within this complex picture the turbulent oceanic medium induces physical mixing. Additionally, many planktonic species have developed migration strategies, such as motility and buoyancy regulation, as a survival strategy. Physical properties, such as transport and collision rates, as a function of the migration strategies splay a crucial role in determining plankton survival in the ocean. Taken from [7].

to survive they need to graze, mate and evade predation. Therefore some zooplankton species have developed motility as a transport mechanism to improve their survival. This complex interplay between planktonic organisms, migration strategies, and the turbulent oceanic medium is sketched in figure 1.2. Mechanistic migration strategies are present at various trophic levels [6], and a great part of the survivability of these plankton species depends on physical properties of the microorganisms in the flow, such as transport and collision rates. Studying these physical properties of microorganisms in an oceanic turbulent medium is therefore an important step at understanding the complex and vital role plankton play in the oceanic ecosystem. Another tangible way in which planktonic organisms affect the oceanic ecosystem is through bloom formation.

Planktonic blooms are events in which temperature and nutrient conditions favor the exponential growth of planktonic population [1]. Some plankton blooms are seasonal [8], while others are driven by oceanic nutrient excess due to human activity [9]. These blooms can grow to macroscopic sizes even visible from space, such as in figure 1.3. The exponential growth of the bloom is eventually halted, either by nutrient depletion, or by such a dense plankton population that the water becomes dark and sunlight no longer penetrates into the water. When the photosynthetic microorganisms die, oxygen is eventually depleted. This is because on the one hand the photosynthetic organisms suffer a catastrophic death, and on the other hand the bacteria that decompose these dead phytoplankton consume oxygen. The bloom then creates a hypoxic dead zone in the ocean in which biotic organisms cannot survive. Plankton blooms then play a fundamental role not only in the oceanic ecosystem but also in human economic activities, such as fisheries by creating dead zones and depleting fish populations.

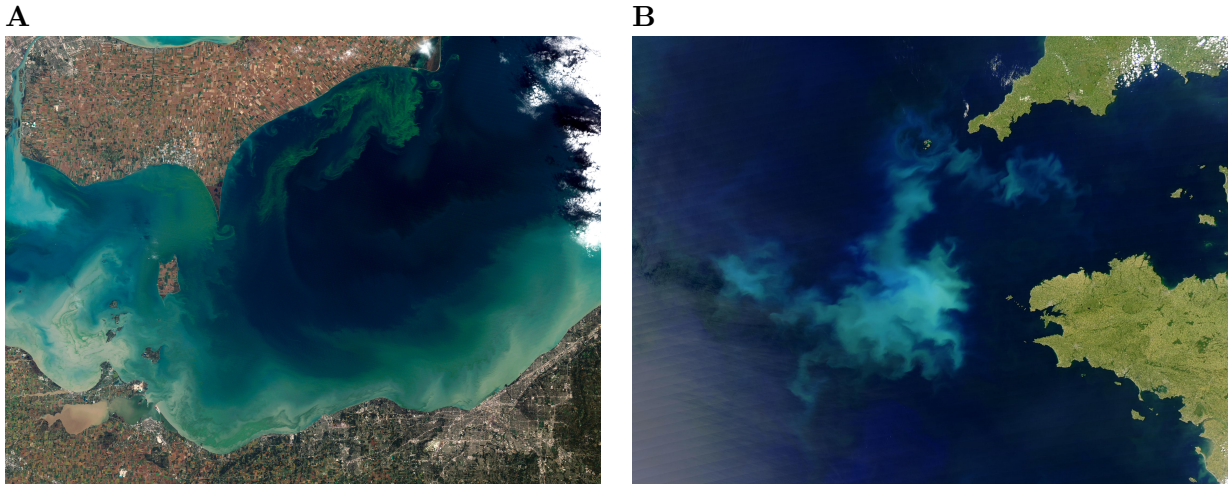


Figure 1.3: Under certain circumstances planktonic organisms can bloom, and grow exponentially in the ocean. These bloom are eventually halted, and lead to oxygen depletion, further impacting oceanic ecosystems. Explaining the generation of plankton bloom requires a complex interplay between biological, environmental, and physical factors. A mechanistic approach helps to better understand the interplay between planktonic migration strategies, and fluid flow properties of the oceanic turbulent medium, leading to bloom formation. **A** A bloom in Lake Erie due to fertilizer inflow and nutrient excess in the water. Taken from [10]. **B** A spring bloom of coccolithophores in the Celtic Sea off the coast of Brittany. Taken from [11].

Plankton survival as a function of migration strategies, as well as the process and mechanisms for the generation of a plankton blooms are still active research questions. A complex interplay between external factors, such as nutrient input, temperature, ocean turbulence, as well as planktonic factors, such as biological behavior, locally present species, and plankton transport strategies, all play a role [12, 13]. Analyzing this whole complex picture is a difficult endeavor, which spans several disciplines. In this dissertation, we will concentrate on the basic physical mechanisms to model microorganisms in oceanic turbulence on the order of tens of centimeters to meters. Studying these models might help to better understand how the relation between planktonic microorganisms and turbulent flows affects plankton surviveability in terms of transport and collision rates, as well as how this leads to phenomena such as planktonic blooms.

To better understand microorganisms in a turbulent oceanic medium, scientists have devised simplified modeling approaches [14, 15] to understand and quantify planktonic phenomena. We concentrate in models, in which a turbulent background flow  $\mathbf{u}$  advects the microorganisms, which are modeled as non-inertial particles. Furthermore, apart from the survival migration strategies of motility and buoyancy regulation, the microorganism shape is also a critical parameter, as it determines how the flow rotates and spins the organisms around. A glimpse at figure 1.1 reveals the variety of shape and sizes of planktonic organisms. By focusing on the case of small organisms and approximating their shape as ellipsoidal, the spinning and rotation induced by the turbulent medium on these microorganisms can be modeled by use of

the Jeffery's equations [16]. These modeling approaches then have the generic form

$$\dot{\mathbf{x}} = \mathbf{u} + \mathbf{f}(\hat{\mathbf{p}}), \quad (1.1)$$

$$\dot{\hat{\mathbf{p}}} = \frac{1}{2}\boldsymbol{\omega} \times \hat{\mathbf{p}} + \alpha \left( \mathbf{S}\hat{\mathbf{p}} - \hat{\mathbf{p}}^T \mathbf{S}\hat{\mathbf{p}} \hat{\mathbf{p}} \right) + \mathbf{g}(\hat{\mathbf{p}}). \quad (1.2)$$

Here  $\mathbf{x}$  is the microorganism position,  $\alpha$  parametrizes the shape of the ellipsoid, and  $\hat{\mathbf{p}}$  is the ellipsoid's orientation. The fluid vorticity  $\boldsymbol{\omega}$  and strain rate  $\mathbf{S}$  rotate and spin the microorganisms. Furthermore, migration strategies depending on the microorganism orientation can be modeled by the term  $\mathbf{f}(\hat{\mathbf{p}})$ . The term  $\mathbf{g}(\hat{\mathbf{p}})$  can be used to introduce preferential orientation (such as gravity) or orientational stochastic terms. This modeling approach has been used to study several migration strategies, such as self-propulsion (motility) [17–24], buoyancy regulation (sedimentation) [25–31], and gravity oriented motility (gyrotaxis) [15, 19, 24, 32–40]. In this dissertation we will limit ourselves to the study of motility and sedimentation. We will study the mathematical properties of motile microorganisms in a two-dimensional toy-model. Afterwards we will move on to realistic turbulence and measure microswimmer transport and collision properties in mild turbulence. We then will turn our attention the problem of sedimentation of slim microorganisms in the ocean, and tackle the question of bloom formation of thin elongated planktonic species.

## Thesis outline

This dissertation is structured as follows. In chapter 2 we will introduce the theoretical framework which our physical models are based on, as well as details regarding the implementation in simulation code. In chapter 3 we will study a modeling approach of motile microorganisms in a two-dimensional toy-model setting. In this toy-model setting, we will analytically explore the properties of the pertinent equations as a function of shape and motility. Subsequently, in chapter 4 we make the jump from a two-dimensional toy-model to a turbulent medium. By use of direct numerical simulations, we systematically study the transport and rotation properties of motile microorganisms in mild turbulence as a function of shape and motility. We will also study the effect of motility and particle size in collision rates of motile spherical particles.

In chapter 5 we then switch our approach and instead of motility study microorganisms with a density mismatch to the surrounding fluid. More specifically, we look at sedimenting elongated microorganisms in mild turbulence, and relate the effect of turbulence intensity and density offset, to collision rates and subsequently to the timescales pertinent to plankton bloom formation.

Finally, in the appendix 6 we present two manuscripts that formed part of the research carried out during my time as doctoral researcher, but which are not directly related to the central topic of this dissertation.

# Theory and Methods

In this chapter we will introduce the theoretical framework relevant for the topics of this dissertation: turbulence and particles in turbulent flows. We will first introduce the Navier-Stokes equations as the underlying equations of a turbulent flow. Subsequently we will characterize the different length and time scales present in fluid flows via a small excursion into the statistical theory of turbulence. We will then consider particles embedded in a fluid flow, starting with non-inertial Lagrangian particles, and then going on to more general equations of motion, where particle shape is taken into account. As a next step we will introduce collision rates and the corresponding criteria for quantifying what constitutes a particle collision. Finally, we will discuss details regarding the numerical simulations of the turbulent flow and the rotational dynamics of particles in the flow.

We refer to classical textbooks for more thorough and detailed presentation of the theory of turbulent flows [41–44].

## 2.1 Turbulent flows

### 2.1.1 Navier-Stokes equations

Fluid flows appear in a variety of physical settings. The motion of viscous fluid flow is captured by the velocity field  $\mathbf{u} = \mathbf{u}(\mathbf{x}, t)$ , which is a function of position  $\mathbf{x}$  and time  $t$ . The time evolution of the velocity field is governed by the Navier-Stokes equations [41]. In the case of liquids, the flow is usually incompressible. That is, density differences are negligible. The incompressible Navier-Stokes equations then take the form of a momentum equation and an incompressibility condition

$$\frac{\partial \mathbf{u}}{\partial t} + \mathbf{u} \cdot \nabla \mathbf{u} = -\nabla p + \nu \Delta \mathbf{u} + \mathbf{f}, \quad (2.1)$$

$$\nabla \cdot \mathbf{u} = 0. \quad (2.2)$$

Here  $p$  denotes the kinematic pressure,  $\nu$  is the kinematic viscosity, and  $\mathbf{f}$  is a generic term accounting for forcing or external forces. In this dissertation  $\mathbf{f}$  will always be a pure large-scale isotropic forcing term, as we will not take into account any other external forces acting on the flow. Without the forcing term, the dissipation term  $\nu \Delta \mathbf{u}$  will eventually dissipate

all the energy contained in the flow  $\mathbf{u}$ , leading to a quiescent flow solution ( $\mathbf{u} = 0$ ) at long times. We hence include a large scale forcing  $\mathbf{f}$  to obtain a statistically stationary velocity field. Additionally, the pressure term  $p$  is a non-local term [41], enforcing incompressibility (2.2) in the momentum equation (2.1).

Consider now typical velocity and length scales of a given flow  $\mathbf{u}$  given by  $U$  and  $L$ , respectively. Using these length scales we can rescale the physical variables of equations (2.1)-(2.4) as  $\mathbf{u} \rightarrow \mathbf{u}' U$ ,  $\mathbf{x} \rightarrow \mathbf{x}' L$ ,  $\mathbf{f} \rightarrow \mathbf{f}' U^2/L$ ,  $t \rightarrow t' L/U$ , and  $p \rightarrow p' U^2$ . These new primed quantities are non-dimensional. Dropping the tildes we can rewrite (2.1) and (2.2) in non-dimensional form as

$$\frac{\partial \mathbf{u}}{\partial t} + \mathbf{u} \cdot \nabla \mathbf{u} = -\nabla p + \frac{1}{\text{Re}} \Delta \mathbf{u} + \mathbf{f}, \quad (2.3)$$

$$\nabla \cdot \mathbf{u} = 0. \quad (2.4)$$

Here we have obtained  $\text{Re}$ , the so-called Reynolds number. It is a non-dimensional quantity defined as

$$\text{Re} \equiv \frac{UL}{\nu}. \quad (2.5)$$

The Reynolds number describes the ratio between the typical scales of the flow (inertial scales), and the scales at which viscous dissipation becomes important. Hence a flow with a small Reynolds number is said to be highly viscous, as the viscous term is important. On the other extreme, a large Reynolds number flow is said to be turbulent. This means that there is an appreciable separation between the typical scales of the flow, and the scales at which viscosity becomes important. This large separation allows for the energy to be transferred from the forcing at the large scales, then by inertial transport as kinetic energy down to the smallest scales of the flow, where it is finally dissipated. This picture is known as the cascade picture of turbulence. In order to better understand this picture we will now take a look at the statistical theory of turbulence. This will allow us to more formally define the different length scales at play in a turbulent flow, and precisely describe what is meant by this cascade picture.

### 2.1.2 Statistical theory of turbulence

The velocity field of a turbulent flow  $\mathbf{u}$  following the Navier-Stokes equations (2.3) is chaotic, and as such a statistical approach is adequate. We consider flows with forcing and boundary conditions such that the flow statistics are homogeneous and isotropic.

In order to better understand the dynamics of the fluid flow, we will look at the dynamics of energy in the flow, from where it is pumped into the flow by the forcing, up to its dissipation at the smallest scales. The classical picture of an energy cascade was introduced by Richardson [45] in 1922. According to this picture energy is input at the large scales of a fluid flow. This may be, for example, wind over the ocean. The flow acquires speed from the forcing. There is then an energy transfer from the external forcing into kinetic energy contained in the fluid flow  $\mathbf{u}$ . The kinetic energy is then transferred from length scale to length scale. The kinetic energy is eventually transferred to scales at which viscosity becomes important. Viscosity then dissipates energy in the form of microscopic heat.

In the cascade picture there are three important ranges of length scales. First of all, the largest scales, which are induced by the large scale forcing. Then the inertial range: a range of scales in which energy is transferred in form of kinetic energy from length scale to length scale onto the smaller length scales. Finally the smallest scales of the flow denote the length scales at

which viscosity starts to become important and eventually dominates. We will now introduce the two-point correlation function as a formal way to define these different length scales.

### Two-point correlation function

At a given time  $t$  a velocity field  $\mathbf{u}$  decorrelates in space. The simplest statistical quantity containing information on spatial structure is the two-point correlation function. This is a direct way to measure spatial statistics, and it will help us to formally define length scales in a turbulent flow. In a homogeneous flow, the (equal time) two-point correlation is defined as

$$R_{ij}(\mathbf{r}, t) \equiv \langle u_i(\mathbf{x} + \mathbf{r}, t) u_j(\mathbf{x}, t) \rangle, \quad (2.6)$$

where the brackets indicate volume averaging (average over  $\mathbf{x}$ ). At zero separation  $|\mathbf{r}| = 0$  we get  $R_{ij}(0, t) = u_{\text{rms}}^2/3$ , where  $u_{\text{rms}} = \sqrt{\langle \mathbf{u}^2 \rangle}$ . In a statistically isotropic flow,  $R_{ij}$  can be recast as a contribution from the transverse and longitudinal directions of  $\mathbf{r}$ . This yields the two-point correlation as

$$R_{ij}(\mathbf{r}, t) = \frac{u_{\text{rms}}^2}{3} \left( g(r, t) \delta_{ij} + [f(r, t) - g(r, t)] \frac{r_i r_j}{r^2} \right) \quad (2.7)$$

where  $r := |\mathbf{r}|$  is the distance. The two-point correlation then has explicit contributions from a longitudinal autocorrelation function  $f$ , and a transverse autocorrelation function  $g$ . These functions have the property that  $f(0, t) = g(0, t) = 1$ . In three-dimensional isotropic turbulence it can be shown that  $g$  depends on  $f$  through

$$g(r, t) = f(r, t) + \frac{r}{2} \frac{\partial f(r, t)}{\partial r}. \quad (2.8)$$

Hence, the two-point correlation function and all derived quantities can be expressed in terms of  $f$ . The explicit expressions for  $g$  in the rest of this section can be readily worked out [41]. However, for simplicity, in the following we will express all relevant quantities using  $f$ .

### Large length scales: integral length

In a turbulent flow, certain regions with a given size may show turbulent structures with some coherence. These turbulent coherent regions are called eddies, and typically have a vortex structure of a given length scale [43]. Eddies are found at all length scales in a turbulent flow. The largest eddies are then the largest turbulent coherent structures in a turbulent flow. These large length scales may be taken as the typical large scales of the flow. A way of defining the size of these largest coherent structures is by use of the autocorrelation function  $f$ .

The typical length of the autocorrelation function  $L_{\text{int}}$  can be obtained by integrating over it. That is,

$$L_{\text{int}}(t) := \int_0^\infty dr f(r, t). \quad (2.9)$$

This integral length is a statistical quantity. Presuming exponentially decaying tails, it tells us after which distance the flow decorrelates. That is, the integral length characterizes the length scales of the largest eddies in the flow.

### Kolmogorov similarity hypotheses

In his seminal work in 1941 [46, 47] Kolmogorov proposed two similarity hypotheses for turbulent flows at high Reynolds numbers. Using dimensional analysis, Kolmogorov's first similarity hypothesis pertains the statistics at the small scales of a turbulent flow, and it can be rephrased as follows:

**First similarity hypothesis:** At high enough Reynolds numbers the small-scale turbulent statistics have a universal form depending only on  $\nu$  and  $\varepsilon$ .

Here  $\varepsilon$  is the kinetic energy dissipation rate, which is defined as

$$\varepsilon = 2\nu \langle S_{ij}S_{ij} \rangle \quad (2.10)$$

Here  $S$  is the strain rate tensor, that is, the symmetric part of the velocity gradient tensor

$$S_{ij} = \frac{1}{2} \left( \frac{\partial u_i}{\partial x_j} + \frac{\partial u_j}{\partial x_i} \right). \quad (2.11)$$

The kinetic energy dissipation rate  $\varepsilon$  then accounts for the total energy dissipated by viscous forces. In isotropic turbulence  $\varepsilon$  can be recast as [41]

$$\varepsilon = 15 \nu \left\langle \left( \frac{\partial u_x}{\partial x} \right)^2 \right\rangle. \quad (2.12)$$

Kolmogorov also proposed a second similarity hypothesis pertaining the inertial range. This second hypothesis can be expressed as follows:

**Second similarity hypothesis:** At high enough Reynolds numbers the statistics of turbulent motion in the inertial range have a universal form depending only on  $\varepsilon$  and not on  $\nu$ .

### Kolmogorov microscales

At the smallest scale viscosity dissipates kinetic energy into heat. Using Kolmogorov's first similarity hypothesis we will derive the so-called Kolmogorov microscales, which characterize the smallest scales of the flow in which viscosity starts to dominate. Using combinations of  $\nu$  and  $\varepsilon$  we can form length, time, and velocity quantities

$$\eta = \left( \frac{\nu^3}{\varepsilon} \right)^{1/4}, \quad \tau_\eta = \left( \frac{\nu}{\varepsilon} \right)^{1/2}, \quad u_\eta = (\nu\varepsilon)^{1/4}. \quad (2.13)$$

These microscales characterize the scales at which viscous forces become comparable to the inertial. A way to see this is by calculating the typical Reynolds numbers  $\text{Re}_\eta$  at these scales

$$\text{Re}_\eta = \frac{u_\eta \eta}{\nu} = 1. \quad (2.14)$$

A Reynolds numbers of unity means that these scales characterize the small scales of the fluid.

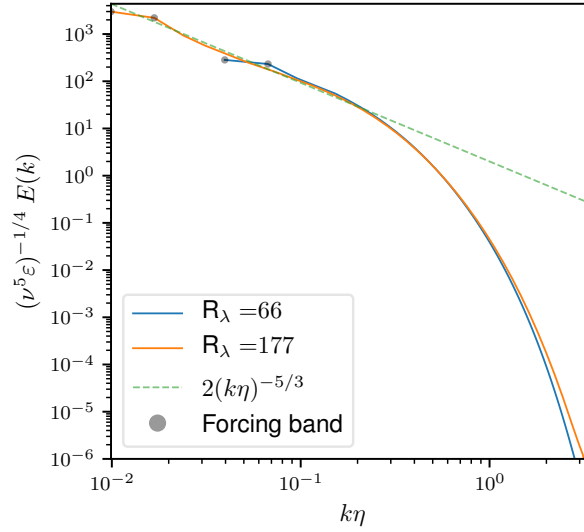


Figure 2.1: Here we show the energy spectrum from two simulations. The energy spectrum  $E(k)$  of a turbulent flow shows the energy contained in structures of typical length  $l = 2\pi k$ . Energy is input at the forcing band, and then transferred from larger to smaller eddies in the flow. Eventually viscous forces dominate at the large wave number regime (small length scales), and energy is dissipated. The Reynolds number  $R_\lambda$  is a measure of the separation between the large and the small scales of the flow, i.e. a measure of the turbulence intensity. A turbulent flow with larger Reynolds number has a broader inertial range. The slight departure at the deep dissipative range (large  $k\eta$ ) can be related to dependence on Reynolds number [48].

### Energy spectrum of the inertial range

Kolmogorov's second similarity hypothesis can be used to predict the energy spectrum in the inertial range. The energy spectrum is a function of the wavenumber  $k = l/2\pi$ , and it displays the kinetic energy contained structures of the length scale  $l$ . Then the kinetic energy spectrum can be expressed as

$$E(k) = \frac{1}{2} \oint d\Omega(k) \frac{1}{(2\pi)^3} \int d\mathbf{x} R_{jj}(\mathbf{x}) e^{-i\mathbf{k}\cdot\mathbf{x}}, \quad (2.15)$$

where  $d\Omega(k)$  is a spherical differential surface element at radius  $k$ , and  $\oint d\Omega(k)$  is an integral over a spherical shell of radius  $k = |\mathbf{k}|$ . Then, the quantity  $E(k)dk$  is the kinetic energy contained between  $k$  and  $k+dk$  and has units of velocity squared. Kolmogorov's second similarity hypothesis [41, 46] can be used to derive the following scaling law

$$E(k) = C \varepsilon^{2/3} k^{-5/3}, \quad (2.16)$$

where  $C$  is a universal constant. This is known as the 5/3-law, and is one of the most celebrated results of the statistical theory of turbulence. This scaling is typical of turbulent kinetic energy transfer in the inertial range. In figure 2.1 we show a typical energy spectrum of numerical simulations.

### Taylor based Reynolds number

Apart from the integral length, we can derive a second length scale from the autocorrelation functions. The autocorrelation functions  $f$  and  $g$  are parabolic at  $\mathbf{r} = 0$ . Taking a Taylor

expansion of  $f$  around  $\mathbf{r} = 0$  we obtain the so-called Taylor longitudinal microscale  $\lambda_f$  as

$$\lambda_f(t) = \left[ -\frac{1}{2} \frac{\partial^2 f(r, t)}{\partial r^2} \Big|_{r=0} \right]^{-1/2} \quad (2.17)$$

A similar length scale can be derived for the transverse autocorrelation function  $g$ , and it is related to the longitudinal Taylor microscale through  $\lambda_g(t) = \lambda_f(t)/\sqrt{2}$ . Furthermore, taking a Taylor expansion of  $f$  we can relate the longitudinal Taylor microscale to average of the gradient tensor as

$$\left\langle \left( \frac{\partial u_x}{\partial x} \right)^2 \right\rangle = \frac{2 u_{\text{rms}}^2}{3 \lambda_f^2}. \quad (2.18)$$

Using equation (2.12) we can also express the energy dissipation rate in terms of the Taylor microscale

$$\varepsilon = \frac{10\nu u_{\text{rms}}^2}{\lambda_f^2} \quad (2.19)$$

The Taylor microscale does not have a direct physical interpretation, and it is intermediate between the dissipative scales  $\eta$  and the integral length  $L$  [41]. The Taylor microscale is, however, a well defined quantity from which a Reynolds number can be defined. The so-called Taylor based Reynolds number is defined as

$$\text{R}_\lambda \equiv \frac{u_{\text{rms}} \lambda_f}{\sqrt{6} \nu} \quad (2.20)$$

The Taylor based Reynolds number is commonly used in turbulence simulations to characterize the degree of turbulence intensity. In figure 2.1 we present the energy spectrum of two numerical simulations. The integral range shows the  $k^{-5/3}$  scaling. Increasing the Reynolds number increases the range of the integral range. This means that the separation between the large scales and the scales at which viscosity dominates becomes larger.

## 2.2 Particles in turbulence

The Navier-Stokes equations (2.3)-(2.4) describe the velocity field of an incompressible fluid flow and appear in a wide variety of physical settings. The presence of particles in turbulent flows has been intensively studied [49], as it has applications ranging from industry applications to droplet growth in clouds.

We now turn our attention to non-inertial particles embedded within this turbulent fluid. We start by introducing the advection equation of Lagrangian tracers. That is, particles which have negligible inertia and are advected by the surrounding fluid. We will then introduce generalizations of these equations for particles with different features. Subsequently we will introduce the Jeffery's equations, which describe the rotations of a microscopic ellipsoid in a fluid flow due to the small-scale features of the flow.

### 2.2.1 Non-inertial particles

The most simple non-trivial particles one can encounter in turbulent flow are Lagrangian tracers. These are particles move with the velocity field, such that their position evolves as

$$\dot{\mathbf{x}} = \mathbf{u}(\mathbf{x}(t), t) \quad (2.21)$$

This is the simplest type of particles in a turbulent flow, and no feedback into the flow is considered. In this dissertation we will look at particles which are advected, but have additional contributions to their spatial evolution, for example due to motility or sedimentation. We will hence expand (2.21) to equations of the form

$$\dot{\mathbf{x}} = \mathbf{u} + \mathbf{f}(\hat{\mathbf{p}}), \quad (2.22)$$

where  $\hat{\mathbf{p}}$  is an orientation vector. In chapter 5 we will look at sedimenting ellipsoids (5.10). There we will explore a shape- and orientation-dependent particle settling. Later in chapter 4 we will investigate the effects of motile ellipsoids (4.3) in turbulence.

### 2.2.2 Particle orientation: Jeffery's equations

A key parameter of particles contained in a turbulent flow is their shape. Consider a particle with a certain geometry in a turbulent flow. The torques produced by the flow on the surface of the particle induce rotation. How these rotation rates depend on the exact shape of a particle is a complicated question, which usually escapes an easy solution. In the following we will present the equations for the rotation rate of small triaxial ellipsoids in turbulence, for which analytic results are known. We will then simplify this result to the case of an symmetric ellipsoid.

Consider the limiting case of small particles, smaller or comparable to the Kolmogorov length  $\eta$  of the flow. The local velocity field can then be expressed by a Taylor expansion in terms of gradients of the velocity field, i.e. strain  $\mathbf{S}$  and vorticity  $\boldsymbol{\omega}$ . The strain and vorticity the effect torque on the surface of the particle and induce rotation. Calculating the total torque is usually a complex computation, without a closed solution. In the case of ellipsoids, however, this computation can be carried out to obtain the rotation rates of the ellipsoid's main axes. This is known as Jeffery's equations [16], and the original derivation goes back to 1922. In the following we will present the Jeffery's equations for a triaxial ellipsoid [50] and then simplify to the case of symmetric ellipsoids.

We begin by considering a triaxial ellipsoid with three main axes given by  $a_i$ , where  $i = 1, 2, 3$ . We define, additionally, the auxiliary shape parameters  $\alpha_i$ , defined as

$$\alpha_1 = \frac{(a_2/a_3)^2 - 1}{(a_2/a_3)^2 + 1}, \quad \alpha_2 = \frac{(a_3/a_1)^2 - 1}{(a_3/a_1)^2 + 1}, \quad \alpha_3 = \frac{(a_1/a_2)^2 - 1}{(a_1/a_2)^2 + 1}. \quad (2.23)$$

Now let us define the orientation of the ellipsoid by the orientation of the ellipsoid axes. We define the unitary vectors  $\hat{\mathbf{p}}_i$  pointing in the corresponding  $a_i$  axis, such that they form a complete right-handed orthonormal vectorial basis, i.e.

$$\mathbb{1}_{3 \times 3} = \hat{\mathbf{p}}_1 \otimes \hat{\mathbf{p}}_1^T + \hat{\mathbf{p}}_2 \otimes \hat{\mathbf{p}}_2^T + \hat{\mathbf{p}}_3 \otimes \hat{\mathbf{p}}_3^T, \quad \hat{\mathbf{p}}_i^T \cdot \hat{\mathbf{p}}_j = \delta_{ij}, \quad \epsilon_{ijk} \hat{\mathbf{p}}_j \hat{\mathbf{p}}_k = \hat{\mathbf{p}}_i. \quad (2.24)$$

By taking the limit of small ellipsoids, such that a strain  $\mathbf{S}$  and vorticity  $\boldsymbol{\omega} = \nabla \times \mathbf{u}$  dominate the torques on the ellipsoid, Jeffery worked out the rate of change of the orientation of these orientation vectors. The time evolution of the orientation vectors  $\hat{\mathbf{p}}_i$  can be cast as [50]

$$\dot{\hat{\mathbf{p}}}_1 = \frac{1}{2} \boldsymbol{\omega} \times \hat{\mathbf{p}}_1 - \alpha_2 \hat{\mathbf{p}}_3 (\hat{\mathbf{p}}_3^T \mathbf{S} \hat{\mathbf{p}}_1) + \alpha_3 \hat{\mathbf{p}}_2 (\hat{\mathbf{p}}_2^T \mathbf{S} \hat{\mathbf{p}}_1), \quad (2.25)$$

$$\dot{\hat{\mathbf{p}}}_2 = \frac{1}{2} \boldsymbol{\omega} \times \hat{\mathbf{p}}_2 - \alpha_3 \hat{\mathbf{p}}_1 (\hat{\mathbf{p}}_1^T \mathbf{S} \hat{\mathbf{p}}_2) + \alpha_1 \hat{\mathbf{p}}_3 (\hat{\mathbf{p}}_3^T \mathbf{S} \hat{\mathbf{p}}_2), \quad (2.26)$$

$$\dot{\hat{\mathbf{p}}}_3 = \frac{1}{2} \boldsymbol{\omega} \times \hat{\mathbf{p}}_3 - \alpha_1 \hat{\mathbf{p}}_2 (\hat{\mathbf{p}}_2^T \mathbf{S} \hat{\mathbf{p}}_3) + \alpha_2 \hat{\mathbf{p}}_1 (\hat{\mathbf{p}}_1^T \mathbf{S} \hat{\mathbf{p}}_3). \quad (2.27)$$

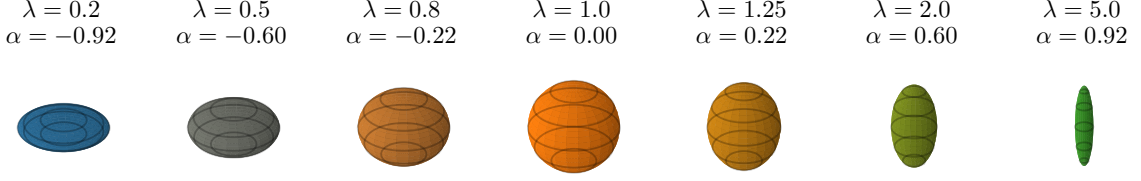


Figure 2.2: Ellipsoid shape can be parametrized by the aspect ratio  $\lambda$  between the axis of symmetry, and the other axes. The shape parameter  $\alpha$  (2.28) is a function of the aspect ratio and is the relevant shape control parameter in Jeffery's equations (2.39); it determines the rotational dynamics of an ellipsoid in a fluid flow.

We can readily verify that these vectors remain unitary with time evolution, that is  $d\hat{\boldsymbol{p}}_i^2/dt = \hat{\boldsymbol{p}}_i^T \cdot \dot{\hat{\boldsymbol{p}}}_i = 0$ . It is notable that these equations are cyclic, revealing the interchangeability of the labels of the different axes.

Consider now the case of an ellipsoid with two equal axes, and a third axis of symmetry. Let us define the axis of symmetry as  $i = 1$ . Consider now the ratio between the axis of symmetry and the other axes as  $\lambda$ , i.e.  $\lambda = a_1/a_2 = a_1/a_3$ . Then the auxiliary shape parameters (2.23) become

$$\alpha_1 = 0, \quad -\alpha_2 = \alpha_3 = \frac{\lambda^2 - 1}{\lambda^2 + 1} =: \alpha. \quad (2.28)$$

and we are left with only one shape parameter  $\alpha$ . The relation between  $\alpha$  and  $\lambda$  is shown in figure 2.2. The equations (2.25)-(2.27) then take the form

$$\dot{\hat{\boldsymbol{p}}}_1 = \frac{1}{2}\boldsymbol{\omega} \times \hat{\boldsymbol{p}}_1 + \alpha \left[ \hat{\boldsymbol{p}}_2 \otimes \hat{\boldsymbol{p}}_2^T + \hat{\boldsymbol{p}}_3 \otimes \hat{\boldsymbol{p}}_3^T \right] S \hat{\boldsymbol{p}}_1, \quad (2.29)$$

$$\dot{\hat{\boldsymbol{p}}}_2 = \frac{1}{2}\boldsymbol{\omega} \times \hat{\boldsymbol{p}}_2 - \alpha \hat{\boldsymbol{p}}_1 (\hat{\boldsymbol{p}}_1^T S \hat{\boldsymbol{p}}_2), \quad (2.30)$$

$$\dot{\hat{\boldsymbol{p}}}_3 = \frac{1}{2}\boldsymbol{\omega} \times \hat{\boldsymbol{p}}_3 - \alpha \hat{\boldsymbol{p}}_1 (\hat{\boldsymbol{p}}_1^T S \hat{\boldsymbol{p}}_3). \quad (2.31)$$

Using the identities (2.24) we can reduce the dynamics of the ellipsoid orientation to depend only on  $\hat{\boldsymbol{p}}_1$ ,  $\hat{\boldsymbol{p}}_2$ ,  $\hat{\boldsymbol{p}}_3$ , and  $\dot{\hat{\boldsymbol{p}}}_1$ . Using the identity

$$\hat{\boldsymbol{p}}_2 \otimes \hat{\boldsymbol{p}}_2^T + \hat{\boldsymbol{p}}_3 \otimes \hat{\boldsymbol{p}}_3^T = \mathbb{1}_{3 \times 3} - \hat{\boldsymbol{p}}_1 \otimes \hat{\boldsymbol{p}}_1^T \quad (2.32)$$

we can rewrite equation (2.29) so that  $\dot{\hat{\boldsymbol{p}}}_1$  only depends on  $\hat{\boldsymbol{p}}_1$ ,  $S$ , and  $\boldsymbol{\omega}$ . Now, applying a time derivative on the identity  $\hat{\boldsymbol{p}}_2 = \hat{\boldsymbol{p}}_3 \times \hat{\boldsymbol{p}}_1$  we obtain

$$\dot{\hat{\boldsymbol{p}}}_2 = \dot{\hat{\boldsymbol{p}}}_3 \times \hat{\boldsymbol{p}}_1 + \hat{\boldsymbol{p}}_3 \times \dot{\hat{\boldsymbol{p}}}_1. \quad (2.33)$$

The first term in this equation can be substituted from equation (2.31) to yield

$$\dot{\hat{\boldsymbol{p}}}_3 \times \hat{\boldsymbol{p}}_1 = \frac{1}{2}(\boldsymbol{\omega} \times \hat{\boldsymbol{p}}_3) \times \hat{\boldsymbol{p}}_1 = \frac{\hat{\boldsymbol{p}}_1^T \cdot \boldsymbol{\omega}}{2} \hat{\boldsymbol{p}}_3. \quad (2.34)$$

For the second term in equation (2.33) we can use  $\hat{\boldsymbol{p}}_3 = \hat{\boldsymbol{p}}_1 \times \hat{\boldsymbol{p}}_2$  to obtain

$$\hat{\boldsymbol{p}}_3 \times \dot{\hat{\boldsymbol{p}}}_1 = (\hat{\boldsymbol{p}}_1 \times \hat{\boldsymbol{p}}_2) \times \dot{\hat{\boldsymbol{p}}}_1 = -\hat{\boldsymbol{p}}_1 (\hat{\boldsymbol{p}}_2^T \cdot \dot{\hat{\boldsymbol{p}}}_1). \quad (2.35)$$

Proceeding then in a similar manner with  $\hat{\boldsymbol{p}}_3$  we can rewrite equations (2.29)-(2.31) as

$$\dot{\hat{\boldsymbol{p}}}_1 = \frac{1}{2}\boldsymbol{\omega} \times \hat{\boldsymbol{p}}_1 + \alpha \left( S\hat{\boldsymbol{p}}_1 - \hat{\boldsymbol{p}}_1^T S\hat{\boldsymbol{p}}_1 \hat{\boldsymbol{p}}_1 \right), \quad (2.36)$$

$$\dot{\hat{\boldsymbol{p}}}_2 = \frac{\hat{\boldsymbol{p}}_1^T \cdot \boldsymbol{\omega}}{2} \hat{\boldsymbol{p}}_3 - \hat{\boldsymbol{p}}_1 (\hat{\boldsymbol{p}}_2^T \cdot \dot{\hat{\boldsymbol{p}}}_1), \quad (2.37)$$

$$\dot{\hat{\boldsymbol{p}}}_3 = -\frac{\hat{\boldsymbol{p}}_1^T \cdot \boldsymbol{\omega}}{2} \hat{\boldsymbol{p}}_2 - \hat{\boldsymbol{p}}_1 (\hat{\boldsymbol{p}}_3^T \cdot \dot{\hat{\boldsymbol{p}}}_1). \quad (2.38)$$

Note that with this formulation it becomes clear that the orientation of the ellipsoid is then defined by the orientation of the axis of symmetry. The other axes,  $\hat{\boldsymbol{p}}_2$  and  $\hat{\boldsymbol{p}}_3$ , are slave variables to  $\hat{\boldsymbol{p}}_1$ . We hence will only keep track of the dynamics of the axis of symmetry  $\hat{\boldsymbol{p}}_1$ , which we denote  $\hat{\boldsymbol{p}}$  from now on. We drop the dynamics of  $\hat{\boldsymbol{p}}_2$  and  $\hat{\boldsymbol{p}}_3$  and retain the rotational evolution of the ellipsoid as

$$\dot{\hat{\boldsymbol{p}}} = \frac{1}{2}\boldsymbol{\omega} \times \hat{\boldsymbol{p}} + \alpha \left( S\hat{\boldsymbol{p}} - \hat{\boldsymbol{p}}^T S\hat{\boldsymbol{p}} \hat{\boldsymbol{p}} \right). \quad (2.39)$$

It is these set of equations which are commonly called the Jeffery's equations. Note that in this reduced formulation the orientation vector  $\hat{\boldsymbol{p}}$  remains normalized. Here this is due to the  $\hat{\boldsymbol{p}}S\hat{\boldsymbol{p}}$  term. This term is a Lagrangian multiplier, ensuring the normalization of  $\hat{\boldsymbol{p}}$  in the  $\alpha \neq 0$  case. This equation has been intensively used to study rotation of particles in turbulent flows [51].

## 2.3 Particle collisions

In real turbulent flows, particles contained in the flow are advected and may also be affected by sedimentation, and the particles might be motile. These particles can collide or coalesce. Measuring collision rates is a way to statistically approach these collision events. Just as we did with the equations of motion when we neglected feedback into the surrounding fluid, here we will do a simplifying consideration. We will use the so-called ghost collision approximation. Using this approximation, particles may overlap and move through one another. Collisions are merely the event at which a particle overlaps another one. But no change is made to the equations of motion of the particle itself, of the colliding particle, or the underlying flow.

In this section we will explain the concept of a collision kernel as a statistical measure for particle collision occurrences. Additionally we will describe geometrical conditions by which to measure and classify collisions between spheres, thin disks, and rods.

### 2.3.1 Collision kernel

In a physical flow particles can collide, coalesce, or even interact. To quantify the evolution of droplet size distributions a Boltzmann like equation comes into play [52]. Within this complex picture a critical quantity is the so-called collision kernel  $\Gamma$  [53]. In the droplet case, the collision kernel describes the rate at which particles of different radius collide. In general, however, the collision kernel is a geometric quantity obtained by also taking into account particle shape and orientation. It describes the collision rate of particles averaging over all possible geometrical collision configuration. In the context of microorganism, the collision kernel  $\Gamma$  is also called sometimes encounter rate [14].

Consider a total of  $N$  identical particles in a volume  $V$ . Now consider that in a certain time

$T$  the total number of new collisions is  $N_c$ . Then the collision kernel  $\Gamma$  is the proportionality constant between particle number, volume, and time, and the total number of new collisions [54, 55]

$$N_c = \frac{\Gamma N^2 T}{2V} \quad \text{or equivalently} \quad \Gamma = \frac{2V N_c}{N^2 T}. \quad (2.40)$$

The collision kernel  $\Gamma$  is a statistical quantity which states how many new collision of a given particle species will occur, given volume, time, and number of particles.

In a simulation a new collision is then characterized as a particle pair transitioning from no collision to collision over a timestep. Numerically the total number of new collisions  $N_c$  over a time period  $T$  is obtained by keeping track of the identity of colliding particles and integrating, i.e.

$$N_c = \int_0^T \frac{dN_c}{dt} dt. \quad (2.41)$$

### Saffman-Turner kernel

A celebrated result in the theory of turbulence is the so-called Saffman-Turner kernel [56]. This is a collision kernel for small non-inertial spheres of radius  $r$  advected by turbulence. The kernel has the form

$$\Gamma^{\text{ST}} = 1.3 (2r)^3 \sqrt{\frac{\varepsilon}{\nu}}. \quad (2.42)$$

The Saffman-Turner collision kernel is proportional to sphere volume. This intuitively means that larger spheres collide more often than smaller ones. Additionally, using we identify that the kernel is inversely proportional to the Kolmogorov time  $\tau_\eta$  (2.13). This means that in more intense turbulence, i.e. smaller  $\tau_\eta$ , collisions happen more often than in milder turbulence with a larger  $\tau_\eta$ . It is notable that the Saffman-Turner result overestimates the real measured collision rates from simulations by around 5% [57].

## 2.4 Ghost collision algorithms

In our approach we have neglected the hydrodynamic interactions between particles, as well as any feedback effect of the particles on the fluid flow. For calculating collisions we also use a simplified approach, the so-called ghost collision approximation [54, 57, 58]. This consists of simulating particles in a flow which can geometrically overlap without interacting with one another. Hence, by use of simulations we can measure how often particles come close enough to one another to touch or even overlap, but we ignore any coagulation or interaction effects resulting from this process. Deriving and implementing exact algorithms for particle collision detection is notably difficult, even in the case of ellipsoids [59, 60]. Therefore, in the following, we will describe the collision test for three limiting cases of particle shapes: spheres, thin disks, and slim rods.

### 2.4.1 Collision algorithm between spheres

Collision between spheres happen, when the distance between the centers of two spheres  $\mathbf{r}_i$  is smaller than their diameter  $d$ , that is:

$$\sqrt{(\mathbf{r}_1 - \mathbf{r}_2)^2} \leq d. \quad (2.43)$$

### 2.4.2 Collision algorithm between thin disks

Consider two disks centered at  $\mathbf{x}_1$  and  $\mathbf{x}_2$ , and orientations  $\hat{\mathbf{p}}_1$  and  $\hat{\mathbf{p}}_2$ . Their width is denoted as  $w$ . A collision, if any, will happen along the intersection of the two planes which contain these disks. The intersection of these planes is a line. Positions along this line can be parametrized by one parameter  $t$ , the line orientation  $\hat{\mathbf{p}}_0$ , and a point along this line  $\mathbf{x}_0$  as

$$\mathbf{l}(t) = \mathbf{x}_0 + \hat{\mathbf{p}}_0 t, \quad (2.44)$$

where the vectors  $\mathbf{x}_0$  and  $\hat{\mathbf{p}}_0$  can be defined as

$$\hat{\mathbf{p}}_0 = \hat{\mathbf{p}}_1 \times \hat{\mathbf{p}}_2, \quad \mathbf{x}_0 = (\mathbf{x}_1 \cdot \hat{\mathbf{p}}_1) \hat{\mathbf{p}}_1 + \frac{(\mathbf{x}_1 \cdot \hat{\mathbf{p}}_1)(\hat{\mathbf{p}}_1 \cdot \hat{\mathbf{p}}_2) - \mathbf{x}_2 \cdot \hat{\mathbf{p}}_2}{1 - (\hat{\mathbf{p}}_1 \cdot \hat{\mathbf{p}}_2)^2} [\hat{\mathbf{p}}_2 - (\hat{\mathbf{p}}_1 \cdot \hat{\mathbf{p}}_2) \hat{\mathbf{p}}_1]. \quad (2.45)$$

The distance between the disk center and an arbitrary point along this line is given by

$$d_i(t) = \sqrt{[\mathbf{x}_i - \mathbf{l}(t)]^2} \quad (2.46)$$

If a collision were to happen, it would require that  $d_i(t) \leq w/2$ . We then solve this equation for the solutions to  $d_i(t_{i\pm}) = w/2$ . This can be solved analytically to

$$t_{i\pm} = \mathbf{x}_i \cdot \hat{\mathbf{p}}_0 \pm \sqrt{(\mathbf{x}_i \cdot \hat{\mathbf{p}}_0)^2 + w^2/4 - (\mathbf{x}_i - \mathbf{x}_0)^2}. \quad (2.47)$$

If for one of the disks no solution pair exists, then a collision is impossible. On the other hand, if solutions exist, then a collision will happen when the two disk sections overlap. This overlap can be tested as

$$t_{1+} \geq t_{2-} \wedge t_{2+} \geq t_{1-}. \quad (2.48)$$

If this computation is true, then a collision happens.

### 2.4.3 Collision algorithm between rods with spherical caps

Collisions between thin rods can be calculated by searching for the minimal distance between the two symmetry axis of the rods with spherical caps. In the limit of very thin rods the spherical caps are negligible, and this algorithm practically becomes the same as checking for collisions of pure rod geometry. Consider that the first rod at a position  $\mathbf{x}$  with orientation  $\hat{\mathbf{p}}$ , and a second rod with orientation  $\hat{\mathbf{q}}$  at a position  $\mathbf{y}$ . Both rods have length  $l$ , with two spherical caps of radius  $l/2\lambda$ , a cylindrical body of length  $l(1 - 1/\lambda)$ , and width  $w = l/\lambda$ . Positions along the rods may be parametrized by use of the parameters  $t, s \in [-1, 1]$ , such that any point along the symmetry axis of the rods may be written as

$$\mathbf{r}_1(t) = \mathbf{x} + \frac{t l}{2} \hat{\mathbf{p}} \left(1 - \frac{1}{\lambda}\right); \quad t \in [-1, 1] \quad (2.49)$$

for the first rod, and

$$\mathbf{r}_2(s) = \mathbf{y} + \frac{s l}{2} \hat{\mathbf{q}} \left(1 - \frac{1}{\lambda}\right); \quad s \in [-1, 1] \quad (2.50)$$

for the second. The distance between two points on symmetry axis of the rods is then

$$\text{dist}(t, s) = \sqrt{[\mathbf{r}_1(t) - \mathbf{r}_2(s)]^2} = \sqrt{\left[\frac{l}{2} \left(1 - \frac{1}{\lambda}\right) (\hat{\mathbf{p}} t - \hat{\mathbf{q}} s) + \Delta \mathbf{x}\right]^2}. \quad (2.51)$$

Here we define  $\Delta \mathbf{x} = \mathbf{x} - \mathbf{y}$ . The minimum distance can be found by setting the gradient of this distance function to zero. This leads to a linear system, which can be solved to

$$\begin{pmatrix} t_{\min} \\ s_{\min} \end{pmatrix} = \frac{2}{l(\lambda - 1)} \frac{\lambda}{(\hat{\mathbf{p}} \cdot \hat{\mathbf{q}})^2 - 1} \begin{pmatrix} 1 & -\hat{\mathbf{p}} \cdot \hat{\mathbf{q}} \\ \hat{\mathbf{p}} \cdot \hat{\mathbf{q}} & -1 \end{pmatrix} \begin{pmatrix} \Delta \mathbf{x} \cdot \hat{\mathbf{p}} \\ \Delta \mathbf{x} \cdot \hat{\mathbf{q}} \end{pmatrix}. \quad (2.52)$$

This yields the minimum distance if  $|t_{\min}, s_{\min}| \leq 1$ , that is, if we are inside both rods. If  $|t_{\min}| \geq 1$  or  $|s_{\min}| \geq 1$  we must search for the minimum distance along  $|t| = 1$  and  $|s| = 1$ . Along the edges the minimum distance can be analytically calculated by finding the minimum of equation (2.51) for  $t$  ( $s$ ), while keeping  $s$  ( $t$ ) constant. Keeping  $t$  constant at  $t_{\min} = \pm 1$  the minimum at  $s$  is found at

$$s_{\min} = t_{\min} \hat{\mathbf{p}} \cdot \hat{\mathbf{q}} + \frac{2}{l} \frac{\lambda}{\lambda - 1} \Delta \mathbf{x} \cdot \hat{\mathbf{q}}. \quad (2.53)$$

Keeping  $s$  constant at  $s_{\min} = \pm 1$  the minimum for  $t$  is found at

$$t_{\min} = s_{\min} \hat{\mathbf{p}} \cdot \hat{\mathbf{q}} - \frac{2}{l} \frac{\lambda}{\lambda - 1} \Delta \mathbf{x} \cdot \hat{\mathbf{p}}. \quad (2.54)$$

Collisions at a given time snapshot can then be characterized as  $\text{dist}(t_{\min}, s_{\min}) < \text{rod width}$ .

## 2.5 Details on numerical simulations

The Navier-Stokes equation (2.1)-(2.2) describe the time evolution of a velocity field  $\mathbf{u}$ . In this dissertation we will be interested on the specific case of isotropic homogeneous turbulence. To this end we will be simulating the Navier-Stokes equations directly in a cube with periodic boundary conditions. For this usecase a very advantageous technique for solving the Navier-Stokes equations is the so-called pseudo-spectral approach. In the following we will describe the numerical approach for solving the Navier-Stokes equations. Finally, we will then visit the implementation of Jeffery's equations in the code and give an overview of the particle implementation in the code.

### 2.5.1 Pseudo-spectral approach to solving the Navier-Stokes equations

The pseudo-spectral approach to solving the Navier-Stokes equation (2.1)-(2.2) actually solves the vorticity formulation in Fourier space. Recall that vorticity  $\boldsymbol{\omega}$  is the curl of the velocity field, i.e.  $\boldsymbol{\omega}(\mathbf{x}, t) = \nabla \times \mathbf{u}(\mathbf{x}, t)$ . Applying a curl to equation (2.1) we obtain a partial differential equation for vorticity

$$\frac{\partial \boldsymbol{\omega}}{\partial t} = \nabla \times (\mathbf{u} \times \boldsymbol{\omega}) + \nu \Delta \boldsymbol{\omega} + \nabla \times \mathbf{f}. \quad (2.55)$$

To obtain this equation we have used the incompressibility condition of velocity  $\nabla \cdot \mathbf{u} = 0$ , as well of the vorticity field  $\nabla \cdot \boldsymbol{\omega} = 0$ . Additionally, the identity  $\nabla \times (\mathbf{u} \times \boldsymbol{\omega}) = (\boldsymbol{\omega} \cdot \nabla) \mathbf{u} - (\mathbf{u} \cdot \nabla) \boldsymbol{\omega}$  is needed when deriving equation (2.55). The pressure term, previously a Lagrange multiplier ensuring incompressibility, is gone. But now, both velocity  $\mathbf{u}$  and vorticity  $\boldsymbol{\omega}$  appear in the same equation. The Biot-Savart law can be used to invert the velocity in terms of vorticity, i.e.

$$\mathbf{u}(\mathbf{x}, t) = \frac{1}{4\pi} \int d^3 \mathbf{y} \frac{\boldsymbol{\omega}(\mathbf{y}, t) \times (\mathbf{x} - \mathbf{y})}{|\mathbf{x} - \mathbf{y}|^3} \quad (2.56)$$

Together, equations (2.55) and (2.56) form a closed system of integro-differential equations for vorticity  $\boldsymbol{\omega}$ . As a next step we will transform into a Fourier representation. Because we are

working in a cube with periodic boundary conditions the Fourier representation automatically fulfills the periodic boundary conditions. Consider the Fourier transformation, denoted by  $\mathcal{F}$  and its inverse by  $\mathcal{F}^{-1}$ . We denote the Fourier wave vector as  $\mathbf{k}$ , and the Fourier representation of velocity and vorticity as  $\hat{\mathbf{u}}$  and  $\hat{\boldsymbol{\omega}}$ , respectively. Therefore we have

$$\hat{\mathbf{u}}(\mathbf{k}, t) = \mathcal{F}[\mathbf{u}(\mathbf{x}, t)], \quad \hat{\boldsymbol{\omega}}(\mathbf{k}, t) = \mathcal{F}[\boldsymbol{\omega}(\mathbf{x}, t)]. \quad (2.57)$$

Applying the Fourier transform to equation (2.55) we obtain

$$\frac{\partial \hat{\boldsymbol{\omega}}}{\partial t} = \mathbf{i}\mathbf{k} \times \mathcal{F}[\mathbf{u} \times \boldsymbol{\omega}] - \nu \mathbf{k}^2 \hat{\boldsymbol{\omega}} + \hat{\mathbf{F}} \quad (2.58)$$

Where  $\hat{\mathbf{F}}$  the forcing in Fourier space  $\hat{\mathbf{F}} = \mathcal{F}[\nabla \times \mathbf{f}]$ . The Biot-Savart law (2.56) in Fourier space now takes a simpler form than in real space

$$\hat{\mathbf{u}} = \frac{\mathbf{i}\mathbf{k} \times \hat{\boldsymbol{\omega}}}{\mathbf{k}^2}. \quad (2.59)$$

Replacing real space velocity and vorticity in equation (2.58) and using the Fourier Biot-Savart formulation of the velocity field (2.59) we obtain

$$\frac{\partial \hat{\boldsymbol{\omega}}}{\partial t} = \mathbf{i}\mathbf{k} \times \mathcal{F}\left[\mathcal{F}^{-1}\left[\frac{\mathbf{i}\mathbf{k} \times \hat{\boldsymbol{\omega}}}{\mathbf{k}^2}\right] \times \mathcal{F}^{-1}[\hat{\boldsymbol{\omega}}]\right] - \nu \mathbf{k}^2 \hat{\boldsymbol{\omega}} + \hat{\mathbf{F}} \quad (2.60)$$

Compared to the real space velocity formulation (2.3), the Fourier equation for the vorticity (2.60) is a closed system of partial differential equations for vorticity  $\boldsymbol{\omega}$ : instead of having a pressure term, which is non-local and difficult to compute, in Fourier space becomes a multiplication. This is the reason why this method to solve the Navier-Stokes equations is called pseudo-spectral. We solve the time evolution equations in Fourier space, but use the Fourier transform to compute the computationally intensive non-linear term in equation (2.60). In our code we solve this equation, and then obtain the velocity field by means of Biot-Savart law and inverse Fourier transform. We use our in-house code TurTLE [61] to integrate the vorticity formulation (2.60). We use a third order Runge-Kutta method for time integration and use the FFTW library [62] to perform the Fourier transform. A mixed parallelization scheme using MPI and OpenMP allows for a scalable and efficient implementation.

### 2.5.2 Particle integration

The code TurTLE [61] implements particle position and orientation via time integration of the equations of motion. This is done with a second order Adams-Bashforth time integrating scheme. The particles are distributed according to the parallelization scheme described in the previous section, allowing also for numerical scalability and efficiency solving for the particles in the turbulent flow. The particles can be coupled to the value of the velocity, vorticity, or gradient fields at each particle position. This is done via an efficient and scalable interpolation scheme [61]. The coupling is one way, as the particles can be coupled to the fluid flow, but they themselves have no effect on the underlying flow. Additionally, the code allows for particle interaction. This can be implemented in a variety of ways. In this thesis we utilize the interaction functionality to carry out the measurement of particle collisions.

As part of the work carried out during this doctoral thesis, we used the existing particle code to implement the Jeffery's equations (2.39). As we discussed in section 2.2.2, the term  $\hat{\mathbf{p}}^T \mathbf{S} \hat{\mathbf{p}}$

is a Lagrange multiplier to ensure that  $\hat{\mathbf{p}}$  remains a unitary vector. Numerically, however, this term leads to numerical instabilities. Hence we integrate the equations without this term and then normalize the orientation vector after each time step. Starting from equation (2.39) and using (2.11) we exclude the Lagrange multiplier and expand the  $x$ -component of the orientation vector  $\hat{\mathbf{p}}$  as

$$\dot{p}_x = \frac{1}{2} [\omega_y p_z - \omega_z p_y] + \alpha \left[ \frac{\partial u_x}{\partial x} p_x + \left( \frac{\partial u_y}{\partial x} + \frac{\partial u_x}{\partial y} \right) \frac{p_y}{2} + \left( \frac{\partial u_z}{\partial x} + \frac{\partial u_x}{\partial z} \right) \frac{p_z}{2} \right]. \quad (2.61)$$

Furthermore, using the definition of the shape parameter  $\alpha$  (2.28) in terms of the aspect ratio  $\lambda$  and replacing the components of vorticity with  $\omega_i = \epsilon_{ijk} \partial_j u_k$  we can further expand the expression of  $\dot{p}_x$  as

$$\begin{aligned} \dot{p}_x = & \frac{1}{2} \left[ \left( \frac{\partial u_x}{\partial z} - \frac{\partial u_z}{\partial x} \right) p_z - \left( \frac{\partial u_y}{\partial x} - \frac{\partial u_x}{\partial y} \right) p_y \right] \\ & + \frac{\lambda^2 - 1}{\lambda^2 + 1} \left[ \frac{\partial u_x}{\partial x} p_x + \left( \frac{\partial u_y}{\partial x} + \frac{\partial u_x}{\partial y} \right) \frac{p_y}{2} + \left( \frac{\partial u_z}{\partial x} + \frac{\partial u_x}{\partial z} \right) \frac{p_z}{2} \right]. \end{aligned} \quad (2.62)$$

Rearranging this expression we finally obtain

$$\dot{p}_x = \frac{1}{\lambda^2 + 1} \left[ p_z \left( \lambda^2 \frac{\partial u_x}{\partial z} - \frac{\partial u_z}{\partial x} \right) + p_y \left( \lambda^2 \frac{\partial u_x}{\partial y} - \frac{\partial u_y}{\partial x} \right) + p_x \left( \lambda^2 - 1 \right) \frac{\partial u_x}{\partial x} \right]. \quad (2.63)$$

It is this expression in terms of  $\lambda$ , the components of the orientation vector  $p_i$ , and the components of the velocity gradient tensor  $\partial u_i / \partial x_j$  that we implemented in our code. The other components of  $\hat{\mathbf{p}}$  are obtained by cyclic permutation. The orientation vectors are then normalized at each time step.



---

Part I

—  
Manuscript I

---

# Microswimmers in an axisymmetric vortex flow

This chapter consists of a manuscript which originally appeared as "[Arguedas-Leiva, J.-A and Wilczek, M. \(2020\). Microswimmers in an axisymmetric vortex flow. \*New Journal of Physics\*, 22 \(053051\)](#)" and is licensed under the [Creative Commons Attribution 4.0 licence \(CC BY 4.0\)](#).

M. W. designed the research. J.-A. A.-L. carried out the analytic computations, numerical simulations, and figure generation. Both authors wrote the manuscript.

# Microswimmers in an axisymmetric vortex flow

José-Agustín Arguedas-Leiva<sup>1,2</sup> and Michael Wilczek<sup>1,2</sup>

<sup>1</sup>Max Planck Institute for Dynamics and Self-Organization (MPI DS),  
Am Faßberg 17, 37077 Göttingen, Germany

<sup>2</sup>Faculty of Physics, University of Göttingen,  
Friedrich-Hund-Platz 1, 37077 Göttingen, Germany

<sup>†</sup>To whom correspondence should be addressed; E-mail: michael.wilczek@ds.mpg.de .

## Abstract

Microswimmers are encountered in a wide variety of biophysical settings. When interacting with flow fields, they show interesting dynamical features such as hydrodynamical trapping, clustering, and preferential orientation. One important step towards the understanding of such features is to clarify the interplay of hydrodynamic flows with microswimmer motility and shape. Here, we study the dynamics of ellipsoidal microswimmers in a two-dimensional axisymmetric vortex flow. Despite this simple setting, we find surprisingly rich dynamics, which can be comprehensively characterized in the framework of dynamical systems theory. By classifying the fixed-point structure of the underlying phase space as a function of motility and microswimmer shape, we uncover the topology of the phase space and determine the conditions under which microswimmers are trapped in the vortex. For spherical microswimmers, we identify Hamiltonian dynamics, which are broken for microswimmers of a different shape. We find that prolate ellipsoidal microswimmers tend to align parallel to the velocity field, while oblate microswimmers tend to remain perpendicular to it. Additionally, we find that rotational noise allows microswimmers to escape the vortex with an enhanced escape rate close to the system's saddle point. Our results clarify the role of shape and motility on the occurrence of preferential concentration and clustering and provide a starting point to understand the dynamics in more complex flows.

Driven by the need to better understand the physical mechanisms of microswimming, e.g. in the context of phytoplankton in the ocean [63] or artificial microswimmers in the laboratory [64], the investigation of microswimmers in complex flows has gained considerable momentum over the past years. In such flows, inertial effects [18, 65–68], gyrotactic swimming [15, 19, 24, 32–40], fluid-cell [6, 69] and cell-cell interaction [17, 70], as well as active motility and morphological changes [22, 71] can give rise to complex spatial microswimmer distributions and enable migration strategies.

Among the various mechanisms, shape and motility are the key parameters in quantifying microswimmer interaction with hydrodynamic flows [20, 23, 26, 72]. For instance, motility is a crucial ingredient for the emergence of clustering of neutrally buoyant particles [23, 24, 37]. Shape, on the other hand, determines the dynamic reaction to hydrodynamic cues. Rod-like agents, for example, tend to align with the direction of local vorticity, while also spinning due

to it [73–77]. Furthermore, it has recently been shown that self-propelled rod-shaped particles tend to align with the velocity field [72].

Given the complexity of turbulent and spatiotemporally varying flows, several investigations have focused on simple flows, which allow making contact with dynamical systems theory. For example, the (quasi-)periodic [78] and chaotic [79] motion of spherical microswimmers in a Poiseuille flow can be understood through the underlying Hamiltonian dynamics. In this scenario, the effect of shape in microswimmer dynamics and its relation to the swimming velocity could be well understood: Elongated microswimmers explicitly break the symplectic structure of the dynamics, but their swimming behavior qualitatively follows the swinging and tumbling motion observed for spherical microswimmers [80]. As another example, the ubiquity of vortices in natural environments and their dynamical impact on biological agents [81] continues to make the study of single vortex structures a good starting point for understanding microswimming in more complex, biologically relevant flows [82]. Isolating the impact of individual vortices on microswimming in a two-dimensional cellular flow has revealed barriers to particle transport as a function of shape and swimming speed [83, 84]. Shape deformation, as another example, has been found to have a strong impact on the scattering dynamics of individual microswimmers in a single vortex structure [85]. This illustrates how the investigation of simple flow settings sheds light on the interplay between shape and swimming speed on microswimmer dynamics.

Here, we comprehensively characterize microswimmer dynamics in a single vortex structure by relating the observed physical phenomena to properties of the underlying dynamical system. In particular, we consider non-interacting microswimmers in a two-dimensional axisymmetric vortex flow and address their trapping properties as well as the occurrence of clustering (the spatially heterogeneous distribution of particles) and preferential orientation with respect to the velocity field. We idealize microswimmers as advected ellipsoidal particles, which additionally have a swimming direction and a constant self-propulsion speed. Furthermore, vorticity and shear induce particle tumbling, which alters the swimming direction.

Our study discusses the fundamental dynamical systems properties of ellipsoidal microswimmers in a general axisymmetric vortex flow, complementing previous works on simple vortex [81] and cellular flows [83].

This simple setting reveals surprising insights: we identify an effective swimming velocity, which takes into account both motility and shape, as a control parameter for this system. We find surprisingly rich dynamics, which can be comprehensively characterized in the framework of dynamical systems theory. Classifying the fixed-point structure of the underlying phase space as a function of the effective swimming velocity allows distinguishing microswimmers that escape the vortex from the ones which remain trapped. Moreover, we find that spherical microswimmers obey Hamiltonian dynamics, whereas other shapes break the symplectic structure of phase space. Hence phase-space contraction, and ultimately preferential concentration, can be set into the context of breaking of Hamiltonian dynamics by departure from a spherical shape. Finally, to quantify the robustness of our results, we investigate the impact of rotational noise. We find that a saddle point, present in the relevant phase space, plays an important role in the escape of microswimmers from the vortex core.

### 3.1 Microswimmers in a vortex flow

#### 3.1.1 Model equations

We model microswimmers as inertialess particles advected by a velocity field  $\mathbf{u}$ . The particles are additionally capable of self-propulsion with swimming velocity  $v_s$  in direction  $\hat{\mathbf{p}}$  [15]. The microswimmer position  $\mathbf{x}$  obeys the equation of motion

$$\dot{\mathbf{x}} = \mathbf{u} + v_s \hat{\mathbf{p}}, \quad (3.1)$$

where the flow field is evaluated at the Lagrangian position of the microswimmer  $\mathbf{u}(t, \mathbf{x}(t))$ . A simple but effective way to introduce shape is to consider ellipsoidal microswimmers [86]. Particle orientation can be described by the particle's symmetry axis  $\hat{\mathbf{p}}$ . Additionally, in many relevant settings, microswimmers are smaller than the smallest hydrodynamic scales (such as the Kolmogorov length scale in turbulence). In this limit, the spinning and tumbling of the particle orientation can be described by Jeffery's equation [16], which takes the form

$$\dot{\hat{\mathbf{p}}} = \frac{1}{2} \boldsymbol{\omega} \times \hat{\mathbf{p}} + \alpha (\mathbf{S} \hat{\mathbf{p}} - \hat{\mathbf{p}}^T \mathbf{S} \hat{\mathbf{p}}). \quad (3.2)$$

Here,  $S_{ij} = (\partial_i u_j + \partial_j u_i)/2$  is the strain tensor and  $\boldsymbol{\omega} = \nabla \times \mathbf{u}$  the vorticity. The ratio between the ellipsoid's major and minor axes  $\lambda$  defines the shape parameter as  $\alpha = (\lambda^2 - 1)/(\lambda^2 + 1)$ . The parameter  $\alpha$  interpolates shapes between an oblate ellipsoid ( $-1 < \alpha < 0$ ), a sphere ( $\alpha = 0$ ), or a prolate ellipsoid ( $0 < \alpha < 1$ ).

#### 3.1.2 Two-dimensional vortex flow

In two spatial dimensions, (3.1) and (3.2) have three degrees of freedom: two coordinates for position and one swimming angle

$$\mathbf{x} = \begin{pmatrix} x \\ y \end{pmatrix}, \quad \hat{\mathbf{p}} = \begin{pmatrix} \cos \theta \\ \sin \theta \end{pmatrix}. \quad (3.3)$$

It is also worth noting that in two dimensions ellipsoids can only tumble. In the following, we restrict ourselves to an axisymmetric vortex flow of the form  $\mathbf{u}(t, \mathbf{x}) = u(r) \hat{\mathbf{e}}_\phi$ , where  $r = \sqrt{x^2 + y^2}$  is the radial coordinate and  $\hat{\mathbf{e}}_\phi$  a unit vector along the angular coordinate. By inserting (3.3) into (3.1) and (3.2), we obtain the equations of motion

$$\dot{x} = v_s \cos \theta - \frac{u(r)}{r} y, \quad (3.4)$$

$$\dot{y} = v_s \sin \theta + \frac{u(r)}{r} x, \quad (3.5)$$

$$\begin{aligned} \dot{\theta} = & \frac{1}{2r} \frac{d}{dr} [r u(r)] + \alpha \frac{1}{2r} \frac{d}{dr} \left[ \frac{u(r)}{r} \right] \\ & \times [(x^2 - y^2) \cos(2\theta) + (2xy) \sin(2\theta)]. \end{aligned} \quad (3.6)$$

Inspection of these equations in polar coordinates reveals rotational invariance. Without loss of generality, the dynamics of the system can therefore be reduced by one degree of freedom by transforming into a co-rotating frame. This is achieved by introducing new coordinates

$$\begin{pmatrix} X \\ P \end{pmatrix} = \begin{pmatrix} \cos \theta & \sin \theta \\ -\sin \theta & \cos \theta \end{pmatrix} \begin{pmatrix} x \\ y \end{pmatrix}. \quad (3.7)$$

In the co-rotating coordinate system  $\{X, P\}$ , the microswimmers are rotated so that they swim along the positive  $X$  axis. That is, in this new frame the microswimmer position and orientation differ only by a rotation from the laboratory frame  $\{x, y\}$ . Hence, the radial coordinate is identical in both coordinate systems,

$$r = \sqrt{x^2 + y^2} = \sqrt{X^2 + P^2}. \quad (3.8)$$

Introducing an angle variable defined through  $\tan \psi := P/X$  helps in the description of the dynamics. The equations of motion for  $X$  and  $P$  can be obtained from (3.4)-(3.7) as

$$\dot{X} = v_s + P f(r) [1 + \alpha h(\psi)], \quad (3.9)$$

$$\dot{P} = -X f(r) [1 + \alpha h(\psi)], \quad (3.10)$$

where

$$f(r) := \frac{r}{2} \frac{d}{dr} \left[ \frac{u(r)}{r} \right] \quad \text{and} \quad h(\psi) := \cos(2\psi). \quad (3.11)$$

The function  $f(r)$  contains the dependence on the velocity field  $u(r)$ . Vorticity and strain alter microswimmer orientation. While vorticity affects all microswimmers independent of their shape, the effect of strain is shape-dependent. The function  $h(\psi)$  is a geometric term stemming from the relative orientation of an ellipsoid with respect to the strain tensor.

The swimming orientation angle  $\theta$  is a slave variable to  $X$  and  $P$  and evolves according to the equation

$$\dot{\theta} = \frac{u(r)}{r} + f(r) [1 + \alpha h(\psi)]. \quad (3.12)$$

Hence, this co-rotating representation reduces the three-dimensional dynamics of the microswimmers in the laboratory frame  $\{x, y, \theta\}$  to an effective two-dimensional dynamics in the co-rotating frame  $\{X, P\}$ . In general, a particle's tumbling rate is defined as  $\dot{\theta}^2$ . In our parametrization (3.3), the tumbling rate simplifies to  $\dot{\theta}^2$ , and therefore can be directly determined from the swimming-angle dynamics (3.12). For spherical microswimmers, the tumbling rate only depends on the radial coordinate, while (3.12) shows that strain additionally induces orientation-dependent tumbling for ellipsoidal microswimmers.

As a concrete example, we consider a stationary Lamb-Oseen vortex, a prototypical vortex structure which is representative for a large class of hydrodynamic vortices [43]. The essential feature of this field is that the velocity profile interpolates between linear growth near the core (corresponding to a solid body rotation) and a Gaussian decay far from the core, leading to differential rotation. Its velocity field is given by

$$u(r) = u_0 \frac{r_0}{r} \left( 1 + \frac{1}{2\sigma} \right) \left( 1 - \exp \left[ \frac{-\sigma r^2}{r_0^2} \right] \right) \quad (3.13)$$

where  $u_0$  and  $r_0$  are the maximum azimuthal velocity and its corresponding radial coordinate. The vortex is stationary, and hence its width  $r_0$  is kept fixed. The constant  $\sigma$  is the nontrivial solution to the equation  $\exp(\sigma) = (1 + 2\sigma)$  [87], which is obtained by fixing  $u_0$  to  $r_0$ . The velocity and vorticity profiles are illustrated in figure 3.1.

Using  $r_0$  and  $r_0/u_0$  as length and time scales, respectively, (3.4)-(3.6) and (3.9)-(3.13) can be non-dimensionalized:  $x \rightarrow r_0 \tilde{x}$ ,  $y \rightarrow r_0 \tilde{y}$ ,  $X \rightarrow r_0 \tilde{X}$ ,  $P \rightarrow r_0 \tilde{P}$ ,  $t \rightarrow r_0/u_0 \tilde{t}$ ,  $u \rightarrow u_0 \tilde{u}$ . As a result, we have a non-dimensional swimming velocity  $\tilde{v}_s = v_s/u_0$ . In the following, we drop the tildes and work with the non-dimensionalized swimming speed.

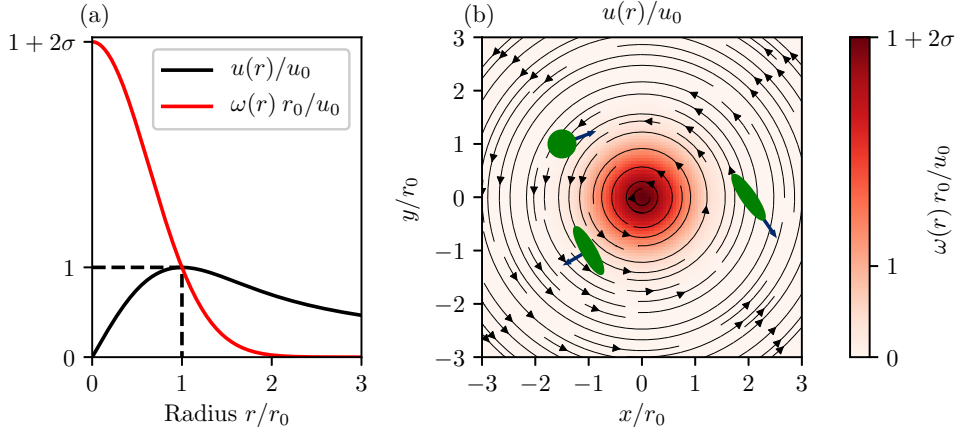


Figure 3.1: To illustrate our results, we choose a Gaussian vortex, the stationary Lamb-Oseen vortex (3.13). (a): Velocity and vorticity profile as a function of radius. (b): Streamline plot of the velocity field with vorticity shown as color-coded background. In our system ellipsoidal microswimmers can self-propel and are also advected by the vortex flow.

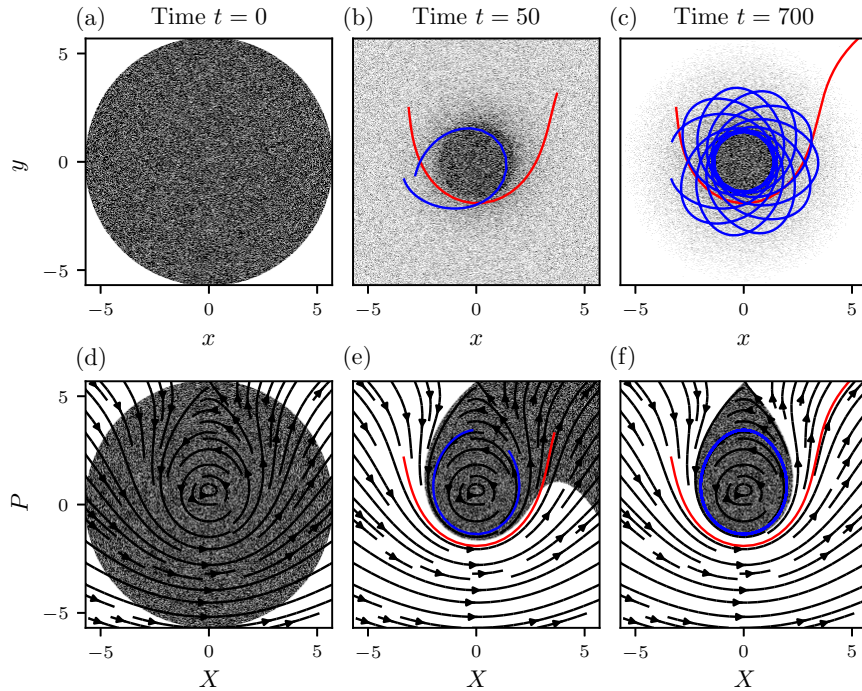


Figure 3.2: (a)-(c): A spherical ( $\alpha = 0$ ) microswimmer ensemble (gray density plot) homogeneously initialized in a disk in the laboratory frame  $\{x, y, \theta\}$  quickly separates into bound and unbound microswimmers. Example trajectories of bound and unbound microswimmers are given in blue and red, respectively. Trapped microswimmers remain near the vortex core and follow quasi-periodic orbits. A non-trivial microswimmer distribution develops. (d)-(f): An analysis in the co-rotating frame  $\{X, P\}$  reveals the phase-space structure of the dynamics.

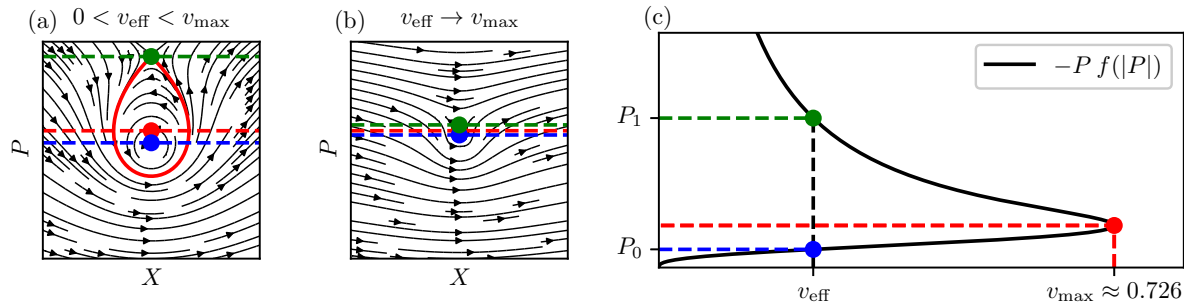


Figure 3.3: (a) Solving (3.14) and classifying the fixed points for microswimmers in a Lamb-Oseen vortex yields a saddle (green)-center (blue) fixed-point pair. The topology of phase space can be described as a function of an effective swimming velocity  $v_{\text{eff}}$  (3.16). (b) By increasing  $v_{\text{eff}}$ , the fixed points converge and undergo a saddle-node bifurcation at  $v_{\text{max}}$  (red dot). For  $v_{\text{eff}} > v_{\text{max}}$ , no fixed-point pair exists, and hence no closed trajectories are found. (c) The bifurcation diagram showing the fixed-point coordinates (3.14) reveals the role of  $v_{\text{eff}}$  as the control parameter for this system.

For the numerical results, we integrate the ordinary differential equations (3.4)-(3.6) using a fourth-order Runge-Kutta method with a time step  $dt = 0.05$ . For each of the simulations shown in figure 3.2 and figure 3.5, we initialized  $5 \times 10^5$  microswimmers. For the radial distribution function in figure 3.6, we initialized  $8 \times 10^6$  microswimmers.

Typical dynamics of microswimmers following (3.4)-(3.6) and the corresponding representation in the co-rotating frame  $\{X, P\}$  are shown in figure 3.2. Here, the quasi-periodic trajectories observed in the laboratory frame can be explained by the coupling of the typical angular velocity of the microswimmers in the co-rotating frame with their rotation frequency given by (3.12).

In the next section, we explore the features of (3.9) and (3.10) to uncover the fixed-point structure of the underlying dynamics and precisely characterize the observed phenomena of the microswimmers.

## 3.2 Fixed-point analysis

Visual inspection of the microswimmer dynamics in the co-rotating frame in figure 3.2 reveals an intricate behavior. These observations can be made precise by a fixed-point analysis. Because the dynamical system (3.9)-(3.10) is two-dimensional, the Poincaré-Bendixson theorem [88] applies, and the topology of the dynamics is completely determined by the fixed points. Already in figure 3.2 (d)-(f) we can visually identify two fixed points in phase space. These fixed points are marked as blue and green dots in figure 3.3 (a) and (b), and are studied in the following.

Calculating the fixed points  $\{X_{\text{FP}}, P_{\text{FP}}\}$  of (3.9)-(3.10) trivially leads to  $X_{\text{FP}} = 0$  for any axisymmetric flow profile. As a consequence,  $r = |P_{\text{FP}}|$  and  $\psi = \text{sign}(P_{\text{FP}}) \pi/2$ . For the subsequent analysis we use the specific example of the Lamb-Oseen vortex (3.13), but the theoretical results are valid in general. For the Lamb-Oseen vortex (3.13), we find that the inequality  $f(r) \leq 0$  is valid for all radii. This means that fixed points exist only for  $P_{\text{FP}} > 0$

and  $\psi = \pi/2$ . The fixed points of (3.9)-(3.10) are then given by the solutions to

$$\begin{aligned} 0 &= X_{\text{FP}}, \\ \frac{v_s}{1-\alpha} &= -P_{\text{FP}} f(|P_{\text{FP}}|). \end{aligned} \quad (3.14)$$

The type of fixed points of a two-dimensional system is determined by the determinant and the trace of its Jacobian matrix  $J$  [88]. At the fixed-point coordinates (3.14) we obtain

$$\begin{aligned} \text{Tr}(J) &= 0, \\ \det(J) &= (1-\alpha)^2 f(r) \left. \frac{d[r f(r)]}{dr} \right|_{r=|P_{\text{FP}}|}. \end{aligned} \quad (3.15)$$

These quantities reveal the nature of the fixed points and their dependence on microswimmer shape. Because  $\det(J) \in \mathbb{R}$  and  $\text{Tr}(J) = 0$ , this type of system can only have either center or saddle points. As a consequence, trajectories remaining bound to the vortex core correspond to areas in phase space enclosed by the homoclinic or heteroclinic orbits of the saddle points. All other areas in phase space lead to and come from infinity. Moreover, (3.14) motivates the definition of an effective swimming velocity as

$$v_{\text{eff}} := \frac{v_s}{1-\alpha}. \quad (3.16)$$

As the trace and determinant of  $J$  are independent of the swimming speed  $v_s$ , and the term  $(1-\alpha)^2$  in (3.15) is non-negative, microswimmers with the same effective swimming velocity have identical types of fixed points located at the same coordinates. This implies that the effective swimming velocity can be used to classify microswimmers according to their shape and swimming speed. Therefore,  $v_{\text{eff}}$  plays the role of a control parameter for the topology of the phase space. To obtain the bifurcation diagram of this system, the equation

$$v_{\text{eff}} = -P_{\text{FP}} f(|P_{\text{FP}}|) \quad (3.17)$$

can be solved graphically. The solution to this equation for the Lamb-Oseen vortex (3.13) is shown in figure 3.3 (c). In the case of the Lamb-Oseen vortex (figure 3.3) the condition  $0 < v_{\text{eff}} < v_{\text{max}}$  ensures the existence of a solution pair to (3.14), which corresponds to a center-saddle pair. As long as this solution exists, so does the homoclinic orbit, enclosing a region of trapped microswimmers. figure 3.3 (a) shows the fixed-point pair and the homoclinic orbit. By choosing a larger value for  $v_{\text{eff}}$ , as in figure 3.3 (b), the fixed points merge and undergo a saddle-node bifurcation at  $v_{\text{max}}$ .

The condition  $v_{\text{eff}} < v_{\text{max}}$  defines a region in the  $\{v_s, \alpha\}$  parameter space for which microswimmers are trapped, as shown in figure 3.4. The transition from bound to unbound microswimmers occurs at  $v_{\text{eff}} = v_{\text{max}}$ , which defines a straight line in  $\{v_s, \alpha\}$  parameter space. For the Lamb-Oseen vortex, we numerically obtain  $v_{\text{max}} \approx 0.726$  as the maximum of (3.17). Hence, by taking into account the role of shape, microswimmers with much lower swimming velocity  $v_s$  than the maximum fluid velocity  $u_0$  can escape the vortex. Additionally, prolate microswimmers can more easily escape the vortex core than oblate microswimmers. That is, the transition from bound to unbound microswimmers takes place at lower swimming velocity for prolate microswimmers than for oblate microswimmers. Furthermore, for constant  $v_s$ , thin elongated microswimmers have a divergent  $v_{\text{eff}}$  in the limit  $\alpha \rightarrow 1$ , and hence always escape the vortex in this limit.

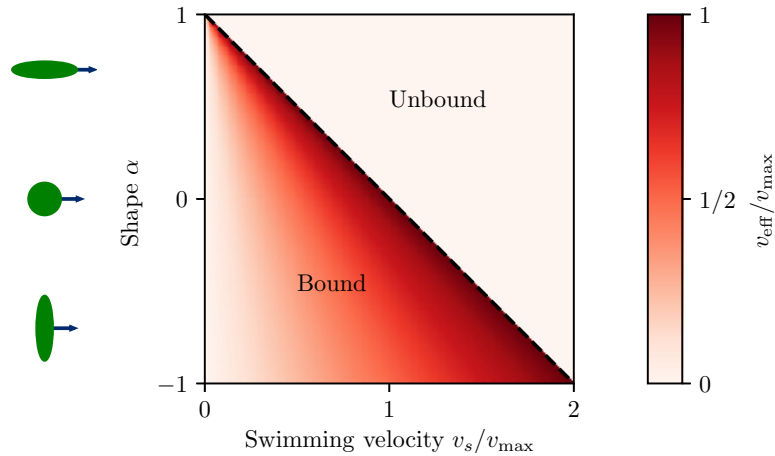


Figure 3.4: The condition  $v_{\text{eff}} < v_{\text{max}}$  defines a region in  $\{v_s, \alpha\}$  parameter space for which bound microswimmer trajectories exist. The effective velocity  $v_{\text{eff}}$  is color-coded and takes the value  $v_{\text{max}}$  at the transition. The transition from bound to unbound microswimmers defines a straight line in  $\{v_s, \alpha\}$  parameters space. The transition for prolate microswimmers ( $\alpha > 0$ ) occurs at lower  $v_s$  than for oblate microswimmers ( $\alpha < 0$ ), and hence prolates can more easily escape the vortex core. Furthermore, in the limit  $\alpha \rightarrow 1$  the region of bound microswimmers vanishes, and all microswimmers in this shape limit can escape the vortex core.

### 3.3 Hamiltonian dynamics and phase-space contraction

Next, we explore the effect of shape on the microswimmer dynamics and its relation to phase-space contraction. Initializing microswimmers homogeneously inside the homoclinic orbit leads to shape-dependent stationary distributions, as shown in figure 3.5. For equal effective swimming velocity  $v_{\text{eff}}$ , changing shape leads to a variety of density distributions.

To elucidate this, we begin by considering spherical microswimmers ( $\alpha = 0$ ). It is well known that, in general, equations for spherical microswimmers following (3.1) and (3.2) conserve phase-space volume [34, 37, 69]

$$\nabla_{\mathbf{x}} \cdot \dot{\mathbf{x}} + \nabla_{\hat{\mathbf{p}}} \cdot \dot{\hat{\mathbf{p}}} = 0. \quad (3.18)$$

An even stronger statement can be made in our case. By using the  $\{X, P\}$  coordinates of the co-rotating frame, we can reveal the Hamiltonian structure of the equations of motion, i.e.

$$\dot{X} = \frac{\partial H(X, P)}{\partial P}, \quad (3.19)$$

$$\dot{P} = -\frac{\partial H(X, P)}{\partial X}, \quad (3.20)$$

where the Hamilton function is given by

$$H(X, P) = v_s P + \int^r s f(s) ds \quad (3.21)$$

for arbitrary axisymmetric velocity fields. As a consequence of the Hamiltonian dynamics, phase-space volume is conserved and does not contract or expand. Therefore, starting from a homogeneous distribution, spherical microswimmers maintain a homogeneous distribution as time evolves.

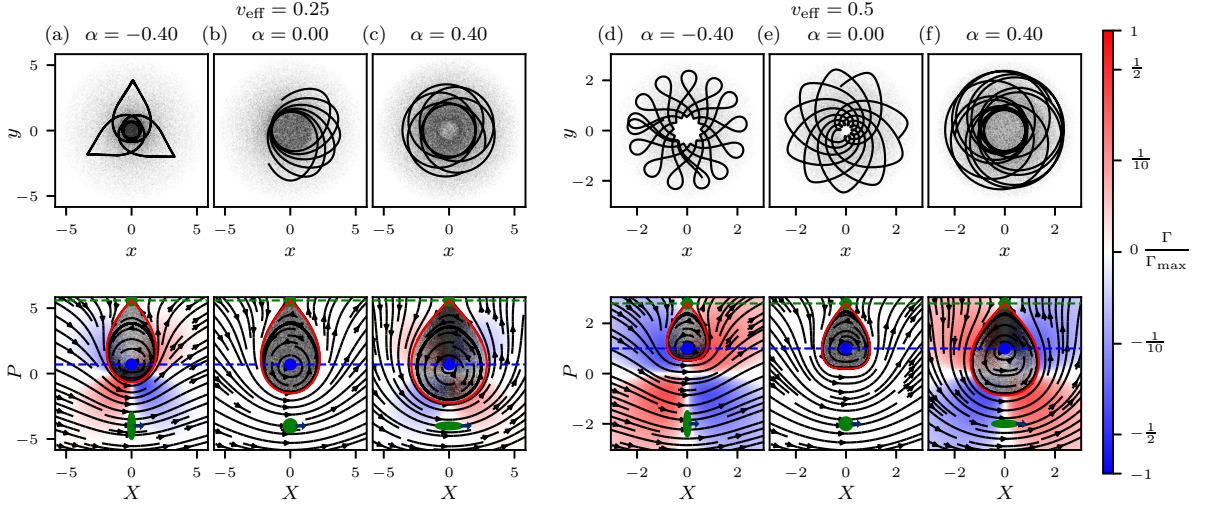


Figure 3.5: Bound microswimmers develop non-trivial density distributions. The gray scale shows the density of the microswimmer distribution. We show density distributions of different shapes and effective swimming velocities, namely  $v_{\text{eff}} = 0.25$  in (a)-(c) and  $v_{\text{eff}} = 0.5$  in (d)-(f). The black lines show sample trajectories. For spherical shapes (b,e), we clearly observe a homogeneous distribution in  $\{X, P\}$  space, a consequence of the phase-space-conserving Hamiltonian dynamics. A homogeneously filled homoclinic orbit (red line) at the initial time will remain so throughout time evolution. Other shapes break the Hamiltonian structure, and phase-space contraction  $\Gamma$  (3.24) leads to preferential alignment of microswimmers with respect to the velocity field, as illustrated by the denser regions in  $\{X, P\}$ -space. Oblate microswimmers (a,d) tend to concentrate along the  $X$ -axis. Prolate microswimmers (c,f) tend to concentrate along the  $P$ -axis. This corresponds to preferential swimming perpendicular or parallel to the flow, respectively.

While spherical microswimmers obey Hamiltonian dynamics, other microswimmer shapes break the Hamiltonian structure. This can be seen by recasting (3.9) and (3.10) as

$$\dot{X} = \frac{\partial H(X, P)}{\partial P} + \alpha P f(r) h(\psi), \quad (3.22)$$

$$\dot{P} = -\frac{\partial H(X, P)}{\partial X} - \alpha X f(r) h(\psi). \quad (3.23)$$

As a result, phase space can contract or expand for non-spherical microswimmers. We show the stationary distributions of bound microswimmers in both the laboratory frame  $\{x, y, \theta\}$  and the co-rotating frame  $\{X, P\}$  in figure 3.5. The gray color scale corresponds to microswimmer density. In the co-rotating frame spherical microswimmers remain homogeneously distributed in time. However, non-spherical microswimmers show denser regions inside the homoclinic orbit. Moreover, prolate ellipsoids are more densely concentrated along the  $P$ -axis. This can be explained by analyzing the phase-space contraction induced by the microswimmer dynamics. The phase-space contraction rate is given by

$$\Gamma := \partial_X \dot{X} + \partial_P \dot{P} = 2 \alpha \sin(2\psi) f(r). \quad (3.24)$$

Non-spherical microswimmers have an orientation-dependent tumbling rate (3.12), which induces phase-space contraction (3.24). As a consequence, non-spherical microswimmers accumulate or deplete in regions of phase space and will depart from an initially homogeneous

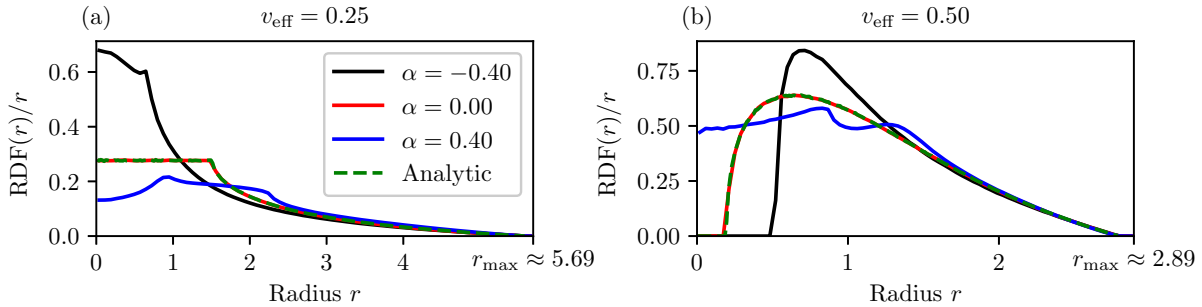


Figure 3.6: The clustering of bound microswimmer ensembles from figure 3.5 is characterized by their radial distribution functions (RDFs). Microswimmers with different shape but equal effective swimming velocity have equal maximum swimming radius  $r_{\max}$ , given by the saddle point ( $P_1$  in figure 3.3). Nevertheless, different shaped microswimmers exhibit different phase-space contraction rates, which leads to different RDFs. (a): For  $v_{\text{eff}} = 0.25$ , spherical microswimmers ( $\alpha = 0$ ) homogeneously fill an area around the origin. Because the radial distribution function is obtained by an angular integration over  $\{X, P\}$ -space, this leads to a linearly increasing RDF (i.e. constant  $\text{RDF}(r)/r$ ) for circular integration areas fully enclosed by the homoclinic orbit, i.e. for radii up to  $r \sim 1.6$ . Beyond this, the RDF starts to decay. Other shapes develop non-trivial RDFs. (b): At higher  $v_{\text{eff}}$  the vortex core may remain devoid of microswimmers. The analytic line corresponds to homogeneously filling the homoclinic orbit in the spherical case ( $\alpha = 0$ ) and integrating out the angle variable. This matches the RDF obtained from the dynamics.

distribution. Note that phase-space volume can locally contract and expand. However, integrating over the whole phase space reveals that the total phase-space volume is conserved. The fact that for the Lamb-Oseen vortex (3.13) the inequality  $f(r) \leq 0$  holds together with (3.24) implies a constant sign of  $\Gamma$  inside each quadrant in  $\{X, P\}$ -space. As trapped microswimmers traverse the different quadrants, they periodically switch between expanding and contracting quadrants. Microswimmers exiting an expansion quadrant will show a minimum in density, whilst those exiting a contraction quadrant will show maximum density. Hence, by considering the sign of  $\alpha$  and  $f(r)$ , we conclude that denser regions are formed along the  $X$ -axis for oblate ellipsoids and along the  $P$ -axis for prolate ellipsoids.

In figure 3.5 the different density regions for oblate and prolate microswimmers can be identified, as well as the homogeneous distribution for spheres. Recall that in the co-rotating coordinate frame  $\{X, P\}$ , the microswimmers are rotated so that they always point in the positive  $X$  direction. The velocity field, on the other hand, is rotationally invariant. Therefore contraction along the different axes reveals that oblate ellipsoids ( $\alpha < 0$ ) swim predominantly perpendicular to the velocity field (denser regions along the  $X$ -axis) while prolate ellipsoids ( $\alpha > 0$ ) mostly remain parallel to it (denser regions along the  $P$ -axis). That means that phase space contracts in such a way that, starting from random initial conditions, trapped microswimmers show shape-dependent preferential orientation parallel or perpendicular to the flow. Similar effects have been observed in chaotic, mildly turbulent flows [72].

Interestingly, the dynamical features of the microswimmers in the co-rotating frame lead to clustering in the laboratory frame. To characterize the spatial distribution of microswimmers, we consider the radial distribution function (RDF). As the laboratory frame  $\{x, y\}$  and the co-rotating frame  $\{X, P\}$  differ only by a rotation, the radial distribution of microswimmer

ensembles is identical in both cases. That means that integrating the distribution function in the co-rotating frame along the angle variable exactly corresponds to the RDF in the laboratory frame for any ensemble configuration. In the case of trapped spherical microswimmers ( $\alpha = 0$ ), starting from homogeneous initial conditions that fill out the homoclinic orbit (as in figure 3.2), the RDF is unaltered as time evolves. In this case, integrating a constant density inside the homoclinic orbit over the angle variable yields the RDF. Here, it is not necessary to integrate the equations of motion for an ensemble of microswimmers to obtain the stationary RDF; it can be obtained from the shape of the homoclinic orbit alone. For other microswimmer shapes this approach is not feasible, as phase-space contraction sets in under time evolution and a non-trivial stationary distribution develops.

Microswimmers with equal  $v_{\text{eff}}$  have the same type of fixed points at the same coordinates. Nevertheless, by changing shape, we observe a variety of quasi-periodic orbits and density distributions. These differences are rooted in the shape of the homoclinic orbit as well as the phase-space contraction rate  $\Gamma$ , which is shown in the background of figure 3.5, normalized by the maximum contraction rate  $\Gamma_{\text{max}} := 2 \max(|f(r)|)$ . Therefore, the RDF of bound microswimmers is a function of both phase-space contraction and the shape of the homoclinic orbit. Both of these differ for microswimmers of different shape and swimming speed, even if their effective swimming speed is identical (see figure 3.6). However, the maximum swimming radius  $r_0$  of trapped microswimmers, beyond which the RDF is zero, is a common property of microswimmers with identical effective swimming speeds. This can be explained by the fact that the saddle point is the point on the homoclinic orbit with the largest radius. Hence the saddle point determines the maximum swimming radius of trapped microswimmers, which is a constant for microswimmers of equal effective swimming speed.

### 3.4 Impact of rotational noise

So far, we have considered only deterministic microswimmers. In realistic biophysical settings, fluctuations play an important role. We explore this by considering the impact of rotational fluctuations on microswimmers. Let  $W$  be a Wiener process with mean zero and variance  $dt$ . We then introduce a stochastic term into (3.2) as

$$d\hat{\mathbf{p}} = \dot{\hat{\mathbf{p}}} dt + \hat{\mathbf{e}}_z \times \hat{\mathbf{p}} g dW, \quad (3.25)$$

where the deterministic part  $\dot{\hat{\mathbf{p}}}$  is given by (3.2) and  $dW$  is an increment of the Wiener process. Here we are using the non-dimensionalized quantities, such that a Péclet number can be defined as  $\text{Pe} := 1/g^2$ . This equation is understood in the Stratonovich sense so that  $\hat{\mathbf{p}}$  remains normalized. With the parametrization (3.3) the equations of motion for microswimmers with rotational noise correspond to additive noise on the swimming angle

$$dx = \dot{x} dt, \quad (3.26)$$

$$dy = \dot{y} dt, \quad (3.27)$$

$$d\theta = \dot{\theta} dt + g dW, \quad (3.28)$$

where again the deterministic parts  $\dot{x}$ ,  $\dot{y}$ , and  $\dot{\theta}$  are given by (3.4)-(3.6). A direct comparison with the deterministic equations reveals that rotational fluctuations enhance the particle's tumbling rate.

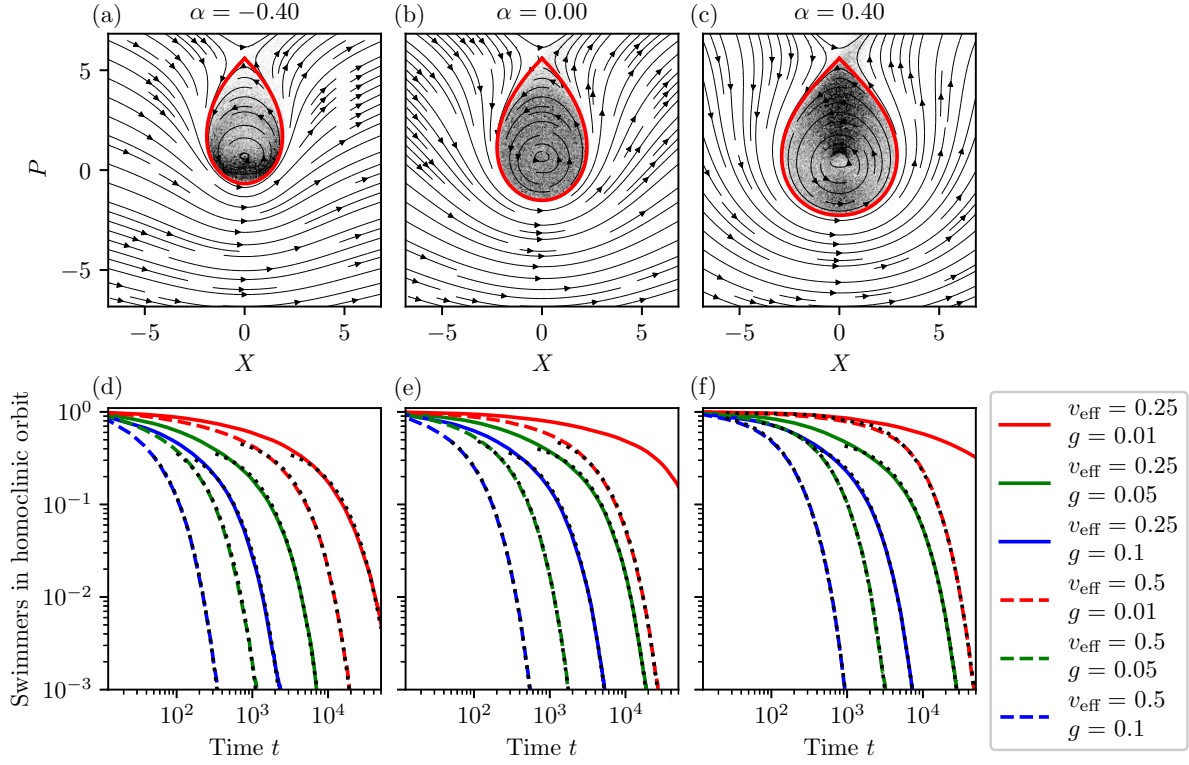


Figure 3.7: (a)-(c) Under the influence of rotational noise a microswimmers can escape the vortex core. The saddle point plays an important role here as the maximum expansion direction leads to microswimmers quickly leaving the vortex core. Snapshots taken at time  $t = 375$  for microswimmers with  $v_{\text{eff}} = 0.25$  and  $g = 0.01$ . (d)-(f) Number of microswimmers inside the homoclinic orbit as a function of time, normalized by the number of microswimmers in the homoclinic orbit at the initial time. For the same  $v_{\text{eff}}$ , prolate microswimmers are slower in escaping the vortex as their  $v_s$  is lower than for microswimmers of other shapes. For low values of the effective swimming velocity  $v_{\text{eff}}$  or rotational noise  $g$ , the number of microswimmers inside the homoclinic orbit decreases slowly. This is due to the microswimmers only drifting and diffusing slowly towards the saddle point. For higher values of both  $v_{\text{eff}}$  and  $g$ , this process happens much more quickly and is approximately described by exponential decay (black dots).

For the numerical results presented in this section, we solve (3.26)-(3.28) using the Euler-Maruyama method with a time step  $dt = 0.0005$  and a total of  $5 \times 10^5$  microswimmers. Switching to the co-rotating  $\{X, P\}$ -frame, we obtain the stochastic equations (in the Stratonovich sense) as

$$dX = \dot{X} dt + g P dW, \quad (3.29)$$

$$dP = \dot{P} dt - g X dW, \quad (3.30)$$

with  $\dot{X}$  and  $\dot{P}$  given by (3.9) and (3.10). The effect of noise in the co-rotating frame corresponds to rotational diffusion. This can be seen from the Fokker-Planck equation for the density distribution function  $\rho(t, X, P)$

$$\partial_t \rho = -v_{\text{eff}}(1 - \alpha) \partial_X \rho + \mu \rho - \Gamma \rho + \frac{g^2}{2} D \rho \quad (3.31)$$

where  $\Gamma$  is the phase-space contraction rate (3.24) and  $\mu$  is a rotational drift operator

$$\mu := f(r)[1 + \alpha h(\psi)](X\partial_P - P\partial_X) = f(r)[1 + \alpha h(\psi)]\partial_\psi. \quad (3.32)$$

Additionally  $D$  is a diffusion operator given by

$$D := (X\partial_P - P\partial_X)(X\partial_P - P\partial_X) = \partial_\psi\partial_\psi. \quad (3.33)$$

Setting  $g = 0$  in (3.31) yields a Liouville equation for the deterministic part of the dynamics (3.9)-(3.10). For  $v_{\max} < v_{\text{eff}}$ , the drift term due to swimming dominates, and microswimmers always escape the vortex core. Without swimming ( $v_{\text{eff}} = 0$ ) only rotational drift is present, i.e. the microswimmers behave as passive tracers. In the regime  $0 < v_{\text{eff}} < v_{\max}$  the presence of the fixed-point pair and the homoclinic orbit leads to a stationary solution to the Liouville equation, corresponding to stationary distributions as shown in figure 3.5.

Enhanced tumbling rates due to the addition of rotational noise on the swimming direction lead to rotational diffusion (3.33) in the co-rotating frame. This induces microswimmer transfer across the homoclinic orbit. Therefore, starting from a stationary distribution of microswimmers in the homoclinic orbit, all microswimmers will eventually escape the vortex core. figure 3.7 illustrates this phenomenon for various microswimmer shapes. The saddle point plays an important role in this context: the maximum expansion direction at this fixed point leads to enhanced escape rates, allowing microswimmers to escape the vortex core faster than they would do with just rotational diffusion. For a constant  $v_{\text{eff}}$ , we observe that oblate ellipsoids escape the homoclinic orbit faster than prolate ellipsoids. This is due to the fact that for constant  $v_{\text{eff}}$  prolate microswimmers swim slower than oblate microswimmers.

### 3.5 Summary and conclusions

We have studied self-propelled ellipsoidal particles as idealized microswimmers in a two-dimensional axisymmetric vortex flow. In particular, we have investigated under which conditions microswimmers are trapped by the vortex, and whether they exhibit preferential orientation. This simple setting reveals interesting insights: due to the axisymmetry of the problem, the phase space is two-dimensional and can be parameterized by the microswimmer's radial position and an orientation angle (relative to the position vector). Topologically, the phase space features a saddle point and a center. Microswimmers bound to the vortex core follow closed orbits inside a homoclinic orbit. Clustering in the laboratory frame occurs as a consequence of phase-space contraction. Shape plays a decisive role: for spherical microswimmers, we have shown that the dynamics are Hamiltonian, excluding clustering as a result of phase-space conservation. However, non-spherical particles break the Hamiltonian structure, hence enabling phase-space contraction and shape-induced clustering.

To determine whether microswimmers are trapped, we identified the effective swimming velocity as the central control parameter. The effective swimming velocity depends both on the swimming velocity and on the shape: at a constant swimming velocity, prolate ellipsoids have a larger effective swimming velocity than oblate ellipsoids. This allowed us to map different microswimmer shapes to topologically equivalent phase spaces. Using bifurcation analysis, we determined the maximum velocity for a given flow profile such that microswimmers faster than this velocity are fast enough to escape the vortex core. Notably, this maximum velocity is lower than the maximum azimuthal flow velocity, implying that microswimmers with a smaller swimming velocity than the advecting flow field can escape the vortex. Shape plays a

role also here as prolate microswimmers can more easily escape than oblate microswimmers. As the shapes of many plankton and bacteria species can be approximated as thin rods [86], this effect may have implications for motile species in aquatic environments. In particular, a prolate shape may yield advantages such as avoiding hydrodynamic trapping while grazing or escaping predation, without having to dedicate additional energy to swim faster.

Finally, we investigated the impact of rotational noise. We find that the inclusion of rotational noise allows for initially trapped microswimmers to escape the vortex core. The presence of the saddle point leads to enhanced escape rates as the maximum expansion direction quickly drives microswimmers away from the vortex core.

While we focused on the simple case of an axisymmetric flow, our results might help to also better understand the impact of shape and motility on microswimmer dynamics in more complex flows.

### **Aknowledgements**

This work was supported by the Max Planck Society. MW also gratefully acknowledges a Fulbright-Cottrell Award grant. The authors thank Ramin Golestanian for helpful discussions.

---

Part II

---

Dispersion and collision of motile  
ellipsoids

---

# Dispersion statistics and collision rates of motile ellipsoidal particles in mild turbulence

## 4.1 Introduction

Plankton in the ocean is an example of microscopic organisms in a fluid flow. These organisms form an integral part of the global carbon and nitrogen cycles. Understanding their interaction with the turbulent flow is therefore ecologically relevant. Motility allows organisms to consume internal chemical energy to self-propel in a fluid. This is one of the main mechanisms that enables cell migration. Furthermore, cell shape is a critical parameter governing the cell behavior in the fluid; particle shape prescribes how the small-scale features of the flow induce particle spinning and tumbling. For motile plankton species, motility and shape are hence the critical parameters which determine the behavior of the plankton cell in the fluid flow.

In the ocean, microscopic plankton are found in a wide variety of shapes and different motile capabilities (figure 4.1). In order to survive, plankton need to graze, mate, and evade predation. From a physical perspective this opens several research approaches to a mechanistic study of microscopic swimming in the ocean. For example, studying the transport properties of microorganisms in turbulence is a simple mechanistic approach to quantify grazing or evading predation. In which way shape, motility, or other parameters such as density interact in this intricate system is a complex question. Mechanistic approaches to study these organisms have revealed both complex small-scale viscous hydrodynamics [63], as well as large-scale oceanic effects [6]. Here we will use a numerical approach to study motile microorganisms in direct numerical simulations of a turbulent fluid flow.

As discussed in the classic review paper by Pedley and Kessler [15] microorganism shape can be parametrized as ellipsoidal. The rotation dynamics of these microorganisms are governed by the Jeffery's equations [16]. This leads to a minimal modeling scheme which allowed for a physical approach to the interaction between a microorganism and the surrounding fluid flow. The peculiar features of such microorganisms, such as motility [18–23, 90], gyrotaxis [24, 33–38, 40, 91, 92], and sedimentation [25–30] cause novel and complex behavior of particles in a turbulent flow compared to passive particles in turbulence. In the present chapter, we will

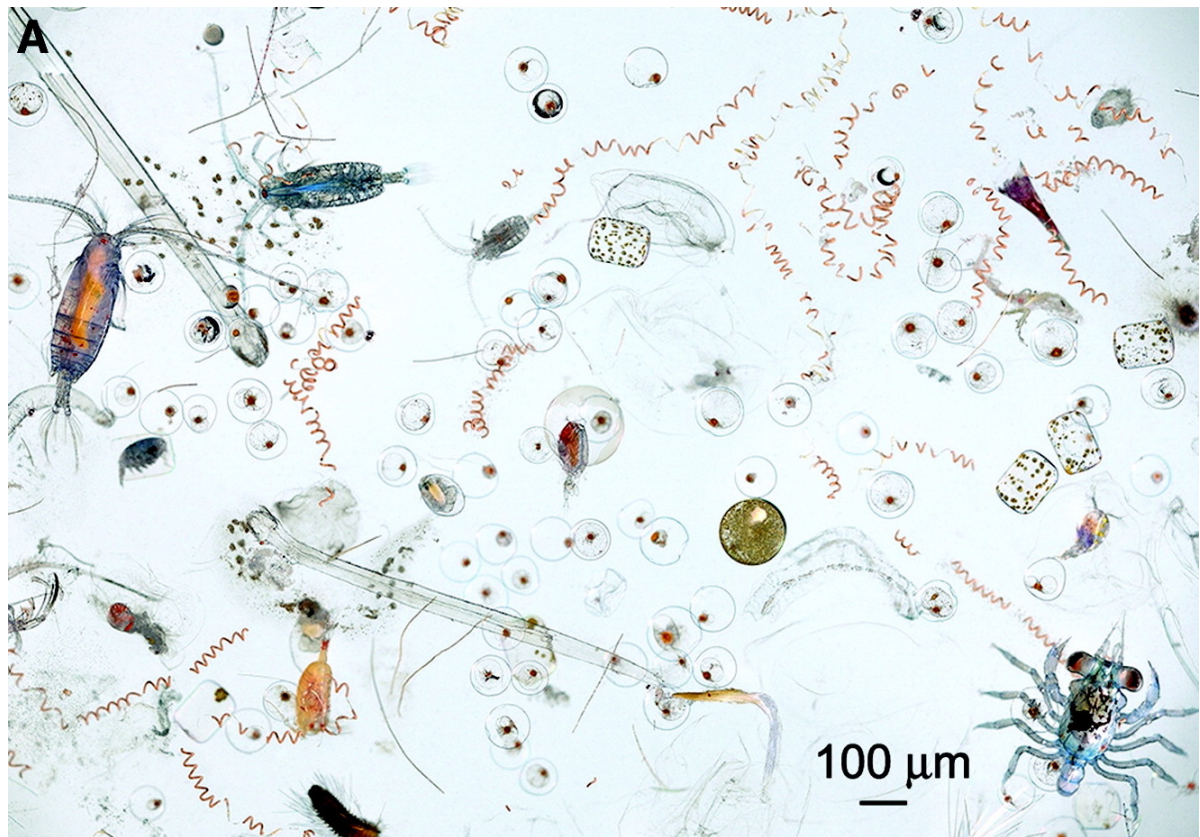


Figure 4.1: Taking a look at ocean water under the microscope reveals the vast diversity of planktonic organisms present in the water. These plankton species come in a wide variety of shapes and sizes. Some species are motile; motility influences transport properties and collision rates of plankton in the turbulent ocean. Figure taken from [89].

concentrate on motile microorganisms, and study their rotation rates, transport properties, and collision rates in a turbulent flow, focusing on small-scale effects.

Rotation rates of complex particles have been an active field of research with applications in diverse disciplines, including the dynamics of microswimmers. Orientational dynamics of ellipsoids have revealed intricate shape-dependent orientation statistics [74, 77, 93–96]. One of the main research areas scientists focus on is understanding the rotational statistics as a function of ellipsoid shape [51]. It has been found, for example, that prolate ellipsoids tend to orient with the vorticity vector [51, 75, 76, 97–99], while oblate ellipsoids rotate perpendicular to it [73]. That is, prolate ellipsoids spin, while oblate ellipsoids tend to mostly tumble [100]. Analytical asymptotic approaches have revealed the shape dependence on the rotation of motile ellipsoids [72] and shown that prolate ellipsoids tend to align with the local velocity field. Furthermore, adding motility has introduced additional complexity to these systems. For instance, shape dependent rotation rates lead to different spatial distributions [17, 19, 23] and transport properties [24, 36, 38, 101] than their non-motile counterparts. One of the main consequences of these intrinsic particle properties is their effect on particle collision rates.

A critical quantity for microscopic organisms in turbulence are collision properties as a function of shape and motility, since they determine the rate of encounters relevant for questions regarding reproduction, predation, and grazing, for example. Collision rates of complex par-

ticles have also been measured in a variety of systems. In cloud microphysics [57, 102, 103], for example, shape and size dependent collision rates play a big role in particle clustering and growth, leading to rain droplet formation and growth. When studying the collision rates of planktonic organisms the effect of motility turned out to be critical in determining collision rates [104, 105], while at the same time, the geometry of the colliding particles plays a crucial role in fixing collision rates [106].

Despite this extensive range of works, a comprehensive analysis of the effect of both shape and motility on collision rates and dispersion statistics is currently missing. We intend to do this here. We start by introducing our modeling approach: we study self-motile ellipsoids in a mildly turbulent flow by use of numerical simulations. We then look at rotation statistics of motile ellipsoids, and compare with the non-motile case as a function of shape and motility. Subsequently, we investigate transport properties of these motile particles and quantify their shape dependent short- and long-time dispersion. Finally, we discuss the collision rates of thin disks, spheres, and slender rods. We measure the transition from non-motile to motile collision rates and quantify the effect of motility in enhancing collision rates as a function of shape.

## 4.2 Theory and methods

In this section we will introduce the relevant theoretical background to set into context the results in the sections below. First of all, we introduce the equations of motion. Subsequently we review the rotation statistics of passive ellipsoids in turbulence. For collision rates and collision kernel we refer to the relevant theory section of this dissertation 2.3.

### 4.2.1 Equations of motion

In the following we will consider a turbulent fluid obtained by directly solving the incompressible Navier-Stokes equations

$$\frac{\partial \mathbf{u}}{\partial t} + \mathbf{u} \cdot \nabla \mathbf{u} = -\nabla p + \nu \Delta \mathbf{u} + \mathbf{f}, \quad (4.1)$$

$$\nabla \cdot \mathbf{u} = 0. \quad (4.2)$$

Here,  $\mathbf{u}$  is the three-dimensional velocity field,  $p$  denotes the kinematic pressure, and  $\nu$  is the kinematic viscosity. A large-scale forcing  $\mathbf{f}$  drives the flow to ensure a statistically stationary state. Our modeling approach is as follows. We consider self-propelled microswimmers with a constant swimming velocity  $v_s$  in the swimming direction  $\hat{\mathbf{p}}$  [15]. Additionally, the fluid flow  $\mathbf{u}$  advects the microswimmers. The resulting equation of motion for the microswimmer position reads

$$\dot{\mathbf{x}} = \mathbf{u} + v_s \hat{\mathbf{p}}. \quad (4.3)$$

Furthermore, the small-scale features of the flow, strain rate  $\mathbf{S} = \mathbf{S}(\mathbf{x}, t)$  and vorticity  $\boldsymbol{\omega} = \boldsymbol{\omega}(\mathbf{x}, t)$ , induce solid body rotation of the particles. In order to model these effects, we take the following simplifications. We consider microswimmers which are smaller than or comparable to the Kolmogorov scale of the flow, i.e. the smallest turbulent scale in a flow. Additionally, we idealize microswimmers as axially symmetric ellipsoids. Moreover, we set the swimming direction along the same direction as the ellipsoid's symmetry axis. With these simplifications the microswimmer orientation  $\hat{\mathbf{p}}$  follows Jeffery's equations [16], which read

$$\dot{\hat{\mathbf{p}}} = \frac{1}{2} \boldsymbol{\omega} \times \hat{\mathbf{p}} + \alpha (\mathbf{S} \hat{\mathbf{p}} - \hat{\mathbf{p}}^T \mathbf{S} \hat{\mathbf{p}} \hat{\mathbf{p}}). \quad (4.4)$$

Here,  $\alpha$  is a shape parameter which is defined as

$$\alpha = \frac{\lambda^2 - 1}{\lambda^2 + 1}, \quad (4.5)$$

where  $\lambda$  is the ratio between the ellipsoid's axis of symmetry and the other axes. As shown in figure 2.2, this parametrizes oblate ellipsoids ( $-1 < \alpha < 0$ ,  $\lambda < 1$ ), spheres ( $\alpha = 0$ ,  $\lambda = 1$ ) and prolate ellipsoids ( $0 < \alpha < 1$ ,  $\lambda > 1$ ). The microswimmer equations of motion (4.3) and (4.4) couple the rotation dynamics to the spatial evolution. It is notable that the spatial evolution by itself conserves the phase space spanned by position. On the contrary, the rotation dynamics contract or expand orientation phase space for non-spherical shapes. By coupling both of these equations, the total phase space spanned by position and orientation of the microswimmers can contract or dilate, i.e.  $\nabla_x \cdot \dot{\mathbf{x}} + \nabla_{\hat{\mathbf{p}}} \cdot \dot{\hat{\mathbf{p}}} \neq 0$ . This coupling of the rotation dynamics onto the spatial evolution of microswimmers leads to non-trivial spatial distributions [19, 23, 24, 36, 38, 101]. Below we will systematically analyze the transport properties of motile ellipsoidal microswimmers. Before that, however, we will first review the rotation statistics of passive ellipsoids in turbulence.

#### 4.2.2 Spinning and tumbling of non-motile particles

In a fluid flow strain and vorticity induce rotation of an ellipsoid. The Jeffery's equations (4.4) induce shape-dependent full-body rotation of the ellipsoid. Summing the rotation on all the axis of an ellipsoid leads to its full-body rotation [50, 74, 77], which we denote by  $\mathbf{\Omega}$  and which is given by

$$\mathbf{\Omega} = \frac{\boldsymbol{\omega}}{2} + \alpha \hat{\mathbf{p}} \times S \hat{\mathbf{p}}. \quad (4.6)$$

The full-body rotation can be split up into a component parallel and a component perpendicular to its symmetry axis, spinning and tumbling, respectively. Starting from equation (4.6), the spinning  $\Omega_p \hat{\mathbf{p}}$  and tumbling  $\hat{\mathbf{p}} \times \dot{\hat{\mathbf{p}}}$  can be recast as [77]

$$\mathbf{\Omega} = \Omega_p \hat{\mathbf{p}} + \hat{\mathbf{p}} \times \dot{\hat{\mathbf{p}}}. \quad (4.7)$$

Spinning is purely due to the local flow vorticity parallel to the ellipsoid's symmetry axis

$$\Omega_p = \frac{\boldsymbol{\omega} \cdot \hat{\mathbf{p}}}{2} = \frac{\omega_{\parallel \hat{\mathbf{p}}}}{2}. \quad (4.8)$$

Here  $\omega_{\parallel \hat{\mathbf{p}}}$  signifies the component of vorticity parallel to the swimming direction  $\hat{\mathbf{p}}$ . Similarly, using equation (4.4) the particle's tumbling can be obtained as

$$\hat{\mathbf{p}} \times \dot{\hat{\mathbf{p}}} = \frac{\omega_{\perp \hat{\mathbf{p}}}}{2} + \alpha \hat{\mathbf{p}} \times S \hat{\mathbf{p}}. \quad (4.9)$$

Here  $\omega_{\perp \hat{\mathbf{p}}}$  is the component of vorticity perpendicular to the swimming direction  $\hat{\mathbf{p}}$  (i.e.  $\mathbf{\Omega} - \hat{\mathbf{p}} \hat{\mathbf{p}} \cdot \mathbf{\Omega}$ ). Notably, for spherical shapes ( $\alpha = 0$ ) the tumbling and spinning are due purely to vorticity contributions. Due to symmetry considerations, for spheres the orientation vector  $\hat{\mathbf{p}}$  can be arbitrarily redefined. Hence, each possible rotation direction contributes in average the same. As tumbling has contributions from two rotation directions, while the other rotation direction contributes to spinning, for spheres the tumbling rate is twice as large as its spinning rate. For non-spherical shapes ( $\alpha \neq 0$ ) strain yields an additional contribution to the tumbling component. This shape-dependent contribution will be crucial later in determining particle

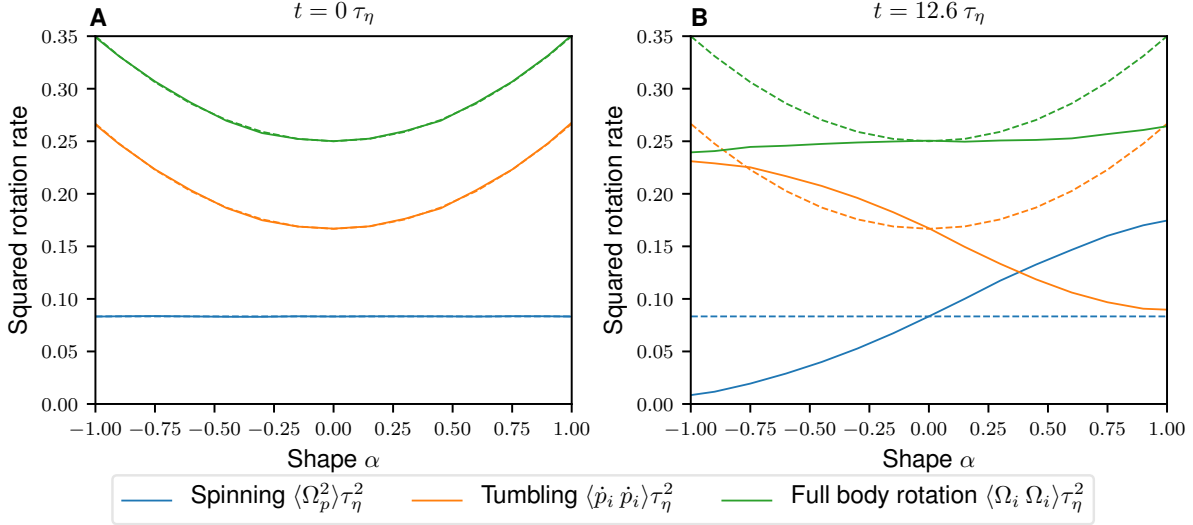


Figure 4.2: Spinning and tumbling statistics for passive ellipsoidal tracers. Dashed lines correspond to the analytic results for randomly oriented ellipsoids (4.14)–(4.16), i.e. the uncorrelated case. The filled lines were obtained from averages of ensembles of  $10^6$  particles. **A** Randomly homogeneously distributed isotropically oriented particles reproduce the rotation rates of the uncorrelated case. **B** After evolving for  $12.6 \tau_\eta$  in a Navier–Stokes flow the passive ellipsoids have non-trivial correlations with the fluid flow and shape-dependent rotation rates. Oblate ellipsoids mostly only tumble, while prolate ellipsoids spin more than they tumble.

diffusion rates.

A useful measure to quantify the ellipsoid’s rotation dynamics is the squared full body rotation rate (4.10). The squared magnitude of the full-body rotation rate factorizes into two contributions. There is a contribution due to the spinning rate  $\Omega_p^2$ , and another due to the tumbling rate  $\dot{\mathbf{p}}^2$

$$\Omega^2 = \Omega_p^2 + \dot{\mathbf{p}}^2. \quad (4.10)$$

Explicitly working out these terms from (4.8) and (4.9) yields

$$\Omega_p^2 = \frac{\omega_{\parallel \hat{\mathbf{p}}}^2}{4}, \quad (4.11)$$

$$\dot{\mathbf{p}}^2 = \frac{\omega_{\perp \hat{\mathbf{p}}}^2}{4} + \alpha (\hat{\mathbf{p}} \times \mathbf{S} \hat{\mathbf{p}}) \cdot [\boldsymbol{\omega} + \alpha (\hat{\mathbf{p}} \times \mathbf{S} \hat{\mathbf{p}})]. \quad (4.12)$$

The particle’s full body rotation rate can then be recast as

$$\Omega^2 = \frac{\omega^2}{4} + \alpha^2 (\hat{\mathbf{p}} \times \mathbf{S} \hat{\mathbf{p}})^2 + \alpha \boldsymbol{\omega} \cdot \hat{\mathbf{p}} \times \mathbf{S} \hat{\mathbf{p}}. \quad (4.13)$$

Let us now consider the statistics of an ensemble of ellipsoids in a turbulent flow. In the case of uncorrelated orientation  $\hat{\mathbf{p}}$  with strain and vorticity the averages can be worked out exactly [74, 76, 77, 99]. By taking ensemble averages, which we denote as  $\langle \cdot \rangle$ , in the uncorrelated case the particle orientation is totally uncorrelated from the local vorticity and strain rate. As a consequence the averages can be split up for example as  $\langle \hat{\mathbf{p}}_i \hat{\mathbf{p}}_j S_{jk} S_{lm} \rangle = \langle \hat{\mathbf{p}}_i \hat{\mathbf{p}}_j \rangle \langle S_{jk} S_{lm} \rangle$ . Then known averages from turbulence theory, such as  $\langle \boldsymbol{\omega}^2 \rangle = 1/\tau_\eta^2$  can be substituted, while

Resolution of simulated box	Reynolds number $\text{Re}_\lambda$	$k_{\max}\eta$	Forcing band	$u_{\text{rms}}/u_\eta$
$1024 \times 1024 \times 1024$	108	2.99	$k = 3 - 4$	9.13

Table 4.1: Simulation parameters used in this chapter.

the averages over the orientation vector can be resolved as  $\langle \hat{\mathbf{p}}_i \hat{\mathbf{p}}_j \rangle = \delta_{ij}/3$ . The uncorrelated rotation rates are then obtained as

$$\langle \Omega_p^2 \rangle \tau_\eta^2 = \frac{1}{12}, \quad (4.14)$$

$$\langle \dot{\hat{\mathbf{p}}} \cdot \dot{\hat{\mathbf{p}}} \rangle \tau_\eta^2 = \frac{1}{6} + \frac{1}{10} \left( \frac{\lambda^2 - 1}{\lambda^2 + 1} \right)^2 = \frac{1}{6} + \frac{\alpha^2}{10}, \quad (4.15)$$

$$\langle \Omega^2 \rangle \tau_\eta^2 = \frac{1}{4} + \frac{1}{10} \left( \frac{\lambda^2 - 1}{\lambda^2 + 1} \right)^2 = \frac{1}{4} + \frac{\alpha^2}{10}. \quad (4.16)$$

where  $\tau_\eta$  is the flow's Kolmogorov time. These rotation rates are observed, for example, when initializing a simulation with randomly oriented ellipsoids (see figure 4.2 **A**). After time passes, the rotational dynamics (4.4) lead to correlations between the ellipsoid orientation and strain and vorticity. As a consequence, the rotation rates of ellipsoids in turbulence differ from those of totally uncorrelated isotropically oriented ellipsoids. Statistical stationarity is obtained after around  $10 \tau_\eta$ . After this time, the rotation rates typical of passive tracers in turbulence are measured (see figure 4.2 **B**). Notably, here shape dependence sets in and produces different behaviors for oblate ellipsoids, spheres, and ellipsoids. In the range  $\alpha < -0.5$  ( $\lambda < 0.577$ ), oblate ellipsoids spin very little, and mostly only tumble. In a transition regime in the range  $-0.5 \leq \alpha < 0.5$  ( $0.577 \leq \lambda < 1.73$ ) oblates progressively spin more and tumble less, until the sphere case  $\alpha = 0$  ( $\lambda = 1$ ). As we saw above, due to symmetry arguments spheres tumble twice as much as they spin. For larger aspect ratios  $\alpha > 0$  ( $\lambda > 1$ ), prolate ellipsoids eventually spin more than they tumble, and after a cross-over at around  $\alpha \sim 0.32$  ( $\lambda \sim 1.4$ ) spinning becomes the dominant rotation rate.

### 4.2.3 Numerical simulations

To carry out our numerical studies we directly simulate the incompressible Navier-Stokes equations (4.2) using our in-house code TurTLE. We solve these equations in the vorticity formulation and obtain a fully resolved velocity field. Our code is a highly parallelized pseudo-spectral code, which allows for scaling of large simulations onto a computing grid. The simulation parameters are reported in table 4.1. We use statistically stationary velocity field as initial condition. A large scale forcing (see forcing band in table 4.1) ensures the statistical stationarity of the simulation.

Within our code, ensembles of particles of different shape and swimming speed are integrated simultaneously with the velocity field. We integrate particle position (4.3) and orientation (4.4) in time with an Adams-Bashford scheme. The code integrates the built-in parallelization into the managing of particles. The particle ensembles are distributed on the computing grid to ensure high performance.

Particles were initialized homogeneously distributed in space and isotropically oriented. Starting from these initial conditions we always took a transient of at least  $10\tau_\eta$  to ensure stationarity of the rotation rates. The only exception to this is panel **A** of figure 4.2, which shows the ro-

Range of shapes $\alpha$ ( $\lambda$ )	Range of swimming speeds $v_s/u_\eta$	Number of particles
-0.999 – 0.999 ( $2.24 \times 10^{-2} - 44.7$ )	0 – 33.1	$10^6$

Table 4.2: The parameter ranges scanned in section 4.3 and figure 4.2.

Range of shapes $\alpha$ ( $\lambda$ )	Range of swimming speeds $v_s/u_\eta$	Number of particles
-0.999 – 0.999 ( $2.24 \times 10^{-2} - 44.7$ )	0 – 10.5	$10^5$

Table 4.3: The range of parameters scanned in section 4.4 are shown in this table.

	Oblate ellipsoids	Spheres	Prolate ellipsoids
	$-1 < \alpha > 0$	$\alpha = 0$	$0 < \alpha < 1$
	$0 < \lambda < 1$	$\lambda = 1$	$\lambda > 1$
Axis of symmetry	$l\lambda$	$l$	$l$
Other axes	$l$	$l$	$l/\lambda$

Table 4.4: For collisions the relative size of the particles has to be specified. A given length is reported as  $l$ . Spheres have a diameter  $l$ , prolate ellipsoids have length  $l$  and width  $l/\lambda$ , and oblate ellipsoids have a diameter  $l$  and height  $l\lambda$ .

tation statistics of ellipsoids at initial conditions, i.e. in the uncorrelated state.

For the numerical results of section 4.3 and figure 4.2 we scanned shape and swimming speed according to table 4.2. For section 4.4 we scanned the parameters shown in table 4.3. In section 4.5 we measured collision rates of particles of different shape. For the collision algorithm is important to know how the particle shape is defined, as the collision between two particles depends on the particle geometry and orientation. In table 4.4 we define the ellipsoid axes in terms of a length parameter  $l$ . The shape and motility parameters we scanned in this section are reported in table 4.5.

Shape $\alpha$ ( $\lambda$ )	Swimming speeds $v_s/u_\eta$	Particle size $l/\eta$	Number of particles
-0.995 (0.05)	0 – 2.10	0.0952 – 0.952	$5.1 \times 10^5 - 1.6 \times 10^7$
0.0 (1.00)	0 – 2.10	0.0952 – 0.952	$5.1 \times 10^5 - 1.6 \times 10^7$
0.995 (20.0)	0 – 2.10	0.0952 – 0.952	$5.1 \times 10^5 - 1.6 \times 10^7$

Table 4.5: The range of parameters scanned in section 4.5 are shown here.

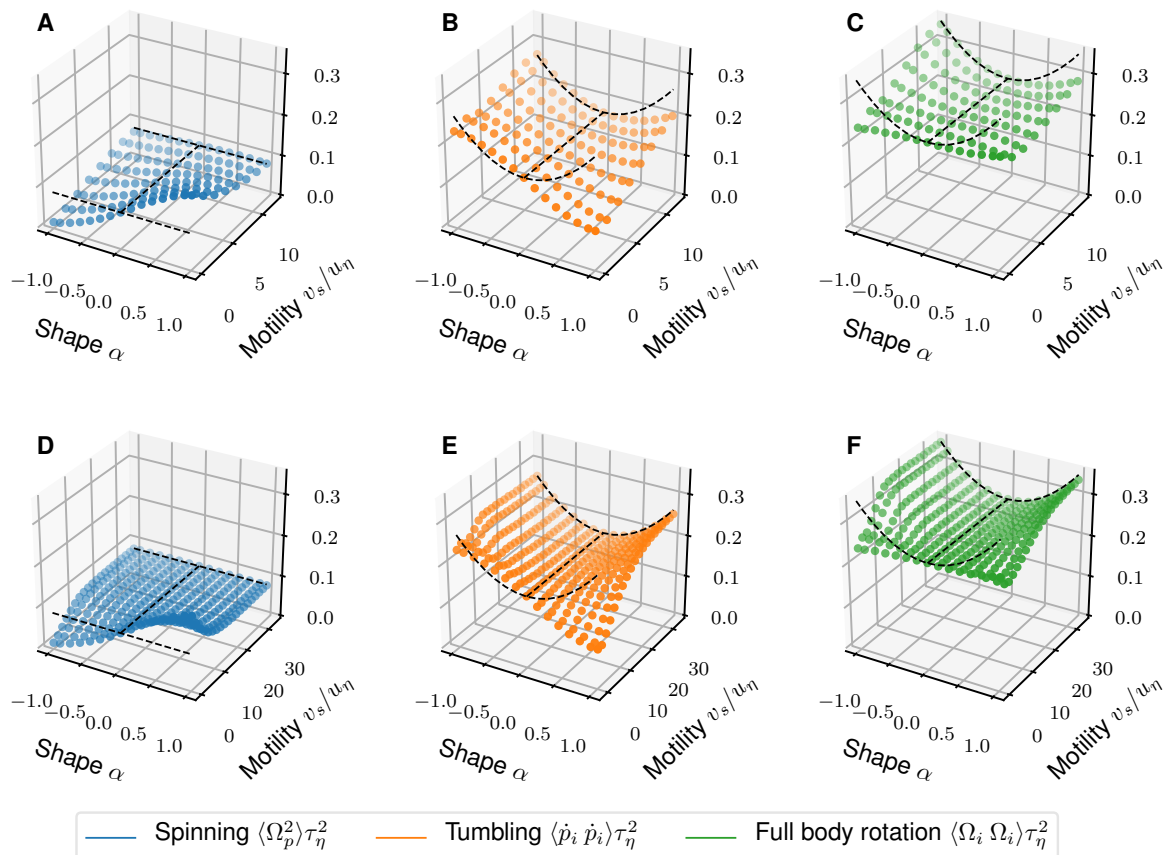


Figure 4.3: Spinning, tumbling, and full-body rotation rates of motile ellipsoids as a function of shape parameter  $\alpha$  and swimming speed  $v_s$ . **A** In the the range of swimming speeds  $0 \leq v_s/u_\eta \leq 12$  motility leads to a departure from the known passive tracer rotation rates. As the swimming speed  $v_s$  increases we observe convergence to the uncorrelated case. **B** In the motility dominated limit to rotation rates of ellipsoids converge onto the uncorrelated rotation rates. The rotation statistics hence interpolate between the non-motile passive statistics ( $v_s = 0$ ) and uncorrelated statistics ( $v_s > 20 u_\eta$ ). Equations (4.16)–(4.9) are shown in dashed black. These results were obtained by averaging over  $10^6$  particles after a  $12.6 \tau_\eta$  transient. Each point is an individual particle ensemble in a  $N = 1024^3$  simulated Navier-Stokes flow with  $R_\lambda \sim 100$ .

### 4.3 Rotation statistics

We explored above two limiting cases of shape-dependent rotation rates: the uncorrelated case and the passive tracer case. In the following we will explore the effect of motility on the rotation rates, and the interpolating effect that motility plays between these two limiting cases. Motile particles depart from the trajectories expected for passive tracers. As a consequence, the correlations between orientation and the small-scale features of the flow will differ to those of their non-motile counterparts. This has an effect on Jeffery’s equations, as the spinning (4.11) and tumbling rates (4.12) depend on the correlation between the ellipsoid orientation and the local strain and vorticity. We take non-motile particles as a starting point. These tracers have known spinning and tumbling rates (see figure 4.2 B). These rotation rates are

the product of the orientation statistics between the ellipsoids and the small-scale features of the flow, i.e. strain and vorticity. Starting from random initial conditions, these orientation statistics set in after around  $10 \tau_\eta$ . The introduction of motility leads to departures from the tracer trajectories. As a consequence, the correlation between orientation and velocity gradient gradually vanishes. In the motility-dominated limit, the correlations are so quickly destroyed that orientation and velocity gradient decorrelate. As a consequence, in this limit we observe the spinning and rotation statistics of uncorrelated orientations (see figure 4.2 **A**). Particle motility can hence be understood as a control parameter, which interpolates between passive tracer statistics in the non-motile case, and uncorrelated statistics in the high motile limit.

The transition from the tracer and the uncorrelated limits for motile ellipsoids is shown in figure 4.3. In **A** we show spinning, tumbling, and total squared rotation rates for swimming speeds in the range  $0 - 10 u_\eta$ . In **B** the spinning rates smoothly converge from the tracer non-motile limit towards the constant uncorrelated limit (4.14). Throughout, prolate ellipsoids spin more than their oblate counterparts. Conversely, oblate ellipsoids always tumble more than other shapes. Furthermore, the tumbling rate of oblate ellipsoids changes only mildly from the tracer limit to the uncorrelated case. This is in strong contrast with prolate ellipsoids, whose tumbling rate approaches the uncorrelated rate only at around  $\sim 30 u_\eta$ . Both of these effects combined lead to oblates reaching uncorrelated limit at a much lower motility than other shapes.

A notable feature here is that phase-space incompressibility motile spheres has direct consequences on rotation rates. As we saw above (section 4.2.2), spheres spin and tumble only due to contributions from vorticity. Additionally, spherical swimmers preserve total phase-space. As a consequence, the averaged spinning (4.11) and tumbling (4.12) rates of a homogeneously distributed ensemble of motile spheres equal spatial averages of the vorticity field. Hence, sphere spinning and tumbling rates are unaffected by motility and remain constant and equal to the uncorrelated spinning (4.14) and tumbling (4.15) rates. This can be seen in figures 4.2 and 4.3. For spheres ( $\alpha = 0$ ), neither motility nor the presence of an underlying turbulent flow alters rotation rates. That is, the rotation rates (4.14)–(4.16) with  $\alpha = 0$  are valid in the uncorrelated, in the passive tracer, and in the motile cases.

In this section we studied the effect of motility on rotation rates of ellipsoids in a turbulent flow. We found that the rotation rates of spheres remain unaltered by motility. For other shapes phase-space can contract or expand, leading to different correlations and orientations between ellipsoid orientation and strain and vorticity. As a consequence, oblate ellipsoids mostly only tumble, and throughout they tumble more than prolate ellipsoids.

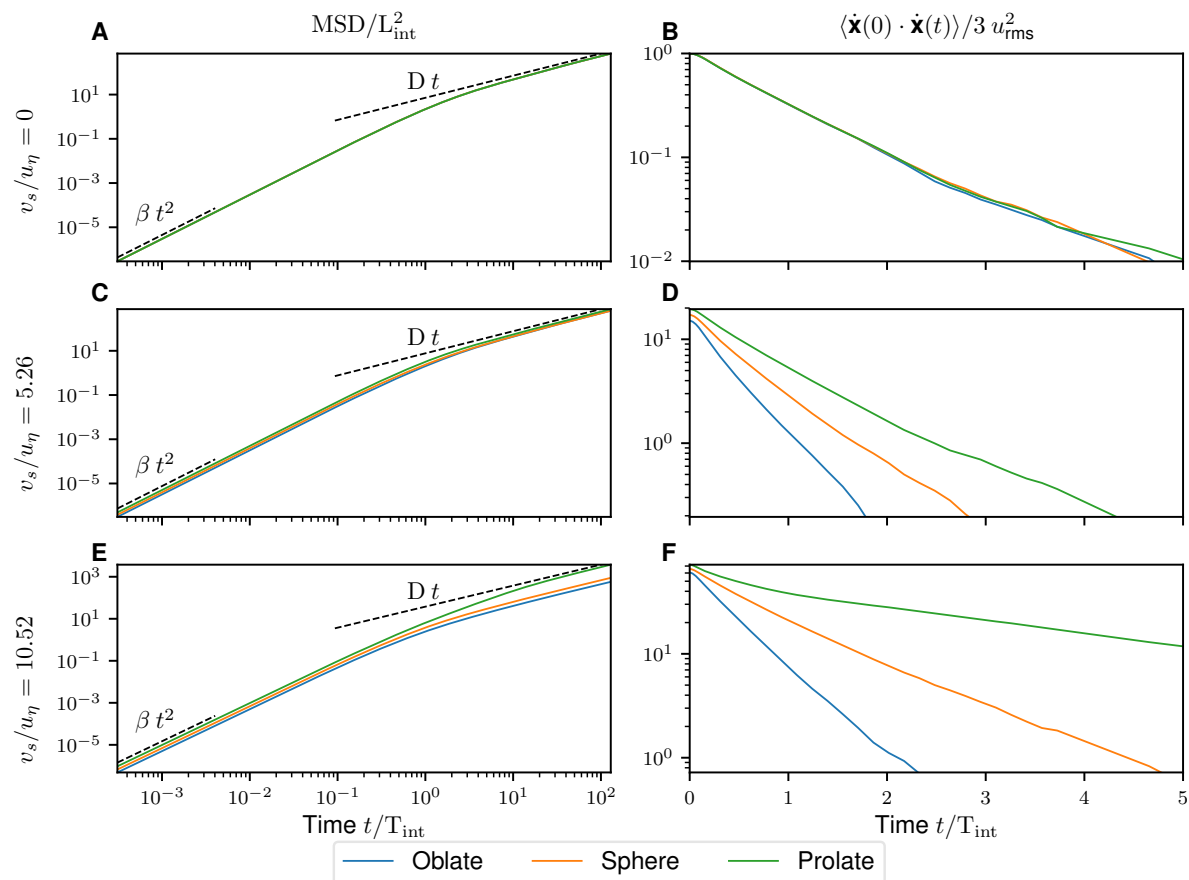


Figure 4.4: The MSD is a statistical quantity which describes how quickly particles depart from a given starting position. The proportionality constants  $\beta$  and  $D$  depend on particle shape and motility. **A,C,E** At small times the behavior is ballistic, whereas at long times it is diffusive. The effect of motility changes these constants as a function of shape. Increasing the swimming speed makes these differences more notable. **B,D,F** The correlation functions of particle velocity play a crucial role in determining the time evolution of the MSD. Prolate ellipsoids consistently show stronger and longer lasting correlation functions than other shapes. This leads to these shapes having higher transport properties than other shapes.

## 4.4 Dispersion statistics

In this section we will explore the effect of motility and shape in the dispersion properties of motile ellipsoidal swimmers in a turbulent flow. Consider a single motile particle starting from an initial position  $\mathbf{x}(0)$ . This particle has a squared displacement defined as

$$[\mathbf{x}(t) - \mathbf{x}(0)]^2. \quad (4.17)$$

This quantity measures, as a function of time, how far a given particle is displaced from its initial position. Let us now take an ensemble of particles and average their squared displacement. This ensemble quantity describes the dispersion properties of the particle ensemble in a flow. This mean squared displacement (MSD) is defined as

$$\text{MSD}(t) = \langle [\mathbf{x}(t) - \mathbf{x}(0)]^2 \rangle. \quad (4.18)$$

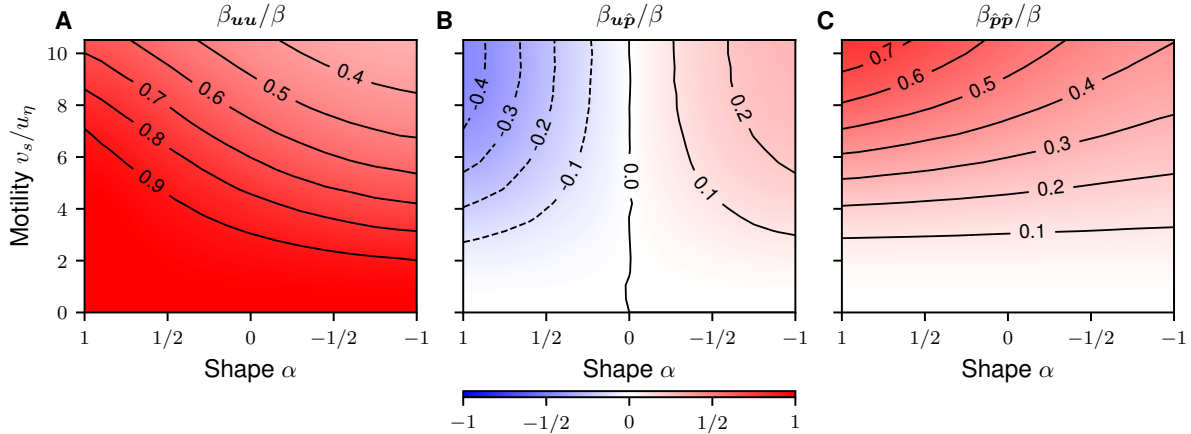


Figure 4.5: The different contributions to the ballistic constant (4.21) can be split up into **A** pure advective  $\beta_{uu}$ , **B** crossed term  $\beta_{up}$ , and **C** pure motile  $\beta_{pp}$  contributions. Here we show the relative contributions from each of these to the total ballistic constant  $\beta$  for a given motility and shape. The crossed term contributions have the greatest shape-dependent behavior, due to elongated ellipsoids aligning with the velocity field, while oblate ellipsoids tend to anti-align to the velocity field. This gives prolates a higher ballistic constant than other shapes. Summing all contributions yields the ballistic constant, as reported in figure 4.6 **A**.

In the following, we will closely look at the short- and long-time behavior of the MSD, and quantify the effect of motility and shape in the diffusive properties of particle ensembles. To this end we recast (4.18) in the form [42]

$$\text{MSD}(t) = 2t \int_0^t ds \left(1 - \frac{s}{t}\right) \langle [\dot{\mathbf{x}}(s) - \dot{\mathbf{x}}(0)]^2 \rangle. \quad (4.19)$$

The particle velocity autocorrelation function and the MSD are shown in figure 4.4. Using equation (4.19) we will explore the short and long time limits of the MSD as a function of motility and shape.

#### 4.4.1 Ballistic regime

An analysis of the MSD at small times reveals ballistic scaling. That is, taking a small time expansion of (4.19) reveals the scaling

$$\lim_{t \rightarrow 0} \text{MSD}(t) = \beta t^2, \quad (4.20)$$

This is a general mathematical property of the MSD (4.18). The specific choice of equations of motion  $\dot{\mathbf{x}}$  fixes the proportionality constant, which we call  $\beta$ . In our case, setting  $\dot{\mathbf{x}}$  to (4.3), plugging this into (4.19), and carrying out a Taylor expansion leads to three individual contributions

$$\beta = \beta_{uu} + \beta_{\hat{p}\hat{p}} + \beta_{u\hat{p}}. \quad (4.21)$$

The contributions to the ballistic constant are a pure velocity, a pure motility, and a cross term contributions. These are obtained respectively as

$$\beta_{uu} = \langle \mathbf{u}^2 \rangle, \quad \beta_{\hat{p}\hat{p}} = v_s^2, \quad \text{and} \quad \beta_{u\hat{p}} = 2 v_s \langle \mathbf{u} \cdot \hat{\mathbf{p}} \rangle. \quad (4.22)$$

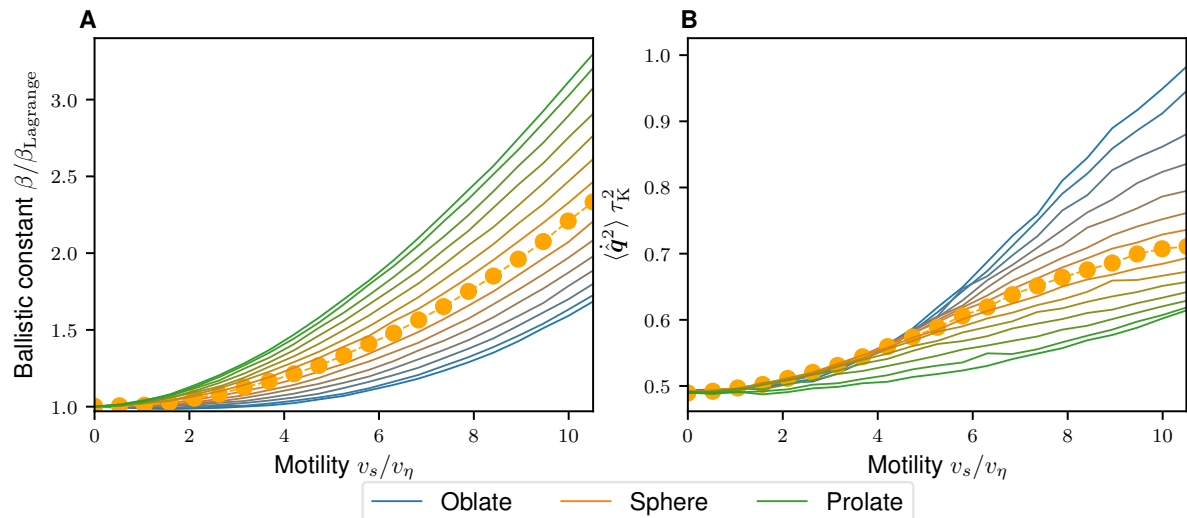


Figure 4.6: **A** The ballistic constant  $\beta$  is shown as a function of swimming velocity and shape. It is normalized by the ballistic constant of non-motile species  $\beta_{\text{Lagrange}}$ . Prolates have throughout a higher ballistic constant as other shapes. **B** The tumbling rate of the velocity vector summarizes the effect of the individual contributions (4.21) to the ballistic constant. Disks tumble more, which leads to reorientation of the velocity vector, and decreased transport. Prolates on the other hand tumble less and tend to orient with the velocity vector and maximize their transport at small times.

These individual contributions to the ballistic constant are shown in figure 4.5. Apart from shape-induced spatial inhomogeneities [23],  $\beta_{uu}$  is an instantaneous average and reflects the mean squared value of the flow velocity  $\langle \mathbf{u}^2 \rangle$ . The motility contribution  $\beta_{\hat{p}\hat{p}}$  is fixed by the particle swimming speed  $v_s^2$ . Finally, the cross term  $\beta_{u\hat{p}}$  is fixed by the shape-dependent orientational statistics. It is known that this cross term is proportional to  $\alpha$  [72], i.e. prolates align with the velocity field and disks anti-align. This observation has been made in other simulations: slender ellipsoids  $0 < \alpha \leq 1$  align with the velocity field, while oblate ellipsoids  $-1 \leq \alpha < 0$  anti-align with it [73]. Due to symmetry considerations, for the averages of spheres ( $\alpha = 0$ ) the orientation vector  $\hat{p}$  can be arbitrarily redefined. As a consequence, for spheres the quantity  $v_s \langle \mathbf{u} \cdot \hat{p} \rangle$  averages out to zero. Interestingly, the ballistic constant for spheres is the direct sum of the squared averaged flow velocity  $\langle \mathbf{u}^2 \rangle$  and motility  $v_s^2$

$$\beta_{\text{spheres}} = \langle \mathbf{u}^2 \rangle + v_s^2. \quad (4.23)$$

Therefore, spheres serve as a reference point to measure the effect of shape on the ballistic constant.

Summing up all contributions above for different shapes, we obtain a shape- and motility-dependent ballistic constant (see figure 4.6). The crossed term  $v_s \langle \mathbf{u} \cdot \hat{p} \rangle$  yields the strongest shape-dependent contribution, being negative for oblate ellipsoids, zero for spheres, and positive for prolate ellipsoids. As a consequence in the short-time limit prolate ellipsoids get an edge compared to spheres, while oblates are hindered by the negative contribution from the cross term. The shape-dependent ballistic constant have the following ordering

$$\beta_{\text{oblates}} < \beta_{\text{spheres}} < \beta_{\text{prolates}}. \quad (4.24)$$

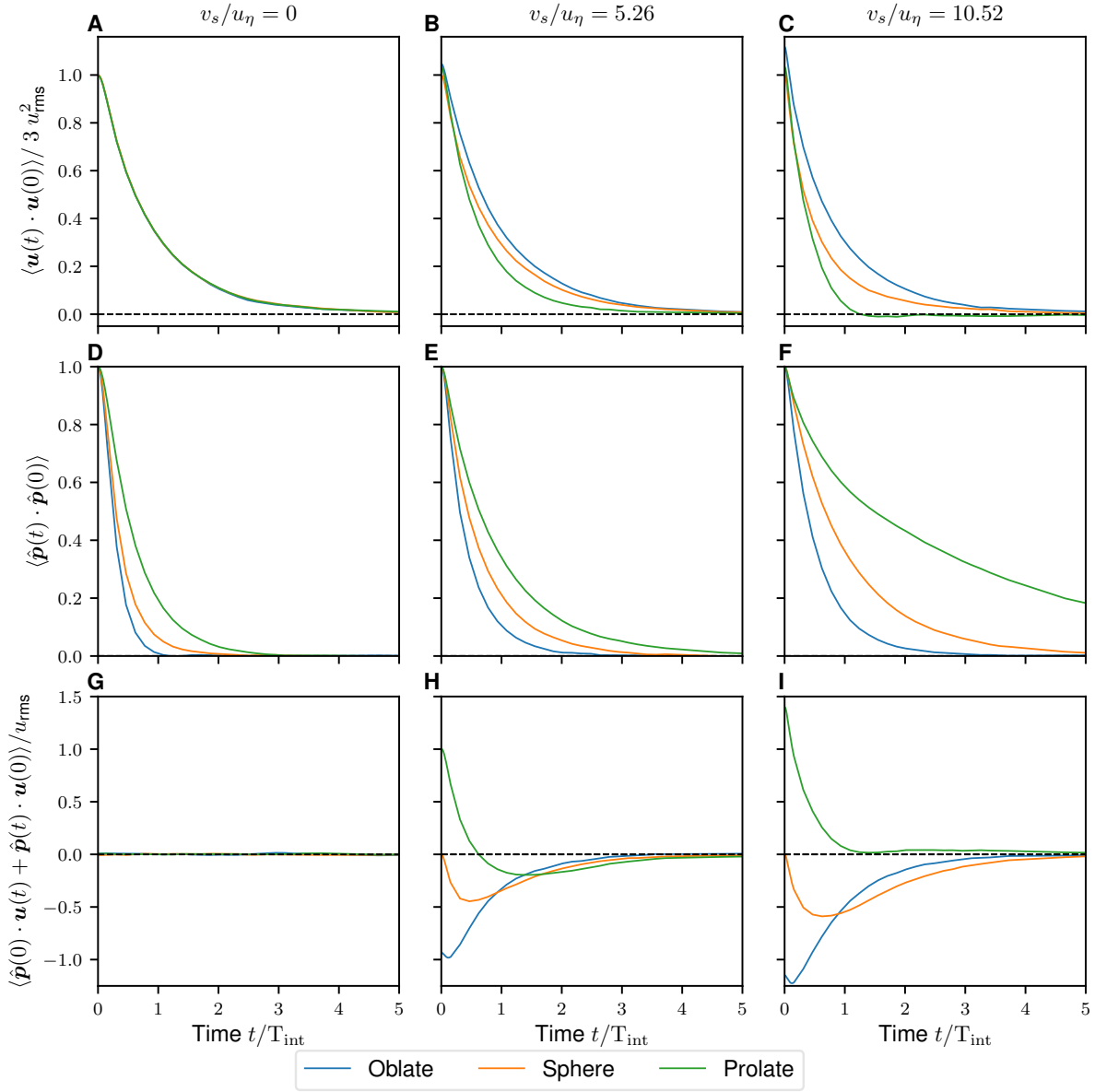


Figure 4.7: The correlation functions of **A–C** pure velocity (4.29), **D–F** pure motile (4.29), and **D–I** mixed (4.29) contributions are shown. Integrating over all these contributions leads to the full diffusive constant. Increasing motility from **A** to **C** shows that oblate ellipsoids have higher pure velocity correlation than other shapes. This is due to disks being slow in the ballistic regime, and retaining correlation at longer times, as they spatially remain longer near their point of origin, in comparison with other shapes. **D** The orientation autocorrelation function shows that for prolates, orientation remains correlated longer even in the non-motile case. The orientation of tumbling oblates, on the other hand, tends to quickly decorrelate. Adding motility **E–F** only makes these effects more dramatic, as oblates remain correlated even longer. The crossed-term correlations **G–I** have the strongest shape dependence. Oblates and spheres have negative cross-term correlation functions. Prolates cross-term correlation functions start positive, and for sufficiently low motility will have also a negative contribution.

As we saw in figure 4.4 and equation (4.19), the correlation functions play a defining role in the MSD. In the ballistic limit a way to summarize our previous results is the following. Consider the velocity vector of a particle as having an orientation  $\hat{\mathbf{q}}$  and a magnitude  $|\dot{\mathbf{x}}|$  such that

$$\dot{\mathbf{x}} = \hat{\mathbf{q}} |\dot{\mathbf{x}}| \quad (4.25)$$

A way to rationalize the results of shape-dependent ballistic diffusion is to look at the tumbling rate of the velocity vector  $\dot{\mathbf{x}}$ , that is  $\langle \dot{\mathbf{q}}^2 \rangle$ . This quantity is an instantaneous quantity relevant at the small time scales we are considering here. A large tumbling rate of the velocity vector indicates a motile ellipsoid whose velocity vector quickly changes its orientation. In contrast, a small tumbling rate indicates that the orientation of velocity changes seldom, thus having a positive effect in the particle's ballistic diffusion. We show the shape and motility dependent tumbling rate of the velocity vector in figure 4.6 B. As can be seen, oblates tumble more than other shapes, while prolates tumble less. This velocity vector tumbling rate  $\langle \dot{\mathbf{q}}^2 \rangle$  summarizes the effect of the instantaneous averages shown in figure 4.5, which lead to the observed ballistic constants reported in figure 4.6 A.

After investigating the small time behavior of the MSD contained in instantaneous averages, we will study the long time limit in the next section.

#### 4.4.2 Diffusive regime

We will now look at the long-time asymptotics. In this limit, the MSD is diffusive, that is, it scales linearly with time. We denote D the corresponding proportionality constant in this limit

$$\text{MSD}(t) \sim D t, \quad t \rightarrow \infty. \quad (4.26)$$

In the long time limit, in equation (4.19) the integrand  $(1 - s/t) \langle \dot{\mathbf{x}}(s) \cdot \dot{\mathbf{x}}(0) \rangle$  can be approximated as  $\langle \dot{\mathbf{x}}(s) \cdot \dot{\mathbf{x}}(0) \rangle$ , assuming that the correlation function decays quickly enough. As a consequence, the integrand can be rewritten in this limit to yield an expression for D as

$$D = 2 \int_0^\infty ds \langle \dot{\mathbf{x}}(s) \cdot \dot{\mathbf{x}}(0) \rangle. \quad (4.27)$$

Using this expression, the ballistic constant can be split up into three distinct contributions

$$D = D_{uu} + D_{u\hat{p}} + D_{\hat{p}\hat{p}}. \quad (4.28)$$

These contributions are due to pure advection  $D_{uu}$ , pure motility  $D_{\hat{p}\hat{p}}$ , and cross terms  $D_{u\hat{p}}$ . Plugging in the equation of motion (4.3) we can work out the individual contributions to the following expressions

$$D_{uu} = 2 \int_0^\infty ds \langle \mathbf{u}(s) \cdot \mathbf{u}(0) \rangle, \quad (4.29)$$

$$D_{u\hat{p}} = 2 v_s \int_0^\infty ds \langle \hat{\mathbf{p}}(s) \cdot \mathbf{u}(0) + \mathbf{u}(s) \cdot \hat{\mathbf{p}}(0) \rangle, \quad (4.30)$$

$$D_{\hat{p}\hat{p}} = 2 v_s^2 \int_0^\infty ds \langle \hat{\mathbf{p}}(s) \cdot \hat{\mathbf{p}}(0) \rangle. \quad (4.31)$$

These individual contributions depend solely on the integral of the respective correlation functions. Analyzing the pure velocity and pure motile correlation functions in figure 4.7 have

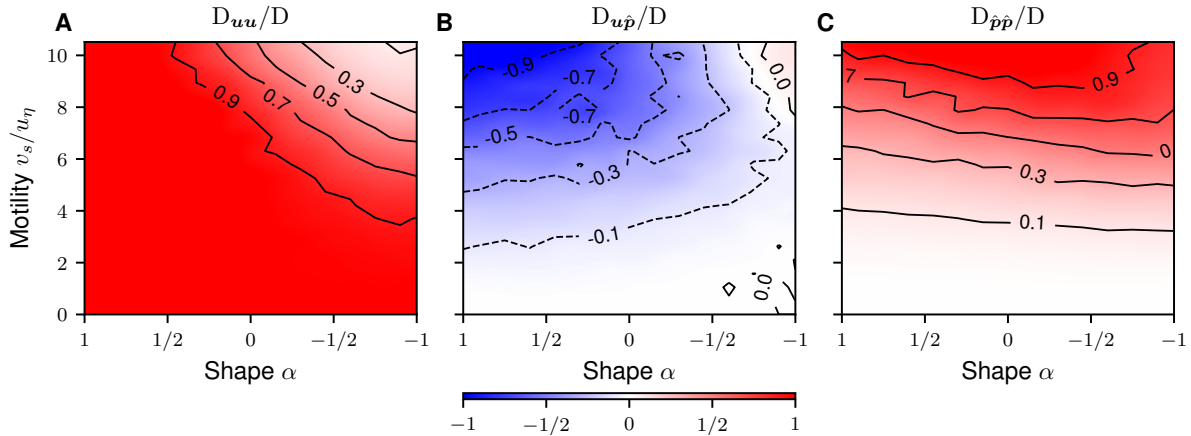


Figure 4.8: The diffusive constant can be split up in distinct contributions (4.28). Integrals over correlation functions of **A** pure velocity (4.29), **B** mixed (4.29), and **C** pure motile (4.29) contributions build up the diffusive constant. The mixed term has the most prominent shape dependence. As we observed in figure 4.7, disks and spheres have a prominent negative contribution in their crossed term correlation functions. These contributions lower a diffusive constant for disks and spheres.

comparable and positive contributions. It is notable that for the pure velocity correlation functions oblates show higher correlations than other shapes. This is due to their tumbling and reorienting. These ellipsoidal shapes remain longer bound to a local part of the flow, thus yielding longer correlations to the local velocity field. In contrast, the orientation correlation function is dominated by prolates even in the non-motile case. Further increasing motility enhances the orientation correlation. This is due to prolates mostly spinning and not tumbling. The cross term correlation functions are the ones that yield the most significant shape-dependent behavior.

Looking closely at these correlation functions (see figure 4.7), we observe that just as in the ballistic case, the cross-terms are strongly shape-dependent. The crossed correlation function at initial time corresponds to the average  $\langle \mathbf{u} \cdot \hat{\mathbf{p}} \rangle$ . In the non-motile case these correlations cancel out [72]. For motile ellipsoids, this quantity is positive for prolates, zero for spheres, and negative for oblates. The correlation function then remains negative for all times for the spherical and oblate cases. In the case of prolates, we observe that the correlation functions start positive and then undergo a cross-over to negative values. For sufficiently high motility these crossed-term correlations can even be completely positive for prolates. As a consequence, prolates have a clear transport advantage over other shapes, as they have a positive contribution to this correlation function, while all other shapes have only negative contributions.

We then integrate over the correlation functions (4.29)–(4.31) shown in figure 4.7 and sum the individual contributions to obtain the diffusion constant (4.28). We show the relative individual contributions to the total diffusion constant  $D$  in figure 4.8. As can be seen there, disks and even spheres have a considerable negative contribution from the integral of their crossed-term correlation functions. This in turn hinders their diffusive properties. Oblates, on the other hand, get mostly positive contributions.

A way to rationalize the sum of all contributions to the diffusive constant is by the total correlation time of (4.27). This is nothing more than the correlation time of the velocity vector  $\hat{\mathbf{x}}$ .

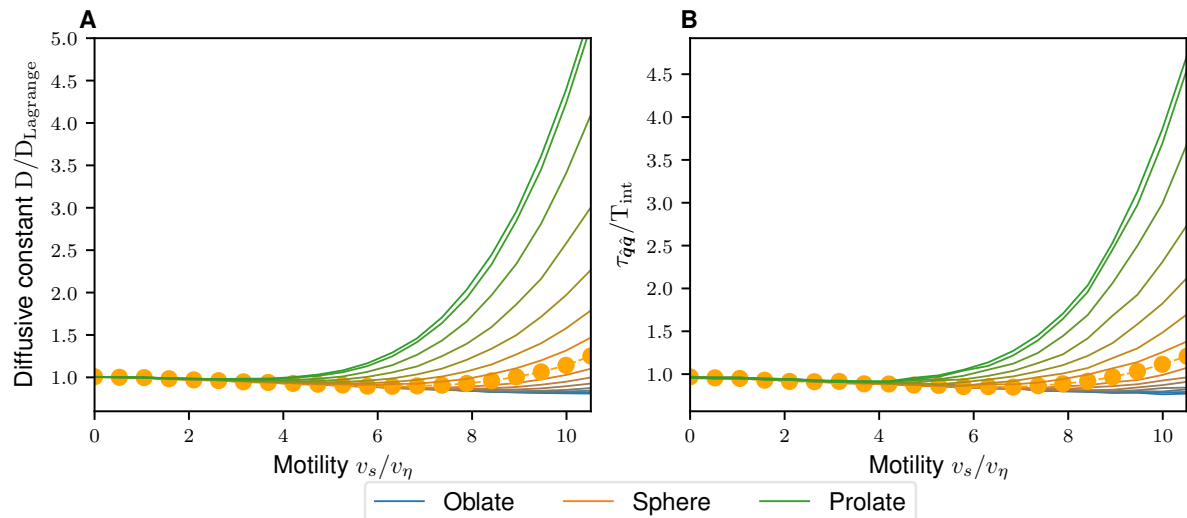


Figure 4.9: **A** Beyond a certain swimming speed prolates quickly depart from other shapes and show a much larger diffusive constant. This is a consequence of the correlation functions studied in figure 4.7. **B** The auto-correlation time  $\tau_{\hat{q}\hat{q}}$  of the velocity vector orientation  $\hat{q}$  summarizes our results here. A long  $\tau_{\hat{q}\hat{q}}$  implies an ellipsoid that retains its orientation longer and can hence diffuse quicker in time. Oblates tumble more than other shapes. Tumbling reorients the ellipsoid and hinders transport. Prolate ellipsoids tend to spin and remain oriented in the same direction for longer, which leads to higher diffusion.

In figure 4.9 **B** we show the total correlation time as a function of shape and motility. It can be seen that the diffusive constant is a measure of the shape and motility dependent correlation time. A longer correlation time means that the velocity vector  $\hat{x}$  keeps its direction constant for a longer time. As a consequence the swimmer disperses more. As we saw above, prolate ellipsoids have an advantage in this. Due to their cross correlation function having positive contributions, prolate shaped swimmers move along with the velocity field, maximizing the possible traversed distance. Oblate ellipsoids, on the other hand, tend to anti-align, counteracting the advective and motile contributions.

In this section we studied the spatial dispersion properties of motile ellipsoidal swimmers. Due to alignment properties of prolate ellipsoids with the velocity field, these shapes disperse faster both in the short and the long time limits of the MSD. Oblate ellipsoids, on the other hand, tumble intensely, hindering dispersion. Higher tumbling rates lead to shorter velocity vector correlation times, by constantly reorienting oblate ellipsoids. In summary, due to rotation rates and orientation properties, prolate ellipsoids more efficient diffusion properties in a turbulent flow over spheres and oblate ellipsoids.

## 4.5 Collision rates

In this section we will investigate the collision rates of motile ellipsoids. We carried out measurements of collision rates for flat oblate ellipsoids, spheres, and thin slender ellipsoids in turbulence. For each of these shapes we also scanned motility.

In figure 4.10 we show the collision kernel of the different shapes as a function of motility. After a turbulence-dominated regime, motility quickly takes over the collision rates, and a

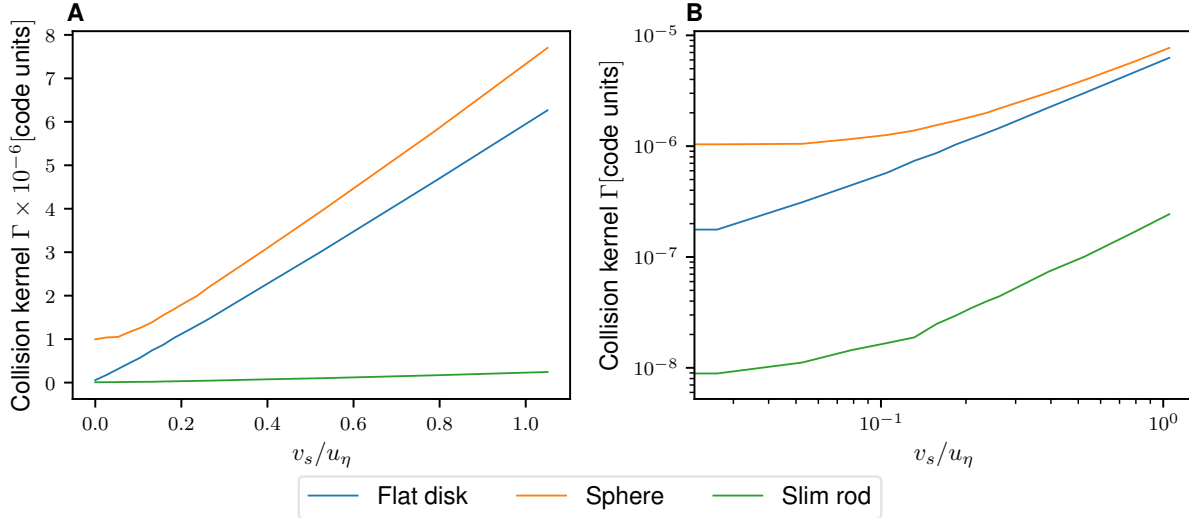


Figure 4.10: Collision rates of flat disks, spheres, and slim rods. **A** In the non-motile limit collisions are induced by turbulent advection. In the motility dominated regime linear scaling is observed. **B** The transition to the linear regime happens at a very low swimming speed. Here we show flat disks of diameter  $0.48\eta$  and aspect ratio  $\lambda = 0.05$ , spheres of diameter  $0.48\eta$ , and thin rods of length  $0.48\eta$  and aspect ratio  $\lambda = 20$ .

linear regime is observed. Due to time constraints at the time of writing of this dissertation and the technical difficulty of handling non-spherical shapes, we will concentrate on the case of spheres. We will now present theoretical predictions on the collision rates of spheres and explain the numerical results obtained in the simulations.

#### 4.5.1 Collision kernel for self-motile spheres

Consider motile spheres of diameter  $l$ . Following [56], to calculate the collision kernel we construct the particle flux of colliding particle pairs. We calculate the integral

$$\Gamma_{\text{spheres}}^{\text{motile}} = \frac{1}{2} \int_{S^2(l)} dS \langle |w_r| \rangle, \quad (4.32)$$

where  $w_r$  is the component of the relative velocity normal to the integration surface  $w_r = v_s \hat{\mathbf{e}}_r \cdot (\hat{\mathbf{p}}_1 - \hat{\mathbf{p}}_2)$ . This is a surface integral over the sphere of the velocity vector normal to the sphere. We choose the coordinate system so that the first of the colliding particles is aligned with the  $z$ -axis  $\hat{\mathbf{p}}_1 = \hat{\mathbf{e}}_z$ . With this choice of coordinate system we then average over the direction of the second colliding particle  $\hat{\mathbf{p}}_2$ . The integral in (4.32) then yields

$$l^2 \frac{v_s}{2} \int_0^{2\pi} d\phi \int_0^\pi d\theta \sin \theta \langle |\cos \theta - \hat{\mathbf{e}}_r \cdot \hat{\mathbf{p}}_2| \rangle_{\hat{\mathbf{p}}_2} \quad (4.33)$$

The average over  $\hat{\mathbf{p}}_2$  takes the form

$$\langle |\cos \theta - \hat{\mathbf{e}}_r \cdot \hat{\mathbf{p}}_2| \rangle_{\hat{\mathbf{p}}_2} = \frac{1}{4\pi} \int_{S^2} d\hat{\mathbf{p}}_2 |\cos \theta - \hat{\mathbf{e}}_r \cdot \hat{\mathbf{p}}_2|. \quad (4.34)$$

In this integral  $\cos \theta$  is a constant, which we denote as  $\cos \theta = a$ . Additionally, we choose the

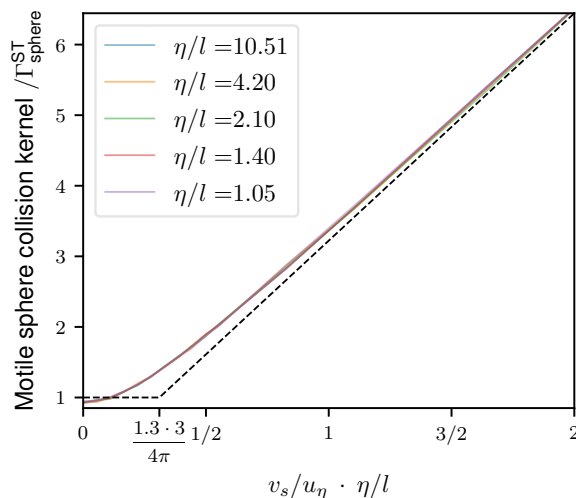


Figure 4.11: The collision kernel for motile spheres of different radii can be collapsed onto a master curve. The transition from the turbulent to the motile dominated collision kernel happens at a very low swimming speed 4.39.

coordinate system for the  $\hat{\boldsymbol{p}}_2$  integration such that the polar angle  $\beta$  fulfills  $\hat{\boldsymbol{e}}_r \cdot \hat{\boldsymbol{p}}_2 = \cos \beta$ . We can then solve the integral as

$$\frac{1}{4\pi} \int_0^{2\pi} d\alpha \int_0^\pi d\beta \sin \beta |a - \cos \beta| \stackrel{x = -\cos \beta}{=} \frac{1}{2} \int_{-1}^1 dx |a + x| = \frac{1 + a^2}{2} \quad (4.35)$$

We insert the result (4.35) into (4.33) and obtain

$$\frac{l^2}{4} v_s \int_0^{2\pi} d\phi \int_0^\pi d\theta \sin \theta (1 + \cos^2 \theta) \stackrel{x = -\cos \theta}{=} \pi \frac{l^2}{2} v_s \int_{-1}^1 dx (1 + x^2) = \frac{4\pi}{3} l^2 v_s. \quad (4.36)$$

The collision kernel of motile spheres then reads

$$\Gamma_{\text{spheres}}^{\text{motile}} = \frac{1}{2} \int_{S^2(l)} dS \langle |w_r| \rangle = \frac{4\pi}{3} l^2 v_s. \quad (4.37)$$

This expression describes the collision kernel of spheres in the motile limit, and is a velocity mono-disperse version of the collision kernel in an ideal gas [107]. On the other hand, passive tracer spheres have a collision kernel approximated by the so called Saffman-Turner kernel [56]

$$\Gamma_{\text{sphere}}^{\text{ST}}(l) = 1.3 l^3 \sqrt{\varepsilon / \nu}. \quad (4.38)$$

A transition speed between these two limiting cases can be obtained by equating (4.37) and (4.38). We then obtain a transition swimming speed as

$$\frac{v_s}{u_\eta} = \frac{3 \cdot 1.3}{4\pi} \frac{l}{\eta} \sim 0.3 \frac{l}{\eta}. \quad (4.39)$$

From this result we can learn the following. Firstly, the quantity  $v_s \eta / u_\eta l$  is the control parameter for the sphere collision kernel. Secondly, for a fixed Kolmogorov length and sphere diameter, the effect of motility overcomes advection already for motility smaller than the Kolmogorov speed of the flow. In figure 4.11 we show the collision kernel for different particle lengths. As can be seen, we obtain a master curve depending on the control parameter. The motile dominated linear regime quickly dominates over the turbulent limit.

## 4.6 Discussion

In this chapter we have explored the effect of motility and shape on rotation rates, dispersion statistics, and collision rates of ellipsoids in turbulence.

We observed that motility induces a transition from two limiting cases of rotation rates. In the non-motile limit tracer statistics are observed, while in the high-motility limit uncorrelated statistics are reproduced. Due to phase-space conservation, spheres have constant rotation rates throughout. Oblate ellipsoids, on the other hand, mostly tumble, and throughout tumble more than prolate ellipsoids. The high tumbling rate of oblates turned out to be crucial in their dispersion statistics. The high tumbling rate induces a constant change of the direction of the velocity vector. As a consequence, these shapes have a reduced dispersion compared to other shapes. Additionally, due to the orientation dynamics prolate ellipsoids align with the velocity field. Advection then constructively acts with motility to enhance particle travel. Conversely, oblate ellipsoids anti-align with the velocity field, and in this case advection and motility act against one another. Both the tumbling rates and orientation statistics lead to ellipsoidal swimmers having enhanced dispersion statistics when compared to other shapes. These effects are shape dependent, and compared to passive tracers, the effect of motility sets in at motility comparable several-fold of the Kolmogorov speed of the flow.

When measuring collision rates of motile particles in turbulence we found that two limiting cases can be identified. Firstly, turbulence dominated case in the non-motile limit. In this limit results exist which depend on the particle size and Kolmogorov speed of the flow. In the motile limit, the collision kernel is linear in the swimming speed. We found that small swimming velocities suffice to dominate the collision generation mechanism.

---

Part III

Manuscript II

---

# Elongation enhances encounter rates between phytoplankton in turbulence

In this chapter we present a manuscript which originally appeared as "[Arguedas-Leiva, J.-A., Słomka, J., Lalescu, C.C., Stocker, R. and Wilczek, M. \(2022\). Elongation enhances encounter rates between phytoplankton in turbulence. \*Proceedings of the National Academy of Sciences of the United States of America\*, 119 \(32\)](#)" and is licensed under the [Creative Commons Attribution-Non Commercial-No Derivatives License 4.0 \(CC BY-NC-ND\)](#).

J. S., R. S. and M. W. designed research. J.-A. A.-L. performed numerical simulations with support from C.C.L.; J.-A. A.-L., J. S. and M. W. analyzed the simulation results. J. S. led the theoretical modeling. J. S. and R. S. studied the ecological consequences. J.-A. A.-L., J. S., R. S. and M. W. wrote the paper.

J.-A.A.-L. and J.S. contributed equally to this work.

# Elongation enhances encounter rates between phytoplankton in turbulence

José-Agustín Arguedas-Leiva,<sup>1</sup> Jonasz Słomka,<sup>2\*</sup>  
Cristian C. Lalescu,<sup>3</sup> Roman Stocker,<sup>2</sup> Michael Wilczek<sup>1,4†</sup>

<sup>1</sup>Max Planck Institute for Dynamics and Self-Organization (MPI DS), Göttingen, Germany

<sup>2</sup>Institute for Environmental Engineering, Department of Civil, Environmental and Geomatic Engineering, ETH Zurich, Zurich, Switzerland

<sup>3</sup>Max Planck Computing and Data Facility, Garching, Germany

<sup>4</sup>Theoretical Physics I, University of Bayreuth, Bayreuth, Germany

†To whom correspondence should be addressed; E-mail: michael.wilczek@uni-bayreuth.de .

## Abstract

Phytoplankton come in a stunning variety of shapes but elongated morphologies dominate – typically 50% of species have aspect ratio above 5, and bloom-forming species often form chains whose aspect ratios can exceed 100. How elongation affects encounter rates between phytoplankton in turbulence has remained unknown, yet encounters control the formation of marine snow in the ocean. Here, we present simulations of encounters among elongated phytoplankton in turbulence, showing that encounters between neutrally buoyant elongated cells are up to ten-fold higher than for spherical cells and even higher when cells sink. Consequently, we predict that elongation can significantly speed up the formation of marine snow as compared to spherical cells. This unexpectedly large effect of morphology in driving encounter rates among plankton provides a potential mechanistic explanation for the rapid clearance of many phytoplankton blooms.

**One-Sentence Summary:** Using simulations and modeling of ocean turbulence, we predict that elongated plankton shows unexpectedly high encounter rates.

Microscopic photosynthetic marine phytoplankton cells are responsible for nearly half of the global carbon fixation [3], a key biogeochemical process that fuels ocean primary production [108]. While phytoplankton come in a variety of shapes [109], combined data from different aquatic habitats indicate that elongated morphologies dominate, with 50% of cells having aspect ratio greater than 5 [110]. The aspect ratio of the most elongated unicellular phytoplankton (e.g., *Ulnaria*, *Rhizosolenia*) approaches 100 [109], whereas bloom-forming species, such as *Trichodesmium*, often form chains of cells which can have even higher aspect ratios [111, 112]. Cell shape is recognized as a key trait determining the fitness of phytoplankton [109], because it affects nutrient uptake [14], growth rate [113], survival upon grazing by

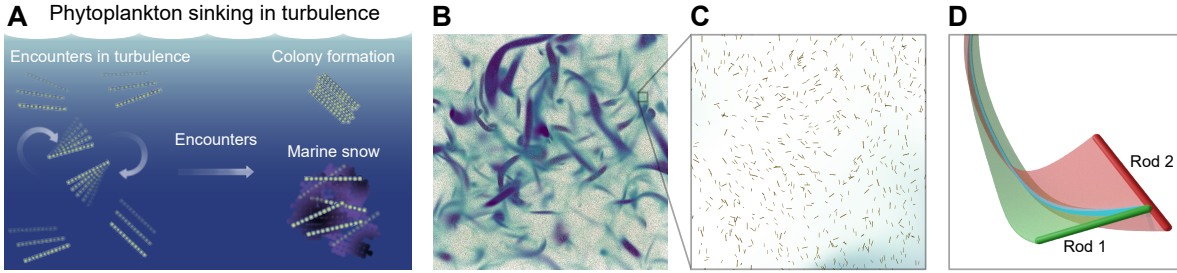


Figure 5.1: **A** Encounters between phytoplankton, whose cells or chains of cells are often highly elongated, drive key ecological processes in the ocean, such as marine snow aggregation and likely colony formation. **B,C** As a model for this process, we here present results from direct numerical simulations of millions of identical rods encountering each other due to the combined effects of turbulence and sinking. The volume rendering shows intense vorticity structures visualizing locally swirling regions in the flow. **D** Trajectories of two encountering rods. Green and red shadings visualize the swept areas, blue indicates the rods' overlap used to detect encounters.

zooplankton [114], swimming direction [71] and light harvesting [115]. By contrast, the impact of elongation on encounters between individual phytoplankton has only recently started to be explored [116, 117], and we still lack an understanding of how interaction between environmental determinants, such as turbulence [14, 26, 118], and biological determinants, such as cell size, elongation and density [14, 26, 117, 118], control encounters. Yet, encounters between individual phytoplankton exert a fundamental control on a broad range of processes in plankton ecology and ocean biogeochemistry. Encounters determine the formation of marine snow, which fuels the ‘biological pump’, the vertical export of carbon to the deep ocean that represents one of the climatically most important carbon fluxes in the ocean [118–121]. Encounters may also influence the composition of marine snow particles [122], by overrepresenting species that encounter frequently, as well as the rate of phytoplankton colony formation, such as the formation of mats or tufts and puffs by the highly elongated *Rhizosolenia* [123] or *Trichodesmium* [124], important players in the nitrogen and carbon cycles [125] (Fig. 5.1A).

Here, we present results from direct numerical simulations and scaling arguments to quantify encounter rates between thin elongated cells or chains of cells, accounting for the effects of turbulence and sinking (Fig. 5.1), focusing on the parameter regime characteristic of elongated phytoplankton experiencing turbulence levels typical of the ocean surface layer. We find that, for neutrally buoyant cells, elongation enhances encounter rates by 20% for cells of aspect ratio 5, two-fold for aspect ratio 20, seven-fold for aspect ratio 100, and ten-fold for even higher aspect ratios. If cells sink or rise, such as most cells upon a bloom demise or cells that actively regulate buoyancy using gas vacuoles and carbohydrate ballasting [126, 127], respectively, we find that the combined effect of turbulence and sinking further enhances encounter rates. Based on these results, we predict that elongation can significantly accelerate the formation of marine snow as compared to spherical cells. These findings provide a potential mechanistic explanation for the rapid clearance of blooms, for the frequent occurrence of highly elongated species in marine snow particles and for the propensity of elongated species to form colonies.

To quantify the role of elongation on the encounter rates between phytoplankton cells, we conducted an extensive series of numerical simulations of millions of cells, across different environmental and cellular parameters (Fig. 5.1B, C, SI). From the simulations, we quantified

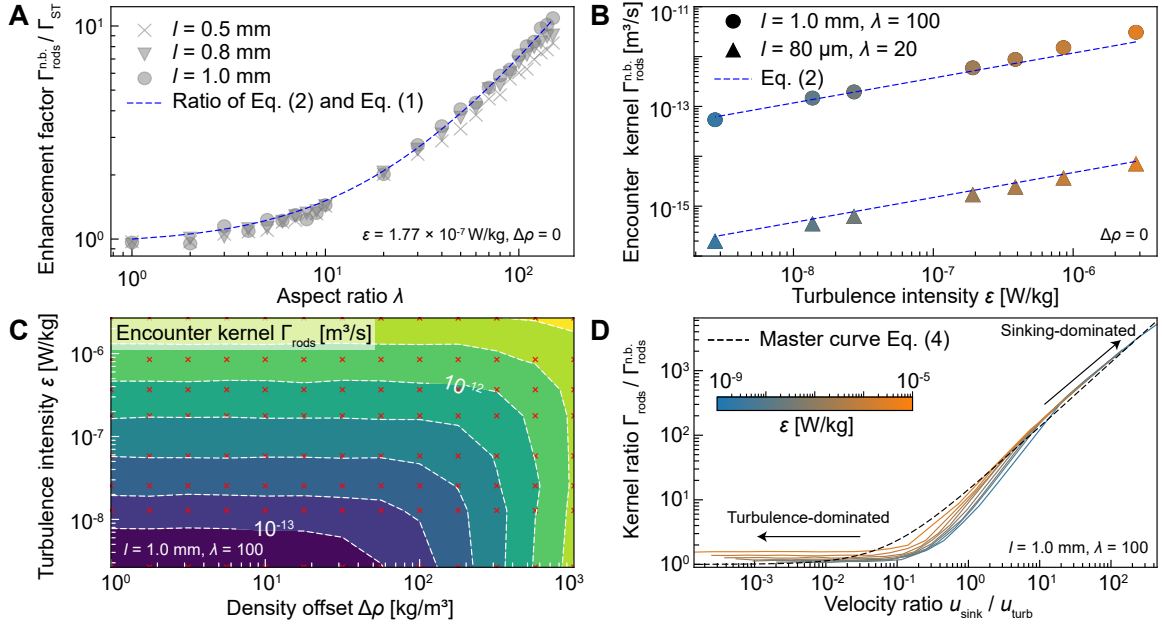


Figure 5.2: Cell elongation enhances encounter rates between cells in turbulence. **A** Encounter kernel for elongated, neutrally buoyant ( $\Delta\rho = 0$ ) cells, obtained from numerical simulations (symbols), as a function of their aspect ratio  $\lambda$ , for three different cell lengths  $l$  and a given turbulence intensity  $\varepsilon$ , showing that elongation enhances encounter rates by up to an order of magnitude. For each aspect ratio, the kernel is normalized by the kernel for equal-volume spheres [Eq. (5.1)]. The blue dashed line represents the ratio  $\Gamma_{\text{rods}}^{\text{n.b.}} / \Gamma_{\text{ST}}$  obtained by dividing Eq. (5.2) by Eq. (5.1) (SI). **B** Encounter kernel for two different elongated, neutrally buoyant phytoplankton cells as a function of turbulence intensity, computed from numerical simulations (symbols). Note the good agreement with the power-law with exponent of  $\frac{1}{2}$  predicted by Eq. (5.2) (dashed line) and by dimensional analysis (SI). **C** Encounter kernel  $\Gamma_{\text{rods}}$  of elongated ( $l = 1$  mm,  $\lambda = 100$ ), sinking rods as a function of their density offset with surrounding water and of turbulence intensity. Red crosses denote data points from numerical simulations, used to obtain the contours and colormap by interpolation. **D** Master curve of the encounter rate of elongated phytoplankton. When rescaled by the encounter kernel for neutrally buoyant rods [Eq. (5.2)], the simulated encounter kernels for buoyant rods (red crosses in **C** and additional data for heavier cells, Fig. 5.4) collapse onto a single master curve [Eq. (5.4), see text], for all values of density offset and turbulent intensity. The master curve shows a clear transition between a turbulence-dominated and a sinking-dominated regime.

encounter rates by counting geometrical intersections between cells, which we modeled as rods (Fig. 5.1D, SI). To understand the dependency of the encounter rate on environmental and cellular parameters, we computed the encounter rate kernel  $\Gamma$ .  $\Gamma$  represents the volume that a pair of encountering cells sweep relative to each other per unit time and is a key quantity widely used to characterize encounter rates in both physics and ecology [14, 56, 128].

Focusing first on neutrally buoyant cells, we found that elongated cells encounter each other up to ten-fold more frequently than equal-volume spherical cells irrespectively of the cell length or intensity of turbulence (Fig. 5.2A and B). From our simulations, we computed the encounter kernel  $\Gamma_{\text{rods}}^{\text{n.b.}}$  for elongated, neutrally buoyant cells (length  $l$ , aspect ratio  $\lambda$ ), and

compared it with the classic encounter kernel  $\Gamma_{\text{ST}}$  for neutrally buoyant spheres due to Saffman and Turner [56],

$$\Gamma_{\text{ST}} = 1.3 (2r)^3 \sqrt{\varepsilon/\nu}, \quad (5.1)$$

where  $\nu$  is the fluid’s kinematic viscosity,  $\varepsilon$  is the energy dissipation rate characterizing the turbulence intensity, and  $r$  is the radius of the spheres, which we set to match the spheres’ volumes with that of elongated cells. Computing the ratio  $\Gamma_{\text{rods}}^{\text{n.b.}}/\Gamma_{\text{ST}}$  for different cell lengths and aspect ratios revealed that elongation always enhanced encounter rates, up to ten-fold for the most elongated cells (Fig. 5.2A). This enhancement was to a good approximation independent of the cell length, which prompted us to generalize the Saffman and Turner kernel to elongated cells (‘rods’) by including the dependence on aspect ratio through a multiplicative factor  $C(\lambda)$ , as

$$\begin{aligned} \Gamma_{\text{rods}}^{\text{n.b.}} &= 1.3 l^3 \sqrt{\varepsilon/\nu} C(\lambda), \quad \text{with} \\ C(\lambda) &= -0.472\lambda^{-3} + 1.388\lambda^{-2} + 0.0841\lambda^{-1} + 9.13 \times 10^{-5}. \end{aligned} \quad (5.2)$$

$C(\lambda)$  is a function of the cell’s aspect ratio only, obtained by a fit to the simulation results (for  $l = 1$  mm) and requiring that  $C(1) = 1$  (Fig. 5.2A, SI). Thus, Eq. (5.2) generalizes the classic Saffman-Turner kernel to elongated cells ( $\lambda > 1$ ) and reduces to Eq. (5.1) for spheres ( $\lambda = 1$ ), as expected. To confirm the functional form of the new kernel  $\Gamma_{\text{rods}}^{\text{n.b.}}$ , which can be motivated by scaling arguments (SI), we considered two representative elongated cells ( $l = 1$  mm,  $\lambda = 100$  and  $l = 80$   $\mu\text{m}$ ,  $\lambda = 20$ ), varied the turbulence intensity in the simulations and found good agreement between the resulting kernel and that predicted by Eq. (5.2) (Fig. 5.2B).

For neutrally buoyant phytoplankton, we predict from Eq. (5.2) that elongation increases the encounter rate by 20% for cells of aspect ratio 5, such as cells of the genera *Navicula* or *Leptocylindrus* [109], two-fold for aspect ratio 20, such as *Rhizosolenia*, *Nitzschia* [109] or chains of *Skeletonema* [129, 130], seven-fold for cells of aspect ratio 100, such as the most elongated cells of *Rhizosolenia*, *Ulnaria* [109], and ten-fold for the most elongated chains of *Trichodesmium* with aspect ratios above 100 [111, 112] (Fig. 5.2A). With this understanding of how elongation affects encounters of neutrally buoyant cells in turbulence, we next studied the encounters of elongated cells that sink in turbulence.

Cells in turbulence that also sink or rise (‘buoyant cells’) encounter each other even more frequently than neutrally buoyant cells. Since many phytoplankton species are denser than seawater and sink, for example following a bloom [129], or can actively modulate their buoyancy [126], we considered cells with a density offset  $\Delta\rho$  compared to the ambient water. For elongated cells, a density offset induces sinking with orientation-dependent velocity (SI). Focusing on highly elongated cells ( $\lambda = 100$ ), we performed simulations to quantify their encounter kernel  $\Gamma_{\text{rods}}$  for a broad range of environmentally relevant values of their density offset and the turbulence intensity (Fig. 5.2C). The simulations revealed two distinct regimes: a turbulence-dominated regime for small values of  $\Delta\rho$  and large values of  $\varepsilon$  (horizontal contours in Fig. 5.2C), in which sinking has a negligible impact on  $\Gamma_{\text{rods}}$ ; and a sinking-dominated regime for large  $\Delta\rho$  and small values of  $\varepsilon$  (vertical contours in Fig. 5.2C), in which sinking starts to dominate over turbulence, eventually increasing the encounter rates in proportion to the density offset.

The self-similar shape of the contour lines in Fig. 5.2C results from a universal scaling for the dependence of  $\Gamma_{\text{rods}}$  on density offset and turbulence intensity. We hypothesized that the general encounter kernel is the sum of the two kernels representing the limits of neutrally

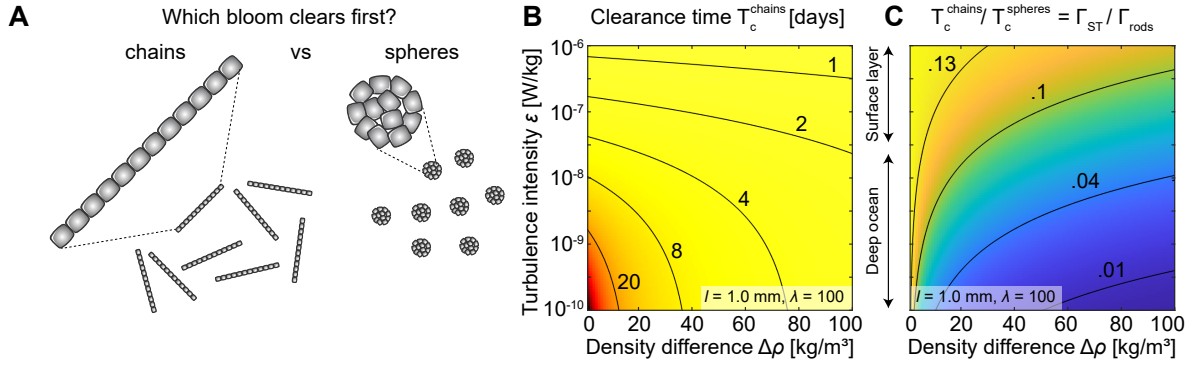


Figure 5.3: Elongation of many phytoplankton cells or chains of cells accelerates bloom clearance through marine snow formation. **A** Which monospecific bloom clears first: one formed by chains of cells or by spheres of cells? **B** Predicted bloom clearance time  $T_c$  for highly elongated chains (e.g., *Trichodesmium*) for a broad range of ecologically relevant turbulence intensities and density offsets (chain concentration  $C_0 = 10 \text{ mL}^{-1}$ ). **C** The ratio of the clearance time for chains and spheres (of equal volume) shows that marine snow forms at least seven-fold faster from chains than from spherical cells.

buoyant cells in turbulence and of cells sinking in a quiescent fluid, i.e.,

$$\Gamma_{\text{rods}} = \Gamma_{\text{rods}}^{\text{n.b.}} + \Gamma_{\text{rods}}^{\text{quiescent}}, \quad (5.3)$$

where  $\Gamma_{\text{rods}}^{\text{n.b.}}$  is given by Eq. (5.2) and, from previous work,  $\Gamma_{\text{rods}}^{\text{quiescent}} = l\beta_1\Delta\rho V_{\text{rod}}g/(16\lambda\mu)$ , where  $V_{\text{rod}}$  is the cells' volume,  $\mu$  is the fluid's dynamic viscosity,  $g$  is the gravitational acceleration and  $\beta_1(\lambda)$  is a geometrical parameter [117]. The ansatz in Eq. (5.3) then yields

$$\Gamma_{\text{rods}}/\Gamma_{\text{rods}}^{\text{n.b.}} = 1 + \Lambda(\lambda)u_{\text{sink}}/u_{\text{turb}} \quad (5.4)$$

where  $\Lambda(\lambda) = \pi/[2.6\lambda C(\lambda)]$  is a geometrical factor that depends only on the aspect ratio, and  $u_{\text{sink}} = \Delta\rho V_{\text{rod}}g\beta_1(\lambda)/(8\pi\mu l)$  and  $u_{\text{turb}} = l\sqrt{\epsilon/\nu}$  are the typical relative velocities between two cells sinking in a quiescent fluid or advected by turbulence, respectively. Rescaling the encounter kernel from our simulations (red crosses in Fig. 5.2C and additional data for heavier cells, Fig. 5.4) by the neutrally buoyant kernel  $\Gamma_{\text{rods}}^{\text{n.b.}}$  [Eq. (5.2)] and plotting it against the velocity ratio  $u_{\text{sink}}/u_{\text{turb}}$  leads to a collapse of the data (Fig. 5.2D), in good agreement with the master curve in Eq. (5.4) predicted by our hypothesis.

Equations (5.2) and (5.3) comprehensively quantify, for the first time, the encounter rate of elongated plankton in turbulence. Previous work on nonspherical objects in turbulence focused for example on preferential accumulations of elongated phytoplankton in turbulence [26], but did not address the role of elongation on encounters. Similarly, recent computations of collisions of ice crystal in clouds [55, 102] do not apply to the often highly elongated phytoplankton, because they focused on spheroids with small aspect ratios and because ice crystals are subject to inertial effects, which are not accessible to phytoplankton cells (characterized by fast relaxation timescales [26]). We found that, for environmentally realistic conditions, encounter rates of elongated cells in turbulence are often substantially higher than those of spherical cells of equal volume (for comparison with cylinders in simple shear flow [131] see SI). Because encounter rates are a foundation of many ecological processes [14], this finding has direct implications in how we understand and model these processes, as we demonstrate next

by focusing on bloom clearance, marine snow formation and colony formation by elongated phytoplankton.

The enhanced encounter rates of elongated cells may be important in bloom clearance and the associated formation of marine snow (Fig. 5.3). To investigate this process, we used our results to directly quantify the role of elongation in marine snow formation. We considered a monospecific bloom of identical elongated phytoplankton, for example cell chains that reach a high chain concentration  $C_0$  and, after dying, start sinking and stick to each other upon encounter, forming marine snow. We quantified the timescale of bloom clearance, associated with the conversion of biomass into marine snow, by computing a characteristic clearance timescale,  $T_c$ , as the time over which encounters convert half of the suspended chains into particles composed of two or more chains. We contrast the clearance time for identical chains with a hypothetical spherical cell arrangement with the same number of cells per particle (Fig. 5.3A, for alternative characterization using critical concentrations [129] see SI). The clearance time  $T_c$  is obtained by solving a simplified version of the Smoluchowski equation (SI)

$$T_c = (C_0\Gamma)^{-1}, \quad (5.5)$$

where  $\Gamma$  is the relevant encounter kernel. For example, for neutrally buoyant chains and spheres, from Eqs.(5.1) and (5.2) we have  $T_c^{\text{chains}} = (C_0\Gamma_{\text{rods}}^{\text{n.b.}})^{-1}$  and  $T_c^{\text{spheres}} = (C_0\Gamma_{\text{ST}})^{-1}$ . The clearance time ratio  $T_c^{\text{chains}}/T_c^{\text{spheres}} = \Gamma_{\text{ST}}/\Gamma_{\text{rods}}^{\text{n.b.}}$  is proportional to the inverse of the kernel ratio and our results thus predict that it is always lower for chains than for spheres, irrespectively of the concentration  $C_0$ . For neutrally buoyant cells, the clearance time is up to ten times shorter for chains than for spheres (Fig. 5.2A). This difference is further magnified by the fact that dead or senescent phytoplankton at the end of an algal bloom tend to be negatively buoyant and sink, which further increases encounters between elongated cells [Eq.(5.3)] but not between spherical cells (because identical spheres do not collide under gravitational settling [117, 132]). For example, modelling negatively buoyant ( $\Delta\rho = 50 \text{ kg/m}^3$ ) chain-forming diatom *Skeletonema* as chains consisting of 10 cells [130], each cell with dimensions  $4 \mu\text{m} \times 8 \mu\text{m}$  [109] (and thus  $l = 80 \mu\text{m}$ ,  $\lambda = 20$  in our model), the clearance time is about four days for conditions representative of the ocean surface layer ( $\varepsilon = 10^{-6} \text{ W/kg}$ ) and chain concentration  $C_0 = 500 \text{ mL}^{-1}$  [129]. This short clearance timescale is consistent for example with the timescale of one week needed to dissipate a recent bloom triggered by a volcano eruption in the North Pacific Ocean [133], which was dominated by *Skeletonema*. By contrast, the clearance time predicted for spheres of equal volume would have been more than nine days. For the most elongated phytoplankton, such as the filaments of *Trichodesmium* ( $l = 1 \text{ mm}$ ,  $\lambda = 100$  [111, 112]), the clearance times are even shorter and can be less than two days for a broad range of conditions (Fig. 5.3B; filament concentration  $C_0 = 10 \text{ mL}^{-1}$  [134]), consistent with field observations [135, 136]. As a result, the clearance is seven to tens of times faster for filaments than for equal-volume spheres (Fig. 5.3C).

The enhanced encounter rates of elongated cells may also help to rationalize marine snow composition. Genera commonly found on diatom aggregates, a type of marine snow that forms following algal blooms, are *Nitzschia*, *Chaetoceros*, *Rhizosolenia*, *Leptocylindricus*, *Skeletonema* and *Thalassionema* [122] – all of which have either elongated cells or grow as chains of cells. While this predominance may also reflect the relative prevalence of elongated species in the water column, our results suggest that an important role could be played by significantly enhanced encounter and thus coagulation rates among elongated species.

Our results also contribute to understanding colony formation among certain species of highly elongated phytoplankton. The needle-like cells of *Rhizosolenia* ( $\lambda$  up to 100 [109]) or

chains of cells of *Trichodesmium* ( $\lambda$  can exceed 100 [111, 112]) often form colonies composed of large numbers of individuals, called mats [123] or tufts and puffs [124], which can have very different properties from the individuals, for example higher vertical migration speeds [137], different microbiomes [138], and different biogeochemical functions [123]. Our results suggest that cell elongation facilitates the formation of such colonies by accelerating the rate at which they form from a suspension of individuals. For example, modeling *Trichodesmium* filaments as elongated rods ( $l = 1$  mm,  $\lambda = 100$ ,  $\Delta\rho = 80$  kg/m<sup>3</sup>) [124, 137], our results suggest that for a turbulent intensity characteristic of the ocean surface layer ( $\varepsilon = 10^{-6}$  W/kg) and an initial filament concentration of 1 mL<sup>-1</sup> [139], colonies start to emerge in less than a week, nearly nine-fold faster than they would if cells were spherical. Whether elongation in phytoplankton is a specific adaptation for colony formation is unclear, but our results indicate that elongation is an important phenotype in setting the timescale and thus ultimately the conditions of colony formation.

In conclusion, we presented results from direct numerical simulations of plankton encounters in turbulence, for the first time taking into account elongation, and distilled these into a single master curve that illustrates how turbulence and sinking each contribute to encounters. We found that elongation can accelerate encounters, and thus the timescale of the many ecological processes dependent on encounters, by up to an order of magnitude for neutrally buoyant cells and even more for buoyant ones, compared to spherical cells. Because to date most modeling of plankton encounters has assumed spherical cells [118], and because a majority of phytoplankton in the ocean are elongated [110], often with high aspect ratios [109], our results provide a substantial departure from the current understanding of ecological processes that depend on encounters. We illustrated the impact of accelerated encounters on bloom clearance and the associated process of marine snow formation, yet we expect that our results will be relevant for a range of other ecological processes, including mating [116], colony formation [123, 124], and biodiversification [109]. Taken together, our work shows that the elongated shape of many phytoplankton species has far-reaching, hitherto neglected consequences on their ecology by exerting a fundamental control on encounter rates.

## Acknowledgements

We thank Lukas Bentkamp and Ewelina Borowiecka for help with the figures, and Ulrike Pfreundt for early discussions. We thank Bérenger Bramas for code development related to the particle tracking and collision functionality in TurTLE.

**Funding** We gratefully acknowledge funding from an ETH Zurich Postdoctoral Fellowship and a Swiss National Science Foundation Ambizione Grant (No. PZ00P2\_202188) to J.S.; from a Gordon and Betty Moore Foundation Symbiosis in Aquatic Systems Investigator Award (GBMF9197), the Simons Foundation through the Principles of Microbial Ecosystems (PriME) collaboration (grant 542395) and the Swiss National Science Foundation, National Centre of Competence in Research (NCCR) Microbiomes (No. 51NF40\_180575) to R. S.; and from a Fulbright-Cottrell Award grant and the Max Planck Society to M. W.

**Competing interests** The authors declare no competing financial interests.

**Data and materials availability** Simulation outputs available upon request.

## 5.1 Supporting information

### 5.1.1 Turbulence simulations

We perform fully resolved direct numerical simulations of the incompressible Navier-Stokes equations in the vorticity formulation with our code TurTLE. This fluid flow solver is a highly parallelized pseudo-spectral code that allows for the integration of particle species advected with the fluid flow [61]. The incompressible Navier-Stokes equations take the form

$$\frac{\partial \mathbf{u}}{\partial t} + \mathbf{u} \cdot \nabla \mathbf{u} = -\nabla p + \nu \Delta \mathbf{u} + \mathbf{f}, \quad (5.6a)$$

$$\nabla \cdot \mathbf{u} = 0. \quad (5.6b)$$

Here,  $\mathbf{u}$  is the three-dimensional velocity field,  $p$  denotes the kinematic pressure, and  $\nu$  is the kinematic viscosity in code units.  $\mathbf{f}$  is a large-scale forcing that drives the flow to ensure a statistically stationary state.

We rescale the simulation units and parameters to physically and biologically relevant ones. In our simulations, we keep the large-scale forcing constant, and adjust viscosity (and simulation resolution) to achieve  $\varepsilon$  in the range  $10^{-6} - 10^{-9}$  W/kg, which corresponds to realistic oceanic values.

To convert from code units to physical units, let us denote  $\ell$  and  $\tau$  as the conversion factors from code units to physical units for space and time, respectively. Additionally, consider the integral length scale of the flow based on the longitudinal velocity autocorrelation function as  $L_{\text{int}}$ , and the code integral length  $\tilde{L}_{\text{int}}$ . Following this convention, symbols with a tilde refer to code units whereas symbols without tilde refer to physical units. Consistent with experiments in turbulence tanks, we set the integral length scale to  $L_{\text{int}} = 10$  cm - since the simulation domain is a cube with size  $\approx 6L_{\text{int}}$ , our simulations represent a turbulence tank of about 250 L [140]. From this we can fix  $\ell$  as

$$L_{\text{int}} = \tilde{L}_{\text{int}} \ell \Rightarrow \ell = \frac{L_{\text{int}}}{\tilde{L}_{\text{int}}}. \quad (5.7)$$

Additionally, we have to match water viscosity to physical units, which fixes  $\tau$

$$\nu = \tilde{\nu} \ell^2 \tau^{-1} \Rightarrow \tau = \frac{\tilde{\nu}}{\nu} \left( \frac{L_{\text{int}}}{\tilde{L}_{\text{int}}} \right)^2. \quad (5.8)$$

Using these conversion factors we can calculate the dissipation rate in physical units for a given dissipation rate in code units:

$$\varepsilon = \tilde{\varepsilon} \ell^2 \tau^{-3}. \quad (5.9)$$

Finally, we set rod length to a fixed length in physical units, i.e. mm, and rescale it correspondingly into code units. In Fig. 5.2A, we explored three rod lengths in the neutrally buoyant case, 0.5mm, 0.8mm, and 1.0mm. In Fig. 5.2B, we studied also neutrally buoyant rods and varied both aspect ratio and rod length, spanning the cases  $\lambda = 100$  and  $l = 1.0$ mm, as well as  $\lambda = 20$  and  $l = 80$   $\mu$ m. Finally, in Fig. 5.2C and 2D we kept the aspect ratio  $\lambda = 100$  and length  $l = 1.0$ mm fixed and scanned the density offset variable  $\Delta\rho$  and the turbulence intensity  $\varepsilon$ . In Fig. 5.2C, we concentrated on the biologically relevant  $\Delta\rho$  regime, while the collapse in Fig. 5.2D is based on a larger dataset that includes heavier rods to resolve the sinking dominated regime - this larger dataset is shown in Fig. 5.4. Other relevant values for the simulations used are reported in Table 5.1.

$N$	$k_M \eta_K$	$Re_\lambda$	$\varepsilon$ [W/kg]	$u_{\text{rms}}$ [mm/s]	$u_K$ [mm/s]	$N_{\text{part}}$
$1024^3$	2.89	177.1	$2.69 \times 10^{-6}$	8.662	1.281	$3.11 \times 10^6 - 1.03 \times 10^7$
$1024^3$	3.92	144.6	$8.48 \times 10^{-7}$	5.865	0.9597	$5.65 \times 10^5 - 1.11 \times 10^7$
$1024^3$	4.85	121.2	$3.68 \times 10^{-7}$	4.356	0.7786	$4.88 \times 10^5 - 1.18 \times 10^7$
$512^3$	2.89	111.0	$1.78 \times 10^{-7}$	3.477	0.6492	$3.06 \times 10^5 - 8.87 \times 10^6$
$512^3$	3.90	89.6	$5.83 \times 10^{-8}$	2.364	0.4913	$2.49 \times 10^5 - 9.46 \times 10^6$
$512^3$	4.85	75.8	$2.54 \times 10^{-8}$	1.768	0.3994	$2.16 \times 10^5 - 9.94 \times 10^6$
$256^3$	2.89	64.7	$1.28 \times 10^{-8}$	1.376	0.3364	$1.34 \times 10^5 - 7.42 \times 10^6$
$256^3$	4.82	44.5	$2.64 \times 10^{-9}$	0.7687	0.2268	$8.66 \times 10^4 - 7.25 \times 10^6$

Table 5.1: Simulation parameters.  $N$  is the number of grid points. The product  $k_M \eta_K$  of the largest resolved wavenumber  $k_M$  and the Kolmogorov scale  $\eta_K = (\nu^3/\varepsilon)^{1/4}$  quantifies the small-scale resolution of the simulations.  $Re_\lambda = \sqrt{15} u_{\text{rms}}^4 / (\varepsilon \nu)$  is the Reynolds number based on the Taylor microscale, where  $u_{\text{rms}}$  denotes the root mean square velocity component,  $\varepsilon$  the mean energy dissipation rate, and  $\nu = 10^{-6} \text{ m}^2/\text{s}$  the kinematic viscosity of water.  $u_K = (\nu \varepsilon)^{1/4}$  is the Kolmogorov velocity. We scanned a range of  $\Delta\rho$  with different numbers of colliding particles  $N_{\text{part}}$ . The range of simulated colliding particles is reported per simulation size above.

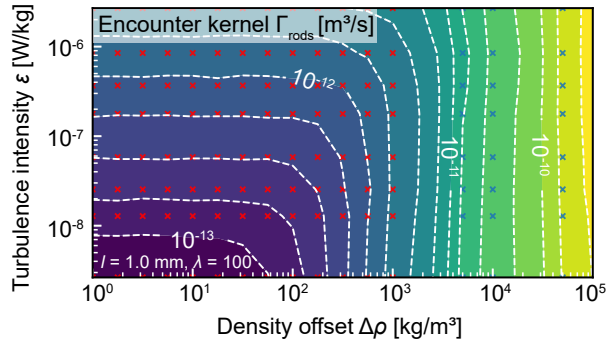


Figure 5.4: Shown is the full dataset that we used in Fig. 5.2D to demonstrate the data collapse onto the master curve. We note that, in Fig. 5.2C, we showed a subset of the above dataset (red crosses here are the same as the red crosses in Fig. 5.2C) to exclude the heaviest rods (blue crosses) to concentrate on a biologically relevant regime for *Trichodesmium*.

### 5.1.2 Simulation of sinking rods

The investigation of sinking anisotropic particles in turbulent flows has recently gained much attention, both from a fundamental point of view, but also with respect to applications in the atmospheric sciences and marine ecology (see e.g. [51, 55, 102, 141–143]).

To model sinking cells, we describe the positional and orientational dynamics of small thin elongated ellipsoidal particles sinking in a turbulent flow with no back-reaction onto the flow, and we neglect inertial effects owing to the fast relaxation timescales of planktonic cells [26, 51]. The particles are advected by the flow and have an orientation-dependent sedimentation velocity

$$\dot{\mathbf{x}} = \mathbf{u} + u_s (\beta_0 \hat{\mathbf{g}} + \beta_1 \hat{\mathbf{p}} \cdot \hat{\mathbf{g}} \hat{\mathbf{p}}). \quad (5.10)$$

Here,  $\mathbf{x}$  is the position of the particle,  $\mathbf{u}$  is the velocity field governed by Eq. (5.6) at the position of the particle and  $\hat{\mathbf{g}}$  is the direction of the gravitational acceleration. The characteristic

sedimentation speed of a single particle is given by

$$u_s = \frac{\Delta\rho V_{\text{rod}} g}{8\pi\mu l}. \quad (5.11)$$

Here,  $\Delta\rho := \rho_p - \rho_f$  is the difference between the particle  $\rho_p$  and the fluid  $\rho_f$  density,  $g$  is the magnitude of the gravitational acceleration,  $\mu$  is the dynamic viscosity of the fluid, and the length of the rods is given by  $l$ . Eq. (5.10) was derived for ellipsoidal particles. However, for consistency with our numerical collision algorithm (see below) we use here the volume of rods with spherical caps  $V_{\text{rod}} = \pi l^3 / (4\lambda^2) (1 - 1/3\lambda)$  with the same aspect ratio  $\lambda$ . Finally,  $\beta_0$  and  $\beta_1$  are functions that depend on  $\lambda$  and are given by given by [144]

$$\beta_0(\lambda) = \frac{\lambda^2}{\lambda^2 - 1} + \frac{2\lambda^3 - 3\lambda}{(\lambda^2 - 1)^{3/2}} \log \left[ \lambda + (\lambda^2 - 1)^{1/2} \right] \quad (5.12a)$$

$$\begin{aligned} \beta_1(\lambda) &= \frac{-3\lambda^2}{\lambda^2 - 1} + \frac{2\lambda}{(\lambda^2 - 1)^{3/2}} \log \left[ \lambda + (\lambda^2 - 1)^{1/2} \right] \\ &\quad + \frac{\lambda - 2\lambda^3}{(\lambda^2 - 1)^{3/2}} \log \left[ \lambda - (\lambda^2 - 1)^{1/2} \right]. \end{aligned} \quad (5.12b)$$

To determine the particles' orientational dynamics, we approximate their shape as ellipsoids with aspect ratio  $\lambda$  and integrate the particle orientation vector using Jeffery's equations [16]

$$\dot{\hat{\mathbf{p}}} = \frac{1}{2} \boldsymbol{\omega} \times \hat{\mathbf{p}} + \frac{\lambda^2 - 1}{\lambda^2 + 1} \left( S \hat{\mathbf{p}} - \hat{\mathbf{p}} \hat{\mathbf{p}}^T S \hat{\mathbf{p}} \right). \quad (5.13)$$

Here,  $\hat{\mathbf{p}}$  is the particle orientation,  $\boldsymbol{\omega} = \nabla \times \mathbf{u}$  is the vorticity, and  $S_{ij} = (\partial_j u_i + \partial_i u_j) / 2$  is the strain tensor, which induce particle spinning and tumbling depending on the shape of the particles.

### 5.1.3 Encounter detection algorithm

Particle encounters are measured using the so-called ghost encounters [57], i.e. particles may overlap but do not interact during collisions. For the encounter detection algorithm, we approximate the particles as thin rods with spherical caps (Fig. 5.1D). Encounters between thin rods can be calculated by searching for the minimal distance between the two symmetry axes of the rods. Consider a first rod at a position  $\mathbf{x}$  with orientation  $\hat{\mathbf{p}}$ , and a second rod with orientation  $\hat{\mathbf{q}}$  at a position  $\mathbf{y}$ . Both rods have length  $l$  and width  $w$ . Positions along the rods may be parameterized by use of the parameters  $t, s \in [-1, 1]$ , such that any point along the symmetry axis of the rods may be written as

$$\mathbf{r}_1(t) = \mathbf{x} + t \left( 1 - \frac{1}{\lambda} \right) \frac{l}{2} \hat{\mathbf{p}}; \quad t \in [-1, 1] \quad (5.14)$$

for the first rod, and

$$\mathbf{r}_2(s) = \mathbf{y} + s \left( 1 - \frac{1}{\lambda} \right) \frac{l}{2} \hat{\mathbf{q}}; \quad s \in [-1, 1] \quad (5.15)$$

for the second. The distance between two points on symmetry axis of the rods is then

$$\begin{aligned} \text{dist}(t, s) &= \sqrt{[\mathbf{r}_1(t) - \mathbf{r}_2(s)]^2} \\ &= \sqrt{\left[ \frac{l}{2} \left( 1 - \frac{1}{\lambda} \right) (\hat{\mathbf{p}} t - \hat{\mathbf{q}} s) + \Delta\mathbf{x} \right]^2}, \end{aligned} \quad (5.16)$$

where  $\Delta \mathbf{x} = \mathbf{x} - \mathbf{y}$ . The minimum distance can be found by setting the gradient of this distance function to zero. This leads to a linear system, which can be solved leading to

$$\begin{pmatrix} t_{\min} \\ s_{\min} \end{pmatrix} = \frac{2}{l(\lambda - 1)} \frac{\lambda}{(\hat{\mathbf{p}} \cdot \hat{\mathbf{q}})^2 - 1} \times \begin{pmatrix} 1 & -\hat{\mathbf{p}} \cdot \hat{\mathbf{q}} \\ \hat{\mathbf{p}} \cdot \hat{\mathbf{q}} & -1 \end{pmatrix} \begin{pmatrix} \Delta \mathbf{x} \cdot \hat{\mathbf{p}} \\ \Delta \mathbf{x} \cdot \hat{\mathbf{q}} \end{pmatrix}. \quad (5.17)$$

This yields the minimum distance if  $|t_{\min}| \leq 1$  and  $|s_{\min}| \leq 1$ . If  $|t_{\min}| \geq 1$  or  $|s_{\min}| \geq 1$ , we must search for the minimum distance along  $|t| = 1$  and  $|s| = 1$ . In these last cases, the minimum distance can be analytically found. For  $t_{\min} = \pm 1$

$$s_{\min} = t_{\min} \hat{\mathbf{p}} \cdot \hat{\mathbf{q}} + \frac{2}{l} \frac{\lambda}{\lambda - 1} \Delta \mathbf{x} \cdot \hat{\mathbf{q}}. \quad (5.18)$$

For  $s_{\min} = \pm 1$

$$t_{\min} = s_{\min} \hat{\mathbf{p}} \cdot \hat{\mathbf{q}} - \frac{2}{l} \frac{\lambda}{\lambda - 1} \Delta \mathbf{x} \cdot \hat{\mathbf{p}}. \quad (5.19)$$

Particle overlaps at a given time snapshot can then be detected by  $\text{dist}(t_{\min}, s_{\min}) < w$ . This means, at their minimum distance the rods are less than one width apart from one another.

We then keep track of overlaps of particle pairs. At every time step we compare the overlap of particle pairs with the ones from the previous time step. If a change in the overlap of a particle pair is detected that was not detected in the previous time step, we count that encounter pair as a new encounter. This new encounter contributes to the number of new encounters  $N_{\text{enc}}$ . Given a number of new encounters  $N_{\text{enc}}$  in a given time  $T$ , volume  $V$ , and total number of particles  $N_{\text{part}}$ , the encounter kernel is then obtained as [57]

$$\Gamma = \frac{2 V N_{\text{enc}}}{N_{\text{part}}^2 T}. \quad (5.20)$$

In our simulations, the simulation domain is a cube with side length  $2\pi$  and volume  $V = 8\pi^3$  in code units. We typically run the simulations for time  $T$  on the order of several integral times (in code units). For our choice of particle numbers  $N_{\text{part}}$  (see Table 5.1), these simulation times guarantee statistical convergence of the kernel estimate in Eq. (5.20). We also remove an initial transient time of two integral time scales, which allows for the large-scale spatial distribution of particles to reach a statistically stationary state. Thus, with the number of detected encounters ( $N_{\text{enc}}$  is on the order of a thousand encounters per integral time), Eq. (5.20) gives us an encounter kernel in code units, with units of  $\text{space}^3/\text{time}$ . Finally, using the transformation factors in Eqs. (5.7) and (5.8) this quantity may then be transformed into physical units.

#### 5.1.4 Comparison of encounter kernels

In the main text, we compare the encounter kernel of elongated particles with the encounter kernel of spheres with an equal volume. We explain the details of this comparison in the following.

The encounter kernel of passive tracer spheres of radius  $r$  advected by turbulence is given by the Saffmann-Turner kernel [56]

$$\Gamma_{\text{ST}}(r) = 1.3 (2r)^3 \sqrt{\frac{\varepsilon}{\nu}}. \quad (5.21)$$

In our simulations, we represent a rod as a cylinder with spherical caps at both ends of the cylinder. The cylinder has length  $l(1 - 1/\lambda)$  and width  $l/\lambda$ . The spherical caps have diameter  $l/\lambda$ , so that the total length of the rod with spherical caps is  $l$ . We now calculate the volume of these rods and obtain the equivalent radius  $r_{\text{eq}}$  of spheres with the same volume. Using  $r_{\text{eq}}$  and the Saffman-Turner kernel (5.21) gives us then a baseline encounter kernel to compare the effect of shape on encounters. The rods with spherical caps have volume

$$V_{\text{rods}} = \frac{4\pi}{3} \left(\frac{l}{2\lambda}\right)^3 + \pi l \left(1 - \frac{1}{\lambda}\right) \left(\frac{l}{2\lambda}\right)^2. \quad (5.22)$$

Consider now the spheres of equivalent radius  $r_{\text{eq}}$ , with volume  $V_{\text{sphere}} = 4\pi r_{\text{eq}}^3/3$ . By demanding  $V_{\text{rods}} = V_{\text{sphere}}$ , we can solve for  $r_{\text{eq}}$

$$(2r_{\text{eq}})^3 = \frac{l^3}{2\lambda^2} \left(3 - \frac{1}{\lambda}\right). \quad (5.23)$$

The Saffman-Turner kernel for these equal-volume spheres is then

$$\Gamma_{\text{ST}}^{\text{eq}}(l, \lambda) = \Gamma_{\text{ST}}(r_{\text{eq}}) = \frac{1.3}{2\lambda^2} \left(3 - \frac{1}{\lambda}\right) l^3 \sqrt{\frac{\varepsilon}{\nu}}. \quad (5.24)$$

The encounter kernel of neutrally buoyant tracer rods in turbulence  $\Gamma_{\text{rods}}^{\text{n.b.}}$  can therefore be measured as an aspect-ratio dependent deviation from  $\Gamma_{\text{ST}}^{\text{eq}}$ . As a result, we obtain

$$\Gamma_{\text{rods}}^{\text{n.b.}}(l, \lambda) = \Gamma_{\text{ST}}^{\text{eq}}(l, \lambda) C'(\lambda). \quad (5.25)$$

The function  $C'(\lambda)$  quantifies how much more rods of a certain aspect ratio collide compared to equal-volume spheres. This function can be fitted by

$$C'(\lambda) = a(\lambda^2 - 1) + b(\lambda - 1) + 1. \quad (5.26)$$

This quantity is plotted in Fig. 5.2A. We used a non-linear least squares regression to estimate the best fit of free parameters to  $a = 6.0864 \times 10^{-5}$  and  $b = 5.6100 \times 10^{-2}$ . The fit ensures that for aspect ratio  $\lambda = 1$  rods we exactly obtain the Saffman-Turner limit, i.e.

$$\Gamma_{\text{rods}}^{\text{n.b.}}(l, \lambda = 1) = \Gamma_{\text{ST}}(l/2). \quad (5.27)$$

Comparing then Eqs. (5.25) and (5.2) we can write the fit function  $C(\lambda)$  as

$$C(\lambda) = \frac{1}{2\lambda^2} \left(3 - \frac{1}{\lambda}\right) C'(\lambda). \quad (5.28)$$

As we showed above, by construction  $C(\lambda = 1) = 1$ , so that in the case of spheres the Saffman-Turner kernel is exactly recovered with this fit.

### 5.1.5 Scaling arguments for the encounter kernel

To further rationalize the functional form of the new kernel  $\Gamma_{\text{rods}}^{\text{n.b.}}$  in Eq. (5.2), we developed simple scaling arguments. We first consider two identical spherical cells in turbulence, smaller than the Kolmogorov length scale, the scale at which viscosity dissipates the fluid kinetic energy, which in the ocean is typically in the range 1 – 6 mm [145, 146]. Their relative velocity

$\Delta u$  at the time of encounter scales as  $\Delta u \sim r\sqrt{\varepsilon/\nu}$ , i.e. the sphere radius times the shear rate  $\sqrt{\varepsilon/\nu}$  at the Kolmogorov length scale. Since the encounter cross-section for spheres scales as  $r^2$ , the rate of volume swept by spheres scales as  $r^2\Delta u \sim r^3\sqrt{\varepsilon/\nu}$ , which is the classic kernel  $\Gamma_{\text{ST}}$  in Eq. (5.1) up to a constant. Turning to elongated cells, both the typical distance and the encounter cross-section at the time of encounter depend on the orientations of the two cells, so that the relevant length scale can be as large as the cell length  $l$  or as small as its width  $l/\lambda$ , depending on whether the orientations are random or aligned and the encounter is head on. Since this length scale impacts both the encounter cross-section, which can be as small as  $(l/\lambda)^2$  or as large as  $l^2$ , and the cells' relative velocity, which can be as small as  $l/\lambda\sqrt{\varepsilon/\nu}$  or as large as  $l\sqrt{\varepsilon/\nu}$ , the rate of volume swept by elongated cells relative to each other thus depends on all the possible combinations  $l^3$ ,  $l^3/\lambda$ ,  $l^3/\lambda^2$ , etc. We thus expect that the encounter kernel for elongated cells scales as  $l^3\sqrt{\varepsilon/\nu}$  times a function of the aspect ratio  $\lambda$ . Our scaling analysis thus validates the semi-empirical formula we derived from the numerical simulations in Eq. (5.2), except for the aspect ratio dependence which cannot be obtained by scaling arguments and which depends on details of the competition between the randomizing and shear-induced aligning effects of turbulence.

### 5.1.6 Comparison with cylinders in simple shear flow

Here, we compare our results with a previous work on encounters between cylinders in simple shear flow [131]. We first note that, as derived by Smoluchowski [147], for spherical particles of radius  $r$  in simple shear flow the encounter kernel reads

$$\Gamma_{\text{spheres}}^{\text{shear}} = \frac{4}{3}(2r)^3\gamma, \quad (5.29)$$

where  $\gamma$  is the shear rate. Remarkably, this classic result can be mapped onto the Saffman-Turner kernel for spheres in turbulence if one replaces the shear rate  $\gamma$  with the turbulent shear  $\sqrt{\varepsilon/\nu}$  - this mapping reproduces Eq. (5.1) to within 3%. Could a similar relationship hold between elongated cells in simple shear flow as studied in [131] and our results?

In [131], the encounter rate between cylinders (without spherical caps) of aspect ratio  $\lambda$  was measured numerically and compared with Eq. (5.29) as follows

$$\Gamma_{\text{cylinders}}^{\text{shear}} = f\Gamma_{\text{spheres}}^{\text{shear}}, \quad (5.30)$$

where  $f(\lambda)$  was termed ‘fractional collision frequency’, and  $r$  was set to be the radius of the circumscribing sphere  $r = l\sqrt{1 + \lambda^{-2}}/2$ . For high aspect ratios and assuming that one can replace the shear rate  $\gamma$  in Eq. (5.30) with the turbulent shear rate  $\sqrt{\varepsilon/\nu}$ , the definition of  $f(\lambda)$  and  $C(\lambda)$  in our Eq. (5.2) should be similar to each other if the encounters between elongated cells in turbulence are similar in nature to encounters between cylinders in simple shear flow. In Fig. 5.5, we plot  $f(\lambda)$  and  $C(\lambda)$  in the range  $10 < \lambda < 100$  and found that, remarkably, the two prefactors agree to within a factor of two (Fig. 5.5A). However, taking the ratio of the two prefactors shows that turbulence increases encounter rates as compared to simple shear flow as the aspect ratio increases, doubling the rate at  $\lambda = 100$  with asymptotic scaling  $\lambda^2/\log(\lambda)$  for large  $\lambda$  (Fig. 5.5B).

### 5.1.7 Clearance times and critical concentrations

In the main text, we analyzed the impact of elongation on the bloom clearance time  $T_c$  [Eq. (5.5)]. Here, we first briefly derive Eq. (5.5) and then discuss critical cell concentrations [129, 148],

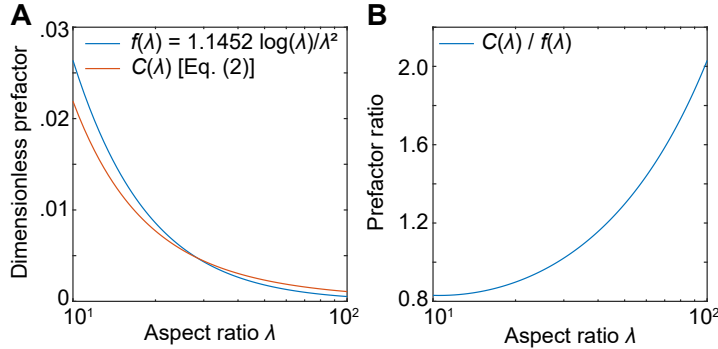


Figure 5.5: Comparison with the encounter kernel for cylinders in simple shear flow studied in [131]. **A** Dimensionless prefactors  $f(\lambda)$  studied in [131] and  $C(\lambda)$  in our Eq. (5.2). **B** The ratio of the two quantities shows that the two prefactors agree to within a factor of two, albeit the turbulent prefactor  $C(\lambda)$  is consistently larger than  $f(\lambda)$  as the aspect ratio increases – the ratio scales like  $\lambda^2/\log(\lambda)$  for large  $\lambda$ .

an alternative way to describe the impact of elongation on the bloom dynamics.

To derive Eq. (5.5), we consider a monospecific bloom of identical chains of cells that grow exponentially until they, for example, deplete nutrients. We denote by  $C_0$  the maximal concentration of individual cells reached at the moment of the nutrient depletion. We then assume that cells die, become sticky, and start to sink. As they sink, they are mixed by turbulence, encounter one another and form composite particles (marine snow) by sticking to each other. The concentration  $C(t)$  of individual chains thus decreases with time because they are converted into composite particles as described by the truncated version of the Smoluchowski coagulation equation [147]

$$dC/dt = -\Gamma_{\text{rods}}C^2, \quad (5.31)$$

where  $\Gamma_{\text{rods}}$  is given by Eq. (5.3) for elongated chains and is replaced by Eq. (5.1) for spherical cells. Eq. (5.31) is a truncated version of the full coagulation equation, because we neglect chain removal via higher-order encounters, such as encounters between individual chains and marine snow composed of two chains, etc. This approximation is valid during the initial stages of the marine snow formation, which is of our interest here, because the concentration of composite particles are small compared to  $C(t)$  and thus the additional decrease in  $C(t)$  due to higher-order encounters can be neglected. The solution of Eq. (5.31) with initial conditions  $C(0) = C_0$  is

$$C(t) = \frac{C_0}{C_0\Gamma_{\text{rods}}t + 1}. \quad (5.32)$$

We define the bloom clearance timescale  $T_c$  to be the time required for half of the individual chains to be converted into composite particles. This corresponds to putting  $C(T_c) = C_0/2$ , and solving for  $T_c$  reproduces Eq. (5.5).

Following [129, 148], we further compute the critical chain concentrations as an alternative way to characterize the impact of cell elongation on the bloom dynamics. In this model of marine snow formation, chains are taken to be sticky at all times, including the growth stage, and thus marine snow particles form even during the cell division stage. Mathematically,

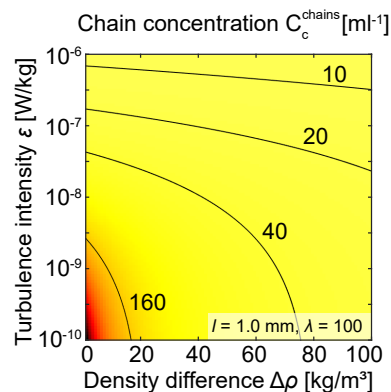


Figure 5.6: Impact of elongation on the critical chain concentration that triggers marine snow formation. Predicted critical chain concentration [Eq. (5.34)] as a function of the turbulence intensity and cell's density offset for growth rate  $\alpha = 1 \text{ d}^{-1}$  (other parameters are the same as in Fig. 5.3).

Eq. (5.31) is replaced with

$$dC/dt = \alpha C - \Gamma_{\text{rods}} C^2, \quad (5.33)$$

where  $\alpha$  is the cell growth rate. The critical concentration  $C_c^{\text{rods}}$  is derived by setting the right hand side of Eq. (5.33) to zero, which corresponds to the assumption that the chain growth is balanced by the chain removal due to coagulation. We obtain

$$C_c^{\text{chains}} = \alpha / \Gamma_{\text{rods}}. \quad (5.34)$$

Similarly to the clearance time considerations in the main text, we find that critical concentrations for elongated cells are lower than for spherical cells by a factor given by the ratio of the corresponding kernels (Fig. 5.3C). Thus, sticky chains need to build up lower chain concentrations for coagulation to start converting chains into marine snow. For example, for the most elongated filaments of *Trichodesmium* ( $l = 1 \text{ mm}$ ,  $\lambda = 100$ ) taking the growth rate  $\alpha = 1 \text{ d}^{-1}$ , we predict that the critical filament concentrations can be below  $C_c^{\text{chains}} = 10 \text{ mL}^{-1}$  (Fig. 5.6), consistent with field observations [134–136].



---

Part IV

—  
Conclusions

---

## Summary & discussion

In this dissertation we have studied physical models of microorganisms in fluid flows. We studied models of motile and sedimenting microorganisms in mildly turbulent flows. Our findings can be summarized as follows.

### Microswimmers in an axisymmetric vortex flow

Realistic turbulent flows are chaotic, and it is difficult to study the mathematical properties of a specific modeling approach. Previous studies have revealed intricate dynamics in toy-model flows, such as the Poiseuille flow [78–80] and simple two-dimensional vortex [81–84]. These approaches have allowed a straightforward characterization of the dynamic and chaotic properties of the kinds of models physicists use to study microswimmers [79].

Using a two-dimensional vortex flow toy-model we studied the effect of shape and motility on microswimmer dynamics. We explicitly uncovered the Hamiltonian structure of the dynamics for spherical microswimmers, and we showed how shape breaks the Hamiltonian structure and introduces clustering via phase-space contraction. Additionally, we were able to identify microswimmers which remain bound to the vortex as a function of their shape and motility. We showed that elongated ellipsoids escape the vortex at lower speeds than oblate ellipsoids. We showed that at sufficiently high speed all microswimmers escape the vortex flow, and we related this to the mathematical properties of the system through a saddle-node bifurcation of the system's fixed-points.

### Dispersion statistics and collision rates of motile ellipsoidal particles in mild turbulence

Physicists have modeled microswimmers in turbulence for a long time as non-inertial ellipsoidal-shaped particles [15]. Within this approach the rotation induced by the flow on the particles can be computed by the Jeffery's equations [16]. Scientists have studied various aspects of these models as a function of shape, motility, and the turbulent flow [17, 19, 23, 24, 36, 38, 72, 101, 104–106]. In our case we contributed to the current scientific knowledge by carrying out systematic measurements of rotation rates and transport properties of microswimmers in turbulence as a function of their shape and motility. Additionally, we carried out measurements of collision rates of spheres of different motility and size.

We learned that rotation rates of motile ellipsoids in turbulence depend on the particle's shape and motility. We identified two shape-dependent limiting cases. The limit of uncorrelated orientation is obtained when the ellipsoid orientation is totally uncorrelated from the underlying flow. In the limit of passive tracers the advected ellipsoids develop correlations with the underlying flow, as Jeffery's equations [16] dictates their orientational dynamics. We found out that motility is the control parameter interpolating between these two limiting cases. In the very fast limit the motile ellipsoids are so fast that there is no time to establish correlations with the underlying fluid flow, such that their orientation is effectively uncorrelated, leading to the uncorrelated limit. On the other hand we obviously obtain the correlated limit in the non-motile passive tracer limit. Notably, we also found that the rotation rates of spheres remain unchanged as a function of motility. This is a direct consequence of the fact that the dynamics of spheres conserve phase space. This is hence a direct consequence of a property we already uncovered and quantified in the two-dimensional toy-model through the presence of the Hamiltonian structure of the dynamics. Finally, we observed that prolate ellipsoids tend to spin throughout, while oblate ellipsoids tend to tumble more than they spin.

Additionally we studied the transport properties of motile ellipsoids by measuring the mean squared displacement (MSD). We studied both the short- and long-time behavior of this quantity. By carefully studying the individual contributions to the MSD we concluded that cross terms depending on correlation terms play a crucial role in determining the shape-dependent behavior. We found that both for the long- and short-time limits the prolate ellipsoids disperse faster than other shapes. We were able to bring this result into the context of tumbling rates. As oblate ellipsoids tumble more, they change their orientation more often, this leading to diminished transport.

Finally, we also looked at the collision rates of motile spheres of different sizes. By rescaling we found a master curve interpolating between the passive tracer limit, known as the Saffman-Turner collision kernel, and a motile limit. The transition happens at a speed much smaller than the Kolmogorov speed of the flow.

## **Elongation enhances encounter rates between phytoplankton in turbulence**

Elongated planktonic species can form macroscopic blooms in the ocean. We measured the collision rates of elongated sedimenting particles in mild turbulence. We were able to find an expression generalizing the Saffman-Turner expression for elongated passive particles as a function of shape, size, and turbulence intensity. We were able to show that shape considerably increases collision rates of elongated particles when compared to passive spheres of equal volume. We then carried out parameter studies as a function of turbulence intensity and density offset. We reduced the parameter dependence on density offset and turbulence intensity to a master curve, which interpolates between a passive tracer limit, and a sedimenting dominated regime. Compared to equal volume spheres, elongated particles have increased collision rates. This leads to a several fold decrease in expected formation times of plankton blooms, thus helping to explain rapid bloom formation.

## **Conclusions**

In this dissertation we have taken several modeling approaches to study microorganisms in mildly turbulent flows. We concentrated on the cases of motility and sedimentation as migration strategies presented by different organisms to navigate in the water column. By studying

a simplified two-dimensional toy-model we were able to explicitly study the mathematical properties of the modeling approach used for microswimmers in fluid flows, and we uncovered a shape-dependent Hamiltonian structure. Furthermore, we were able to explain why in this simple toy-model picture prolate ellipsoids can more easily escape the vortex than other shapes. Moving on to realistic turbulent flows we observed similar behavior: due to shape-dependent rotation rates, elongated ellipsoids have higher transport properties than other shapes both in long- and short time measurements. For survival in the ocean, these results might provide an advantage when navigating the oceanic medium for grazing, or dispersing quickly to avoid predation. Additionally, these results might point to an advantage of elongated organisms developing motility over other shapes.

Another critical quantity for the survival of microorganisms in the ocean is their given collision rate. As many organisms need to graze or meet for mating, this quantity may be considered as a crucial metric for the survival of these motile species in the ocean. In our studies we were able to extract a master curve extrapolating between a passive tracer limit, and a motile limit. The transition between these two limiting cases happens at a very low swimming speed; much lower than the Kolmogorov speed of the flow. Biologically speaking, this means that a very small swimming speed suffices for microorganisms to considerably enhance the probability of meeting other microorganisms. This might hint at a possible reason why microorganisms have evolved motility as a viable migration strategy. By a relatively small energetic effort, a microscopic organisms might considerably increase its probability of grazing or mating.

Finally, we studied the collision rates of elongated sedimenting microorganisms in mild turbulence. We obtained a generalized version of the Saffman-Turner collision kernel, describing collision rates of elongated passive particles in a turbulent flow as a function of their shape, size, and the turbulence intensity. We observed that compared to equal-volume spheres, elongated particles have enhanced collision rates. Then, by expanding onto the sedimenting case, in which the microorganisms have a density offset to the surrounding fluid, we also observed shape dependence in the collision rates in this limit. These results shed light on previously not observed properties, such as how shape affects collision rates. Furthermore, this shape-dependence has direct consequences in the formation of planktonic blooms. The severalfold increase in the collision rates of elongated sedimenting microorganisms in the ocean, compared to equal volume sedimenting spheres, has helped to explain the timescales in which blooms of sedimenting planktonic species form.

Planktonic microorganisms play a crucial role in the ocean. The survival strategies of planktonic species, as well as the formation of planktonic blooms play a fundamental role in chemical cycles, trophic chains, and oceanic ecology. In this dissertation we have approached this problem with a physical modeling approach. We have shed light on transport and collision properties of motile microorganisms, important quantities in the survival of planktonic organisms in the oceanic medium. Additionally, we shed light on the mechanism underlying the formation of planktonic blooms of sedimenting elongated plankton. These findings help to advance the efforts of physicists to explain with a mechanistic approach the dynamics of planktonic microorganisms in the ocean.

---

Part V

—  
Appendix

---

## Manuscript III

In this first part of the appendix we present a manuscript which originally appeared as "**Arguedas-Leiva, J.-A.**, Carroll, E., Biferale, L., Wilczek, M. and Bustamante, M.D. (2022). [A minimal phase-coupling model for intermittency in turbulent systems](#). *Physical Review Research*, 4 (L032035)" and is licensed under the [Creative Commons Attribution 4.0 licence \(CC BY 4.0\)](#).

L. B., M. W., and M. D.B designed the study and led discussion and analysis of the results. J-A. A-L. and E. C. wrote the code, carried out simulations, analyzed the data, and produced the figures. J.-A. A.-L., E. C., L. B., M. W., and M. D.B. wrote the paper.

# A minimal phase-coupling model for intermittency in turbulent systems

José-Agustín Arguedas-Leiva,<sup>1</sup> Enda Carroll,<sup>2</sup>  
Luca Biferale,<sup>3</sup> Michael Wilczek,<sup>1,4†</sup> Miguel D. Bustamante<sup>2</sup>

<sup>1</sup>Max Planck Institute for Dynamics and Self-Organization,  
Am Faßberg 17, 37077 Göttingen, Germany

<sup>2</sup>School of Mathematics and Statistics, University College Dublin,  
Belfield, Dublin 4, Ireland

<sup>3</sup>Dept. Physics and INFN, University of Rome Tor Vergata,  
Via Ricerca Scientifica 1, 00133 Rome, Italy

<sup>4</sup>Theoretical Physics I, University of Bayreuth,  
Bayreuth, Germany

<sup>†</sup>To whom correspondence should be addressed; E-mail: michael.wilczek@uni-bayreuth.de .

## Abstract

Turbulent systems exhibit a remarkable multi-scale complexity, in which spatial structures induce scale-dependent statistics with strong departures from Gaussianity. In Fourier space, this is reflected by pronounced phase synchronization. A quantitative relation between real-space structure, statistics, and phase synchronization is currently missing. Here, we address this problem in the framework of a minimal deterministic phase-coupling model, which enables a detailed investigation by means of dynamical systems theory and multi-scale high-resolution simulations. We identify the spectral power-law steepness, which controls the phase coupling, as the control parameter for tuning the non-Gaussian properties of the system. Whereas both very steep and very shallow spectra exhibit close-to-Gaussian statistics, the strongest departures are observed for intermediate slopes comparable to the ones in hydrodynamic and Burgers turbulence. We show that the non-Gaussian regime of the model coincides with a collapse of the dynamical system to a lower-dimensional attractor and the emergence of phase synchronization, thereby establishing a dynamical-systems perspective on turbulent intermittency.

## A.1 Introduction.

Turbulence is a prototypical non-equilibrium phenomenon with a large number of strongly interacting degrees of freedom [41, 42, 44, 149–151], exhibiting strong departures from Gaussianity on the smallest spatial scales. In real space, non-Gaussian fluctuations can be related to coherent, intense, and rare events in the velocity gradients – a phenomenon also dubbed as

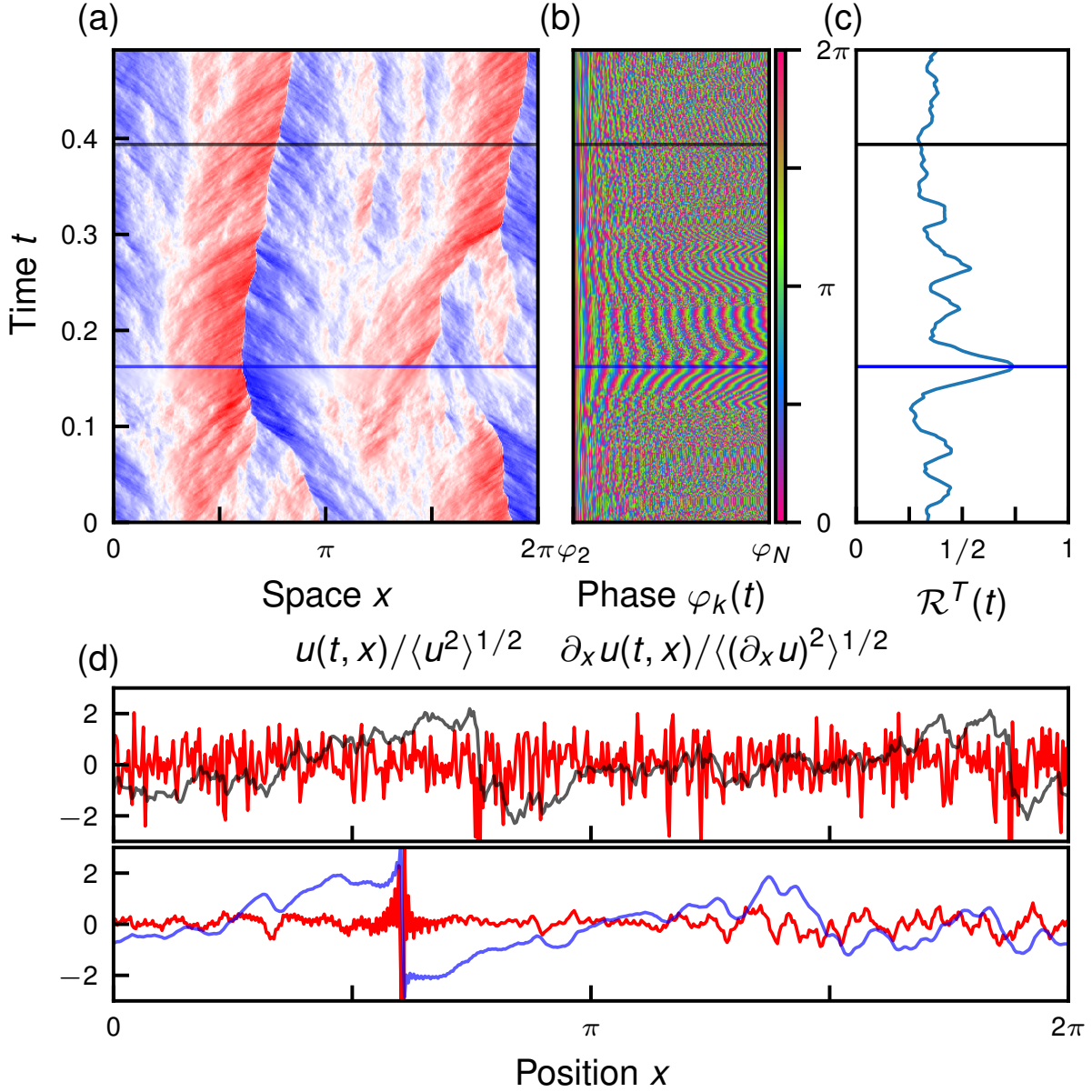


Figure A.1: Numerical simulations of (A.6) with  $k_0 = 1$  and  $N = 2^9$ , with a Burgers-like steepness parameter  $\alpha = 1$ . (a) Plot of the real-space field  $u(t, x)$  displaying a shock near  $x = \pi/2$  at the time indicated by the blue line. The field  $u(t, x)$  is obtained by solving the phase dynamics (A.6) and inserting the time-evolving phases into (A.2) for prescribed amplitudes  $a_k$ . (b) Plot of individual phases  $\varphi_2, \dots, \varphi_N$ . The gray line marks an instance of a relatively disordered regime while the blue line marks a relatively synchronized regime. (c) Time-dependent order parameter  $\mathcal{R}^T(\alpha, t)$ , cf. Eq. (A.10), for the synchronization of the system (here with  $T = 0.0244$ ). The peak corresponds to a synchronization event related to a real-space shock. (d) Snapshots of the real-space field  $u(t, x)$  in the disordered (top, gray) and synchronized (bottom, blue) regimes. Red curves show the gradient  $\partial_x u(t, x)$  to illustrate the difference between the two regimes.

*intermittency* [152, 153]. Intermittency can also be studied from the complementary perspective of Fourier space. While Gaussian random fields feature completely uncorrelated phases, phase correlations can give rise to complex scale-dependent properties, as the ones developed in the presence of coherent shocks. Elucidating these connections is important for both fundamental and applied aspects. In particular, we currently miss a clear identification of which dynamical degrees of freedom lead to such bursting and quiescent chaotic alternations of temporal and spatial flow realizations. As a result, we lack optimal protocols to avoid disrupting fluctuations in engineering turbulence [154, 155], predict extreme events in geophysical flows [156, 157] and control existence and uniqueness of the PDE solutions [158], just to cite a few open problems with multidisciplinary impacts. Studying these issues in fully developed three-dimensional turbulence is an extremely challenging task. The hope is to isolate the main aspects of this problem in simpler, more tractable models. One popular way is to lower the complexity by mode reduction, as in the case of sub-grid-scale modeling [159, 160], Fourier surgery [161, 162], statistical closure [163], partial freezing of some spectral degrees of freedom [164, 165] or asymptotic expansions [166, 167]. All attempts have merits and deficiencies, the main common drawback being the compromised ability to describe simultaneously spatial and temporal fluctuations on a wide range of scales. Notably, only very few studies have addressed the connection between the emergence of coherent intermittent structures in real space and phase correlations, connecting the presence of bursts of spectral energy fluxes (and dissipation) with Fourier phase dynamics [168–172].

In this letter we combine theory and simulations to provide a dynamical systems link between real-space intermittency and phase correlations in Fourier space. We do so by means of a minimal deterministic description of hydrodynamic turbulence derived from a PDE model, preserving the whole richness of multi-scale spatial and temporal statistics. The model is formulated in terms of Fourier phases whose dynamical coupling resembles the one in Navier-Stokes turbulence: specifically, it is Burgers turbulence with the important distinction that the amplitudes are kept at fixed values such that only the phases evolve, obeying a deterministic system that supports a turbulent attractor.

By changing the energy spectrum slope we can tune the coupling strength of the phases and study how the dynamics (intermittency) changes. We find that the system transitions to non-Gaussian statistics as the spectrum is gradually steepened. For slopes beyond a certain value, the rare fluctuations become less extreme and return to near-Gaussian statistics. Strikingly, the strongest deviations occur in the intermediate range, within the range of values attained by turbulent systems. Within this range, the dimension of the strange attractor collapses to a minimum, indicating that non-Gaussian real-space statistics are related to the collapse of the dynamical system onto a lower-dimensional manifold.

Our analysis sheds light on the emergence of coherent structures and the associated phase synchronization phenomena <sup>1</sup>, establishing connections between the statistical theory of non-equilibrium systems and dynamical systems theory.

---

<sup>1</sup>In this paper, *synchronization* is understood as a transient state whereby the phases of the Fourier modes over an extended range of spatial scales evolve following similar patterns, showing strong correlations during finite time intervals. This is similar to the definition used in classical phase models [173, 174], although our work is the first, to our knowledge, to study synchronization in a Fourier phase model based on a system with quadratic nonlinearity.

## A.2 The model

As a starting point, let us consider the one-dimensional Burgers equation

$$\partial_t u(t, x) + u(t, x) \partial_x u(t, x) = \nu \partial_x^2 u(t, x). \quad (\text{A.1})$$

This simple prototypical PDE is reminiscent of the Navier-Stokes equations, known to develop multi-scale bifractal scaling properties, shocks, non-Gaussian statistics and many other non-trivial statistical features [175–184]. We consider a one-dimensional field  $u(t, x)$  on a  $2\pi$ -periodic domain with Fourier decomposition

$$u(t, x) = \sum_{k \in \mathbb{Z}} a_k(t) \exp(i[(\varphi_k(t) + kx)]). \quad (\text{A.2})$$

By inserting (A.2) into (A.1), we obtain the evolution for the amplitudes and the phases

$$a_k \frac{d\varphi_k}{dt} = -\frac{k}{2} \sum_{p \in \mathbb{Z}} a_p a_{k-p} \cos(\varphi_p + \varphi_{k-p} - \varphi_k), \quad (\text{A.3})$$

$$\frac{da_k}{dt} = \frac{k}{2} \sum_{p \in \mathbb{Z}} a_p a_{k-p} \sin(\varphi_p + \varphi_{k-p} - \varphi_k) - \nu k^2 a_k. \quad (\text{A.4})$$

This infinite set of coupled ODEs describes the full Burgers dynamics of the Fourier phases and amplitudes. Recently, we showed that the dynamics of the Fourier phases  $\varphi_k(t)$  determine to a great extent the shock dynamics and the associated non-Gaussian statistics when the amplitudes follow a Burgers-like scaling [172]. In order to establish a deeper dynamical systems understanding of the role of Fourier phases in turbulence, we now follow a different approach, by introducing a minimal *deterministic* model enjoying a turbulent attractor. Take equation (A.3) as a starting point and set the amplitudes to prescribed constants

$$a_k = |k|^{-\alpha}, \quad |k| > k_0, \quad a_k = 0, \quad |k| \leq k_0, \quad (\text{A.5})$$

where the steepness  $\alpha$  is our new *continuous control parameter* and  $k_0 > 0$  is a large-scale cutoff leading to a finite integral length scale, which destabilizes a single-shock-like fixed point, allowing thus for a turbulent attractor. The phase dynamics is obtained from (A.3) which becomes a system of coupled oscillators  $\varphi_k$  satisfying

$$\frac{d\varphi_k}{dt} = \sum_{p \in \mathbb{Z}} \omega_{k,p} \cos(\varphi_p + \varphi_{k-p} - \varphi_k), \quad |k| > k_0, \quad (\text{A.6})$$

with coefficients  $\omega_{k,p} = -k |p(k-p)|^{-\alpha} |k|^\alpha$  when  $|k-p|, |p| > k_0$  ( $\omega_{k,p} = 0$  otherwise), and with  $\varphi_{-k} = -\varphi_k$  (reality condition). Compared to equation (A.3), we have rescaled time in (A.6) to absorb the factor 1/2. The triadic interaction term couples the phases with wavenumbers  $k$ ,  $p$ , and  $k-p$ , via the so-called triad phase  $\varphi_{p,k-p}^k := \varphi_p + \varphi_{k-p} - \varphi_k$ . It is important to note that this phase-only model does not need an energy input/output mechanism, as constant energy is maintained by the constant amplitudes. Furthermore, it is formally fully time reversible under the symmetry  $t \rightarrow -t; \varphi_k \rightarrow \varphi_k + \pi$ . However, it will not come as a surprise that, like in a formally reversible version of the Navier-Stokes equations [185–188], the chaotic dynamics spontaneously break the time symmetry leading to a non-Gaussian and skewed velocity increment probability density function (PDF). To study the model numerically, we further

introduce a discretization with grid spacing  $\Delta x = \pi/N$ , effectively setting  $a_k = 0, |k| > N$ . The reality condition  $\varphi_{-k} = -\varphi_k$  leaves us with a set of phases evolving on modes  $k_0 < k \leq N$ . We set  $k_0 = 1$  so  $a_1 = a_{-1} = 0$  and thus the evolving variables are  $\varphi_2, \dots, \varphi_N$ . Note that the energy spectrum of the field is fixed and perfectly self-similar:  $E_k \sim a_k^2$ , with a power-law decay of  $E_k \propto k^{-2\alpha}$ . The observed original Burgers case, where quasi discontinuities (shocks) dominate the high-order statistics, corresponds to  $\alpha = 1$ .

### A.3 Numerical results on real-space and phase dynamics & statistics.

We integrate numerically (A.6) with a fourth-order Runge-Kutta method starting from uniformly random initial conditions. The nonlinear term can be written as a convolution, which we efficiently evaluate with a pseudospectral method. Figure A.1 illustrates the dynamics of our model, for the choice of steepness  $\alpha = 1$  (Burgers case), revealing insights into the relation between non-Gaussianity of the real-space statistics and Fourier phase synchronization. Panel (a) is a space-time plot of the velocity field from this minimal model, showing that shocks are the dominant structure. As time evolves, shocks steadily merge and separate. Occasionally, they merge into one dominating shock (horizontal blue line). Panel (b) shows a time series of the individual Fourier phases of the model. It shows that the presence of this dominating shock corresponds to highly ordered patterns in the phase plot. Away from these events, the system is dominated by smaller shocks and we observe a low coherence (gray line). To quantify this, panel (c) shows the time average phase synchronization (A.10), which reveals the synchronization of the oscillator system locally in time. The time of the highest synchronization corresponds to the dominating shock in real space. Panel (d) shows that the presence of the dominating shock (blue line) yield extreme events in the gradient field characterizing the small scales of the velocity field.

By changing the free parameter  $\alpha$  in (A.6) we control the multi-scale coupling among the phases and the hierarchical organization of typical time scales. In a *local* approximation, i.e. supposing the dynamics at wavenumber  $k$  is mainly driven by triads around the same wavenumber,  $|k| \sim |k-p| \sim |p|$ , we can estimate the scale-dependent eddy-turnover time as  $\tau_k \sim |k|^{\alpha-1}$ , indicating that, within this approximation, we reach a regime where small scales are faster than the large scales if  $\alpha < 1$  (and slower if  $\alpha > 1$ ). The local-triad approximation is expected to be valid in the range  $0.5 < \alpha < 1.5$  [189], where the Fourier transform connecting the spectrum and the two-point velocity correlation function does not diverge neither in the UV nor in the IR. As a result, we expect that in the above range and around  $\alpha = 1$  a non-trivial balancing between spatial and temporal fluctuations will set in.

In figure A.2 we indeed observe that our model has non-trivial scale- and steepness-dependent statistics. Here we show the probability distribution functions (PDF) of the velocity increments  $\delta_r u = u(x+r) - u(x)$  for two different scales,  $r = L := \pi$  and  $r = \eta := \pi/N$ , denoting the largest and smallest distances in the periodic domain, respectively. Real-space statistics are obtained by inserting the phase dynamics into (A.2). For completely uniform amplitudes (steepness  $\alpha = 0$ ) the phases evolve under an all-to-all coupling with equal strength. Note that this choice of spectral amplitudes corresponds to a delta-correlated field in real space. In this case, all phases become dynamically uniformly distributed and uncorrelated, leading to a Gaussian velocity field at all scales (panel (a) in figure A.2). In contrast, for steepness values

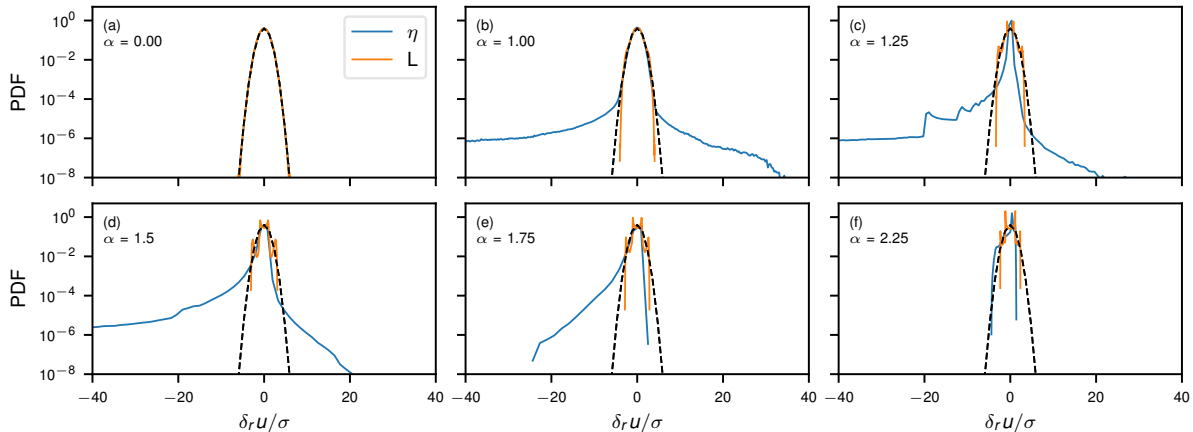


Figure A.2: (a)-(f): Standardized probability density distributions (PDFs) of  $\delta_r u$  calculated at the smallest,  $\eta$ , and largest increments,  $L$ . (a) For flat Fourier amplitudes  $\alpha = 0$  the velocity field is Gaussian across all scales. (b)-(e) Increasing  $\alpha$  leads to heavy tails at small scales. (f) For a steep enough spectrum the velocity field is dominated by the first few modes leading to PDFs without heavy tails. Data for  $N = 2^{15}$  and  $k_0 = 1$ .

within the range  $[0.5, 1.5]$ , where the local-triad approximation is expected to be valid, heavy tails are observed in the velocity increment PDF at small scales (panels (b)–(d) in figure A.2). For the smallest increment, the negative PDF tails are much heavier than the positive tails and both are much heavier than Gaussian. Heuristically (to be quantified later), this is the result of phase synchronization leading to shocks (anti-shocks), i.e. extreme negative (positive) gradients.

The presence of extreme events is maximal at  $\alpha \sim 1.25$ , as evidenced in figure A.2(c). For higher values of  $\alpha$  the PDF tails slowly regularize. In this limit, the large-scale modes dominate the real-space velocity field, leading to a dominant sinusoidal mode with superimposed smaller fluctuations. As a consequence, the large  $\alpha$  limit shows close-to-Gaussian statistics throughout.

To quantify the steepness-dependent departure of the small scales from Gaussianity we measure the skewness and flatness:

$$S(r) = \frac{\langle (\delta_r u)^3 \rangle}{\langle (\delta_r u)^2 \rangle^{3/2}}, \quad F(r) = \frac{\langle (\delta_r u)^4 \rangle}{\langle (\delta_r u)^2 \rangle^2}. \quad (\text{A.7})$$

Due to our frozen-amplitude condition the denominators of both quantities do not fluctuate. Figure A.3(a) shows a clear transition at  $\alpha \sim 1.0$ . The peaks of skewness and flatness at  $\alpha \sim 1.25$  correspond to the presence of extremely intense negative gradients seen in figure A.2(c).

As the steepness is increased further, the phases evolve under a non-local and non-trivial triad coupling. This gives rise to synchronization events, which underlie the steepness-dependent transition observed in the real-space statistics. Note, however, that when the steepness is too large the timescales from the triad coupling can get too separated, as the coefficients  $\omega_{k,p}$  in (A.6) become too small when  $|p|$  and  $|k-p|$  are large. Thus we expect to see synchronization over a finite range of steepness values only. In the next sections we will quantify the dependence on the  $\alpha$  parameter, of synchronization, and of the structure of the associated chaotic

attractors.

## A.4 Synchronization.

We quantify the behaviour of triad phases across a range of scales for (A.6) by defining the scale-dependent collective phase  $\theta_k$ :

$$e^{i\theta_k} = \frac{\sum_{p \in \mathbb{Z}} a_p a_{k-p} e^{i(\varphi_p + \varphi_{k-p} - \varphi_k)}}{\left| \sum_{p \in \mathbb{Z}} a_p a_{k-p} e^{i(\varphi_p + \varphi_{k-p} - \varphi_k)} \right|}. \quad (\text{A.8})$$

This collective phase is dynamically relevant as the RHS of (A.6) is proportional to  $\cos \theta_k$ . The fluctuations of  $\theta_k$  over time serve as a measure of the triad phase coherence across scales. Thus, averaging over a causal time window  $T$  from  $t - T$  to  $t$ , we get the following scale-dependent Kuramoto order parameter:

$$R_k^T(t) e^{i\Theta_k^T(t)} = \left\langle e^{i\theta_k(t)} \right\rangle_T \quad (\text{A.9})$$

As usual we have  $0 \leq R_k^T \leq 1$ , and phase synchronization is indicated by  $R_k^T$  values close to 1. Averaging additionally over the spatial scales, we define the average phase synchronization by

$$\mathcal{R}^T(\alpha, t) = \frac{1}{N - k_0} \sum_{k=k_0+1}^N R_k^T(t), \quad (\text{A.10})$$

which measures how the phase synchronization changes as a function of the spectral slope. As discussed earlier, we evaluated the time-dependent average phase synchronization  $\mathcal{R}^T$  in Fig. A.1(c) to establish the correspondence between real-space structures and phase synchronization. For very large  $T$ , we obtain the time and scale-averaged phase synchronization  $\mathcal{R}(\alpha) = \lim_{T \rightarrow \infty} \mathcal{R}^T(\alpha, t)$ .

Figure A.3(b) shows the average phase synchronization  $\mathcal{R}(\alpha)$  as a function of  $\alpha$  for various system sizes  $N$ . The relatively high synchronization seen for small  $N$  at  $\alpha > 2.0$  decreases as  $N$  is increased. This is due to the addition of faster and noisier oscillators to the system causing a convergence towards a pronounced peak for  $\alpha \in [1.0, 2.0]$ , indicating high phase synchronization for this interval for large  $N$ . The synchronization peak is remarkably coincidental with the flatness and skewness peaks shown in figure A.3(a), providing quantitative evidence in support of the relation between synchronization (a dynamical-system measure) and intermittency (a real-space measure).

## A.5 Chaos characterization.

As an additional characterization of the dynamical system, we estimate the properties of the underlying strange attractor as a function of  $\alpha$  and for  $N = 64, 128, 256, 512$  by examining the Lyapunov exponents (LEs) [190]. For reasons of numerical complexity we cannot reach the same resolution we used for the statistical characterization of intermittency and synchronization; however as we will see below the  $N = 512$  case shows strong indications of convergence to the large- $N$  limit.

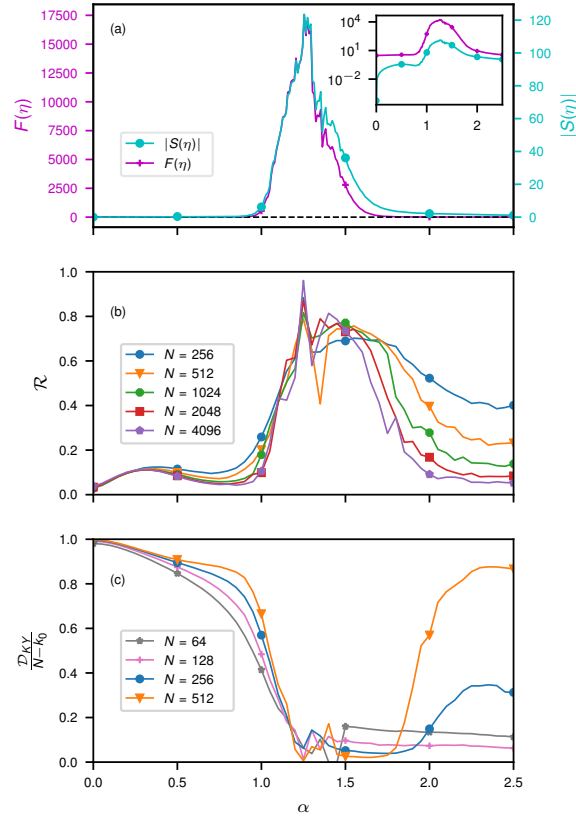


Figure A.3: (a): Absolute value of the skewness  $|S(\eta)|$  and the flatness  $F(\eta)$  for the smallest increment  $\eta$  as a function of  $\alpha$  (inset: same figure on log-lin scales,  $N = 2^{15}$ ). (b): the time and scale-averaged phase synchronization  $\mathcal{R}(\alpha)$  as a function of  $\alpha$  for various system sizes. (c): ratio between the Kaplan-Yorke dimension  $\mathcal{D}_{KY}$  and  $N - k_0$  as a function of  $\alpha$  for various system sizes.

Using the LEs we can calculate the dimension of the attractor via the Kaplan-Yorke (KY) approximation [191, 192]. Given the ordered LEs  $\lambda_1 \geq \lambda_2 \geq \dots \geq \lambda_{N-k_0}$ , the KY dimension is defined as

$$\mathcal{D}_{KY} = J + \frac{\sum_{j=1}^J \lambda_j}{|\lambda_{J+1}|}, \quad (\text{A.11})$$

where the conditions  $\sum_{j=1}^J \lambda_j \geq 0$  and  $\sum_{j=1}^{J+1} \lambda_j < 0$  define the index  $J$ . The KY dimension gives a measure of the systems' effective degrees of freedom. Figure A.3(c) shows a plot of the ratio between the  $\mathcal{D}_{KY}$  and the number of available degrees of freedom, as a function of  $\alpha$  and for several values of  $N$ . It is evident that as  $N$  grows a clear pattern emerges, whereby  $\mathcal{D}_{KY}$  greatly diminishes for values of  $\alpha$  inside the interval  $[1.0, 2.0]$ , a behaviour that coincides, on the one hand, with the departure from Gaussianity observed in figure A.3(a), and on the other hand, with the increase in phase synchronization shown in figure A.3(b).

## A.6 Conclusions.

Our minimal model sheds light into the nature of coherent structures as low-dimensional objects, establishing a dynamical scenario where real-space intermittency and phase synchronization are accompanied by a reduction in the dimensions of the attractor. In our model coherent structures are controlled by Fourier phase dynamics only, as the energy spectrum is static and plays a background role. Our results open new perspectives concerning the possibility to connect turbulence intermittency with dynamical system tools based on phase synchronization and chimera states [193].

On the quantitative side, our results provide insight into the solution to the full inviscid Burgers equation, where all amplitudes are allowed to evolve. There, for generic initial conditions, a finite-time singularity develops characterized by phase synchronization and a power-law spectrum with steepness  $1.33 \leq \alpha \leq 1.50$  [194, 195]. We have checked that this behaviour is robust, occurring even under the constraint  $a_{k_0} = 0$  for  $k_0 = 1$ . Because in the full equations the spectrum evolves slowly, it is natural to expect that in our frozen-spectrum constrained model the phases must show high correlation in the same range of imposed slopes.

A natural extension of this work would be an investigation of the phase-only 3D Navier-Stokes dynamics by fixing the amplitudes of all Fourier modes, including comparisons to Navier-Stokes equations with a fixed spectrum, either for all wavenumbers or for a subset of them [164, 165]. Results in this direction would help to shed additional light on the origin of extreme events and small-scale intermittency.

Acknowledgment. This work received funding from the European Research Council (ERC) under the European Union's Horizon 2020 research and innovation programme (grant agreement No 882340). JAAL and MW were supported by the Max Planck Society. EC and MDB were supported by the Irish Research Council under grant number GOIPG/2018/2653.

## Manuscript IV

In this second part of the appendix we present a manuscript which originally appeared as "Pujara, N., **Arguedas-Leiva, J.-A.**, Lalescu, C.C., Bramas, B. and Wilczek, M. (2021). [Shape- and scale-dependent coupling between spheroids and velocity gradients in turbulence.](#) *Journal of Fluid Mechanics*, 922 (R6)" and is licensed under the [Creative Commons Attribution 4.0 licence \(CC BY 4.0\)](#).

N. P., C.C. L., and M. W. designed the study, analyzed data and reached conclusions. N. P., J.-A. A.-L., C.C. L., and B. B. wrote the code and J.-A. A.-L., C.C. L., and B. B. executed it. N. P. and M. W. derived the theory. N. P., J.-A. A.-L., C.C. L., and M. W. wrote the paper.

# Shape- and scale-dependent coupling between spheroids and velocity gradients in turbulence

Nimish Pujara,<sup>1†</sup> José-Agustín Arguedas-Leiva,<sup>2</sup>  
Cristian C. Lalescu,<sup>2,3</sup> Béranger Bramas,<sup>3,4</sup> Michael Wilczek<sup>2</sup>

<sup>1</sup>Department of Civil and Environmental Engineering,  
University of Wisconsin-Madison, WI 53706, USA

<sup>2</sup>Max Planck Institute for Dynamics and Self-Organization (MPI DS),  
Am Faßberg 17, D-37077 Göttingen, Germany

<sup>3</sup>Max Planck Computing and Data Facility, Gießenbachstraße 2, 85748, Garching, Germany

<sup>4</sup>Inria Nancy – Grand-Est, CAMUS Team, France

<sup>†</sup>To whom correspondence should be addressed; E-mail: npujara@wisc.edu .

## Abstract

Rotations of spheroidal particles immersed in turbulent flows reflect the combined effects of fluid strain and vorticity, as well as the time history of these quantities along the particle’s trajectory. Conversely, particle rotation statistics in turbulence provide a way to characterise the Lagrangian properties of velocity gradients. Particle rotations are also important for a range of environmental and industrial processes where particles of various shapes and sizes are immersed in a turbulent flow. In this study, we investigate the rotations of inertialess spheroidal particles that follow Lagrangian fluid trajectories. We perform direct numerical simulations of homogeneous isotropic turbulence and investigate the dynamics of different particle shapes at different scales in turbulence using a filtering approach. We find that the mean-square particle angular velocity is nearly independent of particle shape across all scales from the Kolmogorov scale to the integral scale. The particle shape does determine the relative split between different modes of rotation (spinning vs. tumbling), but this split is also almost independent of the filter scale suggesting a Lagrangian scale-invariance in velocity gradients. We show how the split between spinning and tumbling can be quantitatively related to the particle’s alignment with respect to the fluid vorticity.

## B.1 Introduction

In the Lagrangian study of turbulence, a point-sized sphere is used to probe the flow since such a particle adopts the velocity and angular velocity of the fluid in its immediate vicinity. Extending this idea to spheroids (figure B.1) offers a more intricate way to examine the Lagrangian flow structure since spheroids rotate due to both fluid rotation and strain, and

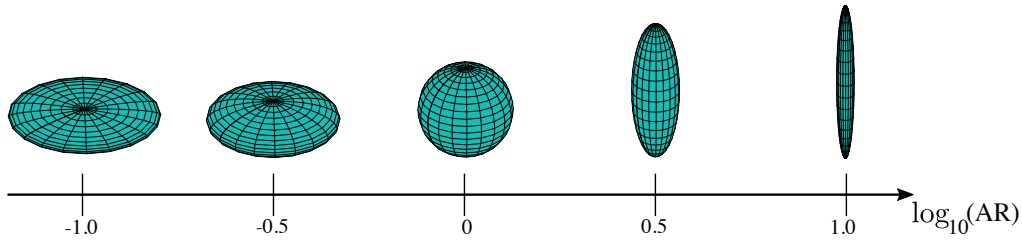


Figure B.1: Spheroids as a function of aspect ratio, AR.

thus the statistics of spheroid rotations reflect the Lagrangian dynamics of velocity gradients [51]. Rotations of spheroidal particles and their coupling with velocity gradients are also important in applications where non-spherical particles are immersed in turbulent flows, such as microswimmers [23, 63, 72, 82, 196], atmospheric aerosol and sediment transport [25, 197–202], process engineering [203–208], and flow diagnostics [209–211].

In this study, we examine how spheroids of different shapes rotate due to their coupling with velocity gradients at different scales in homogeneous and isotropic turbulence. The angular velocity of a spheroid due to local velocity gradients in the absence of inertia is given by Jeffery’s (1922) equation:

$$\boldsymbol{\omega}_p = \frac{1}{2}\boldsymbol{\omega} + \lambda\mathbf{p} \times \mathbf{S}\mathbf{p}, \quad (\text{B.1})$$

where  $\boldsymbol{\omega}_p$  is the particle angular velocity vector,  $\mathbf{p}$  is the particle orientation vector, and  $\lambda = (\text{AR}^2 - 1)/(\text{AR}^2 + 1)$  is the shape factor with AR being the particle aspect ratio (figure B.1). The velocity gradients are represented by the fluid vorticity vector  $\boldsymbol{\omega}$  and the strain rate tensor  $\mathbf{S}$ , which relate to the velocity gradient tensor  $A_{ij} = \partial u_i / \partial x_j$  via  $S_{ij} = \frac{1}{2}(A_{ij} + A_{ji})$  and  $\omega_i = \varepsilon_{ijk}A_{kj}$  with  $\varepsilon_{ijk}$  being the alternating symbol. The first term of Eq. (B.1) shows that particles of all aspect ratios rotate at the local rotation rate of the fluid and the second term shows that non-spherical particles have additional rotation due to the local strain rate. Decomposing Eq. (B.1) into its spinning ( $\boldsymbol{\omega}_p \cdot \mathbf{p}$ ) and tumbling ( $d\mathbf{p}/dt = \dot{\mathbf{p}} = \boldsymbol{\omega}_p \times \mathbf{p}$ ) rates gives

$$\boldsymbol{\omega}_p \cdot \mathbf{p} = \frac{1}{2}\boldsymbol{\omega} \cdot \mathbf{p} \quad (\text{B.2})$$

$$\dot{\mathbf{p}} = \frac{1}{2}\boldsymbol{\omega} \times \mathbf{p} + \lambda [\mathbf{S}\mathbf{p} - (\mathbf{p}^T \mathbf{S}\mathbf{p})\mathbf{p}], \quad (\text{B.3})$$

where spinning is the particle rotation about its axis of symmetry and tumbling is the particle rotation of the axis of symmetry. Spinning and tumbling are related to the total particle angular velocity via the Pythagorean relation  $\boldsymbol{\omega}_p^2 = (\boldsymbol{\omega}_p \cdot \mathbf{p})^2 + \dot{\mathbf{p}}^2$ .

When spheroids follow Lagrangian fluid trajectories and rotate in response to the velocity gradients along those trajectories, the mean-square spinning ( $\langle (\boldsymbol{\omega}_p \cdot \mathbf{p})^2 \rangle$ ) and tumbling ( $\langle \dot{\mathbf{p}}^2 \rangle$ ) rates reflect the distribution of particle orientations with respect to principal directions of the velocity gradients. Eq. (B.3) shows that the particle tumbling rate for a given shape in isotropic turbulence is a joint distribution in a seven-dimensional space [97]: 5 scalar parameters characterise the velocity gradient tensor in isotropic turbulence (*e.g.*, 2 to quantify the eigenvalues of the strain rate tensor, 2 to specify the orientation of vorticity in the strain rate eigenframe, and 1 to quantify the magnitude of vorticity) and an additional 2 parameters describe the particle orientation with respect to the velocity gradient tensor (*e.g.*, 2 angles relative to the strain rate eigenframe). Thus, the spinning and tumbling rates depend on the history of vorticity and strain along Lagrangian trajectories. Being able to predict these rotation rates is useful for the applications mentioned above and for benchmarking stochastic

models of the velocity gradient tensor; for example, Chevillard and Meneveau [74] showed that a model based on the recent fluid deformation approximation was able to correctly predict the tumbling of rods and Leppin and Wilczek [212] showed that inclusion of strain-vorticity interactions and shorter autocorrelation timescales for the strain rate compared to the rotation rate were crucial for predicting the tumbling of discs.

Spinning and tumbling rates can be predicted analytically for particles randomly oriented with respect to the velocity gradient tensor, but results from experiments and direct numerical simulations have shown that this does not provide an accurate prediction of particle rotation rates in turbulence [74, 76, 77, 94, 99]. For example, tumbling of small rods ( $AR \gg 1$ ) and spinning of small discs ( $AR \ll 1$ ) are suppressed relative to their values for random orientation. Qualitatively, this is understood to be because rods align with the vorticity causing them to spin more than they tumble and discs align perpendicularly to the vorticity causing them to tumble more than they spin [73, 75, 94]. While this picture suggests that alignment with vorticity controls the dynamics of particle rotations, a quantitative understanding of this behaviour has not been found. For example, conditional averages of the seven-dimensional joint distribution showed that rod tumbling was equally strongly dependent on both the mean-square vorticity and strain rate and the problem could not be further simplified via a lower-dimensional projection [97]. Here, we present a line of argument that allows us to quantitatively predict the spinning and tumbling rates of spheroids in isotropic turbulence based on their alignment with vorticity. We test this prediction against data from direct numerical simulations and find good agreement.

Since spheroid rotation statistics reveal Lagrangian dynamics of velocity gradients, an understanding of the scale dependency of these statistics can contribute to improving models of the turbulent energy cascade [213–216], sub-grid-scale models for large-eddy simulations (LES) [217, 218], and models of particle motion [219–221]. As a way to characterize multi-scale properties of Lagrangian turbulence, we investigate the scale-dependency in our simulations using a filtering approach where particle rotations are tracked along Lagrangian trajectories in turbulent velocity fields filtered at various scales. This allows for velocity gradients to be tracked along trajectories for times greater than the integral time scale. Our results show that particle rotation statistics are remarkably scale-independent when normalised appropriately and we are able to predict the spinning and tumbling rates for different shapes from the dissipation scales to the integral scale. We interpret this as a sign of fairly robust scale invariance for velocity gradients across the full scale spectrum of turbulence when examined in the Lagrangian frame.

## B.2 Direct numerical simulations

### B.2.1 Velocity gradients along Lagrangian trajectories

We use direct numerical simulations (DNS) of isotropic turbulence to generate data of velocity gradient time histories along Lagrangian trajectories. We do this in the fully resolved flow field and for the flow field filtered at various length scales.

The DNS are performed with a standard pseudo-spectral Navier-Stokes solver. A third-order Runge-Kutta method is used for time stepping the vorticity formulation of the equation, and a high-order Fourier smoothing [222] is used for reducing aliasing errors. Turbulence is maintained in a 3D-periodic domain of  $2\pi \times 2\pi \times 2\pi$  (DNS units) by applying a fixed energy injection rate in the wavenumber interval  $1 \leq k \leq 2$  (DNS units). We use a small-scale resolution of  $k_M \eta = 3$  (where  $k_M$  is the maximum wavenumber resolved, and  $\eta$  is the

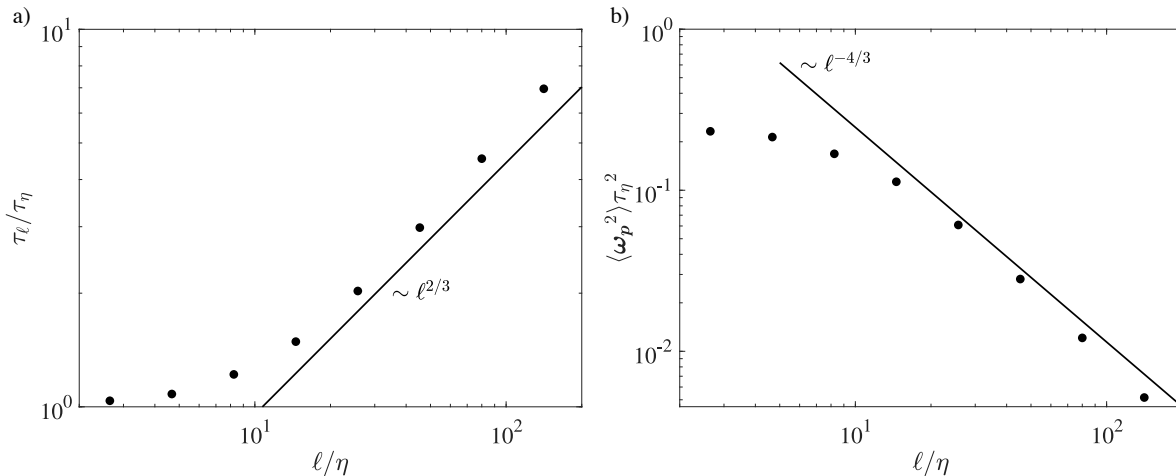


Figure B.2: Variation of (a) scale-local timescale  $\tau_\ell = \langle A_{ij} A_{ij} \rangle^{-1/2}$  and (b) mean-square particle angular velocity  $\langle \omega_p^2 \rangle$  as functions of filter scale  $\ell$ . Data in (b) is for spherical particles.

Kolmogorov length), for a fully developed turbulent flow with a Taylor-scale Reynolds number  $R_\lambda \approx 200$  and a scale separation of  $L/\eta \approx 140$  and  $T/\tau_\eta \approx 20$ . Using the root-mean-squared velocity component  $u$ , the integral length is defined as  $L = \pi \int dk E(k)/(2ku^2)$  and the large eddy turn-over time as  $T = L/u$ . To generate filtered flow fields, the velocity field is filtered at length scale  $\ell$  using a Gaussian filter as detailed in [223]. Values for  $\ell$  vary from zero (no filtering) to  $L$  (the integral scale). Preliminary datasets were generated using all three spherically symmetric filter types described in [223] (*i.e.*, ball filter, Gaussian filter, sharp spectral filter), but the filter type resulted in only small changes in the results with the overall trend being insensitive to the precise filter type.

At each filter scale  $\ell$ ,  $10^4$  tracer trajectories are integrated in the flow using the corresponding velocity fields and the velocity gradient tensor is sampled along these trajectories to generate a large database of Lagrangian time histories of velocity gradients along tracer trajectories.

To analyse particle rotations across different filter scales, we introduce a scale-local time scale defined by  $\tau_\ell = \langle A_{ij} A_{ij} \rangle^{-1/2}$ , which varies smoothly from  $\tau_\eta$  for the fully resolved flow to the expected Kolmogorov scaling  $\tau_\ell \sim \ell^{2/3}$  in the inertial subrange (figure B.2a).  $\tau_\ell$  is a quantitative measure of the correlation time and the inverse strength of the velocity gradients at scale  $\ell$ , making it ideally suited to compare particle rotations across a range of scales.

### B.2.2 Scale-dependency in particle rotation statistics

We use the database of Lagrangian time histories of velocity gradients to compute the orientations and rotations of spheroids by integrating Jeffery's (1922) equations (B.3) using a fourth-order Runge-Kutta method. After an initial transient of several  $\tau_\ell$ , the statistics of particle rotations reach a stationary state. We calculate the statistical moments of particle rotations after this initial transient period.

Figure B.2b shows that data for mean-square particle angular velocity follows a power law scaling in the inertial subrange  $\langle \omega_p^2 \rangle \sim \ell^{-4/3}$ . This scaling behaviour, which was first introduced in the context of tumbling rods by Parsa and Voth [221] and found to be applicable in several other contexts since then [23, 93, 224–226], can be derived based on the expectation

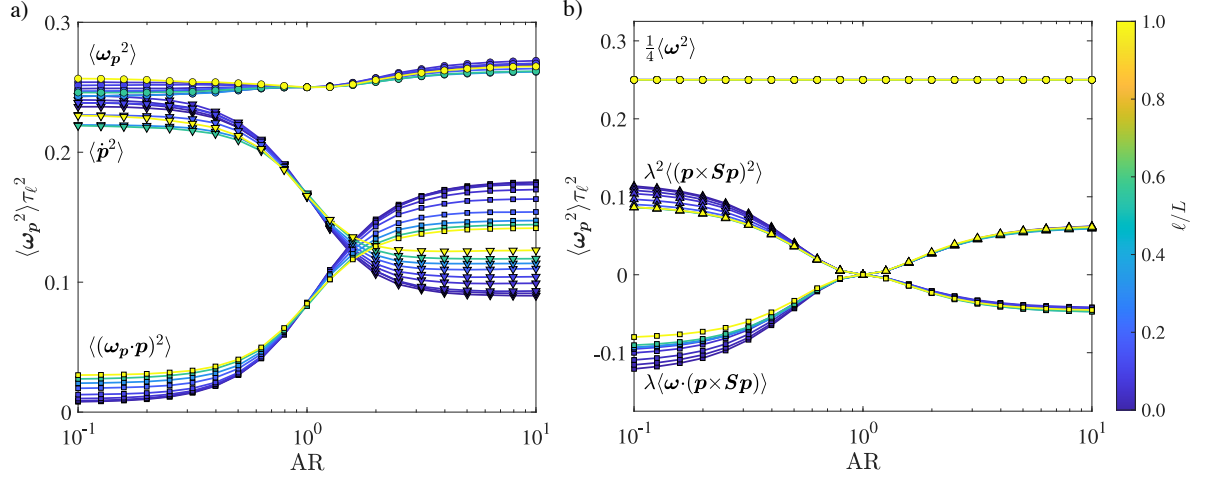


Figure B.3: a) Mean-square particle angular velocity and its decomposition into spinning and tumbling for spheroids of different aspect ratios in turbulence filtered at different length scales. b) Mean-square particle angular velocity and its decomposition into vorticity-induced rotations ( $\frac{1}{4}\langle\omega^2\rangle$ ), strain-induced rotations ( $\lambda^2\langle(\mathbf{p}\times\mathbf{S}\mathbf{p})^2\rangle$ ), and the cross-correlation of vorticity- and strain-induced rotations ( $\lambda\langle\omega\cdot(\mathbf{p}\times\mathbf{S}\mathbf{p})\rangle$ ).

that the particle rotation rate scales as the magnitude of the velocity gradients at a given scale  $\omega_p \sim \tau_\ell^{-1} = \langle A_{ij}A_{ij} \rangle^{1/2}$  and that the magnitude of the velocity gradients follow Kolmogorov scaling in the inertial range  $A_{ij} \sim \ell^{-2/3}$ .

When the mean-square particle angular velocity is examined in terms of the scale-local time scale  $\tau_\ell$  in figure B.3a, we observe that the mean-square rotation rate for particles for all scales is almost shape-independent. Particles of all shapes have approximately the same rotation rate as spheres (or spherical fluid elements) at all scales of turbulence so that  $\langle\omega_p^2\rangle \approx \frac{1}{4}\langle\omega^2\rangle$ . Surprisingly, figure B.3a also shows that the relationship between particle shape and their spinning and tumbling rates is qualitatively preserved as the filter scale increases, even up to the integral scale. Discs tumble much more than they spin and rods spin more than they tumble at all scales of turbulence. As filter scale increases, there is a shift towards the spinning and tumbling rates becoming weaker functions of particle shape, but the main qualitative trend is preserved. Overall, the results in figure B.3a, which are normalised by the scale-local time scale  $\tau_\ell$ , reflect an unexpected scale-invariance in the Lagrangian dynamics of velocity gradients.

To further examine the shape-independence of the mean-square particle angular velocity  $\langle\omega_p^2\rangle$ , we take the mean square of Eq. (B.1) to analyse the situation in terms of rotations due to vorticity and strain. This shows that the mean-square particle angular velocity has contributions from vorticity, strain, and a combination of vorticity and strain:

$$\langle\omega_p^2\rangle = \frac{1}{4}\langle\omega^2\rangle + \lambda^2\langle(\mathbf{p}\times\mathbf{S}\mathbf{p})^2\rangle + \lambda\langle\omega\cdot(\mathbf{p}\times\mathbf{S}\mathbf{p})\rangle. \quad (\text{B.4})$$

The particle shape only influences the second and third terms, which contain the strain rate tensor. Figure B.3b shows the particle rotation rates split into the three terms in Eq. (B.4). While the vorticity term is shape-independent and the strain term is always positive as expected, the cross term is almost exactly equal and opposite to the strain term. This near cancellation is the reason why  $\langle\omega_p^2\rangle$  is nearly independent of particle shape at all scales in

turbulence. We note that this behaviour is specific to Lagrangian trajectories and the mutual interactions between vorticity and strain-rate along these trajectories. The rotations of particles distributed at random positions and orientations within a snapshot of a turbulent velocity field do not show the same behaviour [as previously shown in 74, 76, 77]. While this property of vorticity-strain interactions in the Lagrangian dynamics of velocity gradients was previously noted for point-sized particles [77, 94], the results in figure B.3b show that this behaviour is scale-invariant.

### B.2.3 Particle spinning and tumbling

In this section, we show how the particle spinning and tumbling rates observed in figure B.3a can be quantitatively predicted in terms of particle alignment with vorticity. Starting from Eq. (B.4), we note that an (approximate) cancellation of the last two terms on the right-side leads to  $\langle \omega_p^2 \rangle \approx \frac{1}{4} \langle \omega^2 \rangle$ . In homogeneous isotropic turbulence, the mean-square fluid vorticity and the mean dissipation rate are related via  $\langle \omega^2 \rangle = 2 \langle S_{ij} S_{ij} \rangle = \tau_\eta^{-2}$ , where  $\tau_\eta$  is the Kolmogorov timescale that characterises the smallest scales of motion. In terms of  $\tau_\eta$ , the mean-square particle rotation rate would be

$$\langle \omega_p^2 \rangle \approx \frac{1}{4} \tau_\eta^{-2}. \quad (\text{B.5})$$

To predict the spinning and tumbling rates of particles, we next consider the spinning equation. By taking the mean-square of Eq. (B.2), we get

$$\langle (\omega_p \cdot p)^2 \rangle = \frac{1}{4} \langle \omega^2 (e_\omega \cdot p)^2 \rangle \approx \frac{1}{4} \langle \omega^2 \rangle \langle (e_\omega \cdot p)^2 \rangle = \frac{1}{4} \tau_\eta^{-2} \langle (e_\omega \cdot p)^2 \rangle, \quad (\text{B.6})$$

where we have assumed that the magnitude of vorticity and the degree of alignment between the particle and the vorticity are statistically independent. Under this assumption, Eq. (B.6) gives a prediction for the mean-square spinning rate solely based on particle alignment with vorticity. We can also obtain a prediction for the tumbling rate in terms of the particle alignment with vorticity by combining Eq. (B.6) with Eq. (B.5) and using the Pythagorean relation  $\langle \omega_p^2 \rangle = \langle (\omega_p \cdot p)^2 \rangle + \langle \dot{p}^2 \rangle$ :

$$\langle \dot{p}^2 \rangle \approx \frac{1}{4} \langle \omega^2 \rangle (1 - \langle (e_\omega \cdot p)^2 \rangle) = \frac{1}{4} \tau_\eta^{-2} \langle (1 - \langle (e_\omega \cdot p)^2 \rangle) \rangle. \quad (\text{B.7})$$

Altogether, we have predictions of the particle rotation, tumbling, and spinning rates solely in terms of the particle alignment with vorticity:

$$\langle \omega_p^2 \rangle \tau_\eta^2 \approx \frac{1}{4} \quad (\text{B.8})$$

$$\langle \dot{p}^2 \rangle \tau_\eta^2 \approx \frac{1}{4} (1 - \langle (e_\omega \cdot p)^2 \rangle) \quad (\text{B.9})$$

$$\langle (\omega_p \cdot p)^2 \rangle \tau_\eta^2 \approx \frac{1}{4} \langle (e_\omega \cdot p)^2 \rangle. \quad (\text{B.10})$$

We can now examine the predictions of Eqs. (B.8) using data from our simulations. By replacing  $\tau_\eta$  with  $\tau_\ell$ , we can also extend these predictions to all scales of turbulence. Since these predictions are based on the mean-square particle alignment with vorticity, we first show this quantity in figure B.4. We see that while discs tend to be perpendicular to the vorticity and rods tend to be parallel to the vorticity, particles of all shapes become more randomly aligned with respect to vorticity as the filter scale increases. Particle alignment with vorticity can be understood as the longest particle axis and the vorticity vector both independently

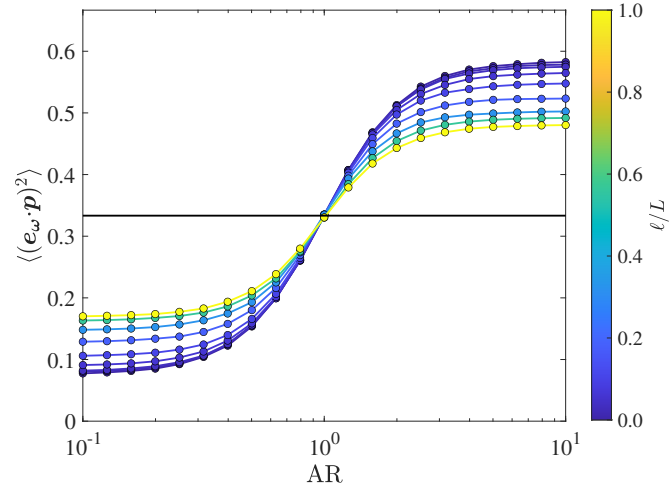


Figure B.4: Mean-square particle alignment with vorticity as a function of particle shape and filter scale. Random alignment corresponds to a value of  $1/3$  (solid black line).

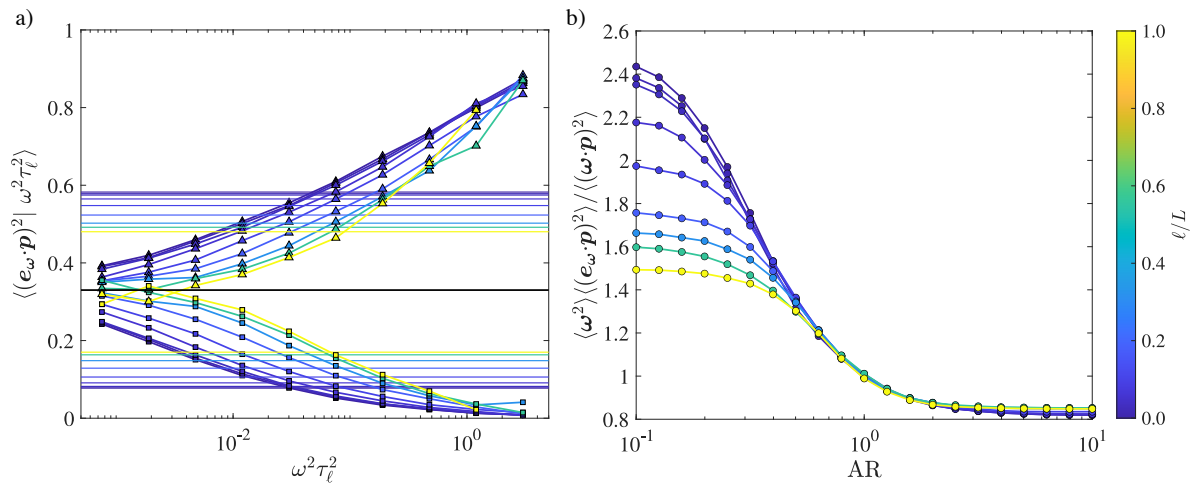


Figure B.5: a) Mean-square particle alignment with vorticity conditioned on the mean-square fluid vorticity. Symbols are data for high-aspect-ratio rods ( $AR = 10^1$ ; triangles and top lines) and discs ( $AR = 10^{-1}$ ; squares and bottom lines). Thin horizontal lines correspond to the unconditional mean-square particle alignment with vorticity  $\langle (\mathbf{e}_\omega \cdot \mathbf{p})^2 \rangle$ . Random alignment corresponds to a value of  $1/3$  (solid black line). b) A direct evaluation of the independence between vorticity magnitude and particle alignment assumed in Eq. (B.6).

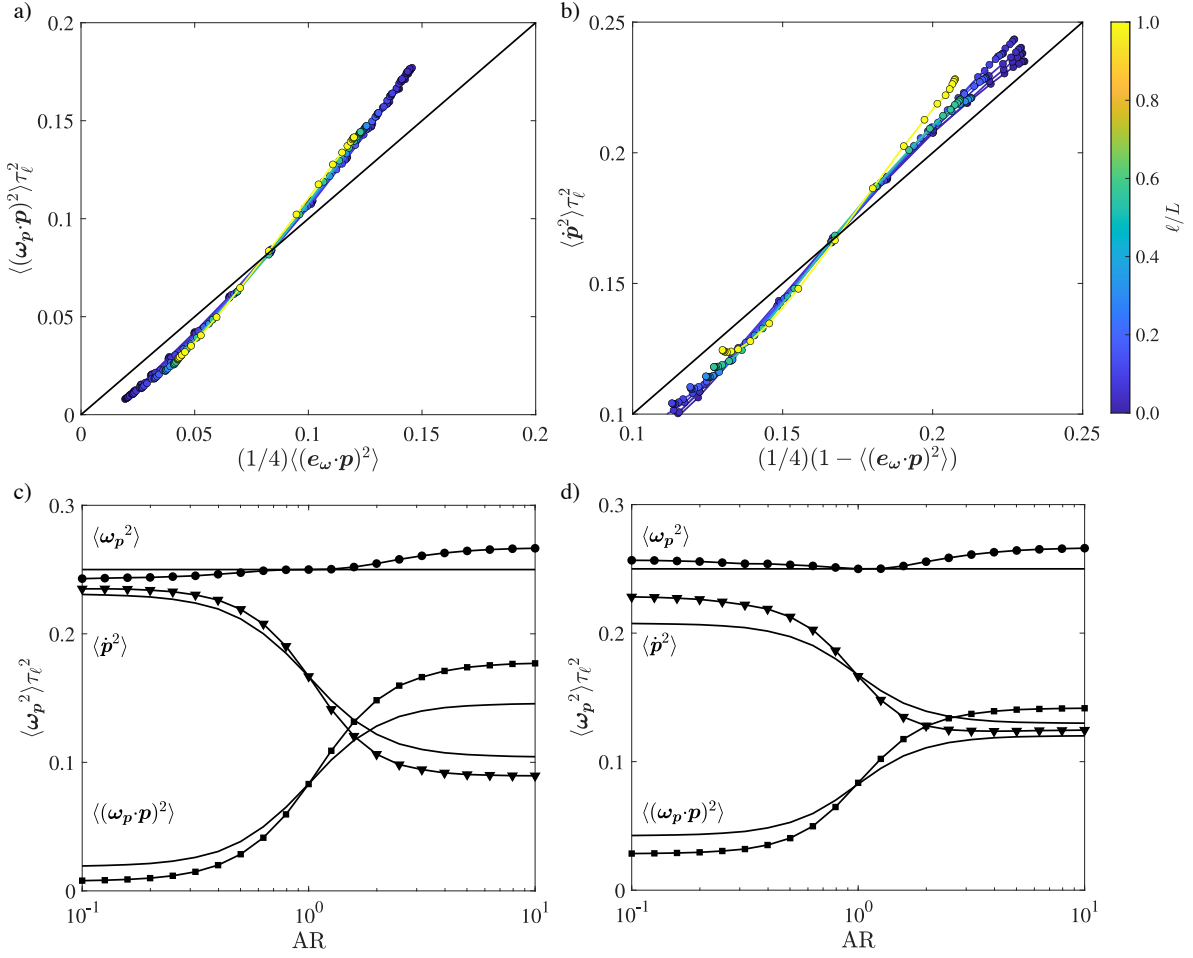


Figure B.6: Panels (a) and (b) compare the spinning (a) and tumbling (b) rates against the predictions from Eq. (B.8) for all shapes across all scales with the solid black line showing the 1:1 correspondence. Panels (c) and (d) compare predictions from Eq. (B.8) (solid black lines) to data (symbols) across all shapes for unfiltered DNS data ( $\ell/L = 0$ ) (c) and DNS data filtered at the integral scale ( $\ell/L = 1$ ) (d).

coming to align with the direction of Lagrangian stretching [75]. The data in figure B.4 show that this effect weakens with increasing filter scale due to the effects of sub-filter-scale motions on the velocity gradient dynamics [214, 226].

Next, we examine the assumption made in deriving Eqs. (B.8), namely that particle alignment with vorticity is independent of the vorticity magnitude. Figure B.5a shows the particle-vorticity alignment conditioned on the square of the vorticity magnitude for high-aspect-ratio rods and discs. We see that particle alignment with vorticity is stronger as the vorticity magnitude is increases, which likely reflects a recent history of Lagrangian stretching, but this variation does not stray too far from the overall mean-square alignment (shown by the thin horizontal coloured lines in figure B.5). Examined in this way, our assumption is only partially supported by the data. However, in figure B.5b, we show a more direct evaluation of the assumption made in Eq. (B.6), namely that particle spinning can be related to particle alignment with vorticity via the relation  $\langle(\omega \cdot p)^2\rangle \approx \langle\omega^2\rangle\langle(e_\omega \cdot p)^2\rangle$ . The data show that

this assumption has a less than 20% error for moderately oblate to extremely prolate particles with aspect ratios in the range  $10^{-0.6} \leq \text{AR} \leq 10^1$ . It is interesting that for prolate particles, the mean-square particle spinning can be accurately estimated by assuming independence between vorticity magnitude and particle alignment with vorticity and that the error in this approximation is independent of filter scale. For extremely oblate particles ( $\text{AR} \leq 10^{-0.6}$ ), the error in this approximation can be large and depends on the filter scale.

Finally, we show how the predictions of Eqs. (B.8) compare against data in figure B.6. The data lie close to the 1-to-1 lines against predictions (figures B.6a and B.6b), regardless of the filter scale and particle aspect ratio. Thus, Eqs. (B.8) provide reasonable predictions of spinning and tumbling rates, despite invoking the approximation that particle alignment is independent of the strength of local vorticity. The error induced by this approximation does not greatly affect the quality of predictions from Eqs. (B.8) because the error is either small in relative terms (prolate and moderately oblate particles) or because even when the error is large in relative terms it only leads to a small error in absolute terms (highly oblate particles). For highly oblate particles, the prediction of particle spinning has a large error error, but small absolute error because such particles rarely spin. In fact, while the relative error is larger for oblate particles compared to prolate particles in figure B.5b, the absolute error is actually slightly smaller for the oblate particles compared to prolate particles in figures B.6a and B.6b. In figures B.6c and B.6d, we can see that these predictions fare well against data for different particle shapes for fully resolved data ( $\ell/L = 0$ ) and for data at the largest filter scale ( $\ell/L = 1$ ), respectively.

### B.3 Discussion

We have conducted direct numerical simulations to examine the statistics of the shape- and scale-dependent coupling between velocity gradients and spheroids in turbulence. By applying a filter that progressively removes small scales from the fully resolved simulations, we have obtained Lagrangian trajectories of tracer particles in filtered fields and calculated spheroid rotations along these trajectories using Jeffery's equation. Our focus has been on the particle rotation rates and on the decomposition of rotations in the particle frame into the spinning and tumbling rates.

Particle rotation rates decrease as the filter scale increases following a power law that is consistent with Kolmogorov scaling in the inertial subrange. When normalised by scale-local time scales, we find that the mean-square particle rotation rates are independent of the particle shape. Even though the spinning and tumbling rates are a function of particle shape, surprisingly, there is little additional dependency on scale. Moreover, we have also shown that relative rates of spinning and tumbling can be reasonably predicted solely from knowledge of particle alignment with the vorticity vector even though the full dependency of these rotation rates is a function of seven variables that quantify the velocity gradient tensor and particle orientation within its axes.

Our results consistently show that the dynamics of the velocity gradient tensor has scale invariant properties in the Lagrangian frame that are not observed in the Eulerian frame. While Eulerian statistics of vorticity alignment with the strain eigenframe and flow topologies are known to exhibit qualitative differences in the inertial range relative to the dissipation (viscous) range [218, 227, 228], no such changes are observed as a function of scale when velocity gradient dynamics are examined in the Lagrangian frame through the lens of coupling

between velocity gradients and spheroids. Our results also suggest that spinning and tumbling rates of large anisotropic particles where particle inertia due to density differences with the fluid can be assumed small [*e.g.*, 221, 224, 226] are likely to follow the same trends with particle shape previously observed in small particles [51]. While information of the detailed flow-particle interactions may still require laboratory experiments or particle-resolved simulations, our results show that it is possible to predict rotation statistics for sub-grid-scale particles in large-eddy simulations (LES) in principle. For example, particle orientations and rotations at the smallest scale resolved in the simulations could be used to predict particle statistics at sub-grid-scales based on the scaling arguments provided herein. The scale-invariance of spinning and tumbling rates of spheroids also motivate future work on extending stochastic models of the Lagrangian velocity gradient tensor [74, 212, 229, 230] to the inertial range. Finally, it would also be interesting to test our predictive framework for particle spinning and tumbling in other canonical turbulent flows like channel flow where interesting similarities and differences have been observed in terms of how particles align compared to isotropic turbulence [231].

**Acknowledgements** We thank Markus Rampp (Max Planck Computing and Data Facility) for support with code optimisation, Greg Voth (Wesleyan University) for useful discussions, and Evan Variano (UC Berkeley) for useful discussions and help with creating the graphical abstract image. We also acknowledge comments and suggestions from anonymous referees.

**Funding** N.P. was supported by the Wisconsin Alumni Research Foundation. J.A.A.L., C.C.L., B.B., and M.W. were supported by the Max Planck Society. M.W. also gratefully acknowledges a Fulbright-Cottrell Award grant.

**Declaration of interests** The authors report no conflict of interest.

**Author ORCID** N. Pujara, <https://orcid.org/0000-0002-0274-4527>; J. A. Arguedas Leiva, <https://orcid.org/0000-0002-2786-2538>; C. C. Lalescu, <https://orcid.org/0000-0003-0043-6632>; Bérenger Bramas, <https://orcid.org/0000-0003-0281-9709>; M. Wilczek, <https://orcid.org/0000-0002-1423-8285>.

---

## Backmatter

---

# Bibliography

- [1] Paul R Pinet. *Invitation to oceanography*. Jones & Bartlett Learning, 2019.
- [2] Paul G Falkowski. [Ocean science: the power of plankton](#). *Nature*, 483(7387):S17–S20, 2012. doi: 10.1038/483S17a.
- [3] P. G. Falkowski. [The role of phytoplankton photosynthesis in global biogeochemical cycles](#). *Photosynth. Res.*, 39(3):235–258, 1994. doi: 10.1007/BF00014586.
- [4] Deborah K. Steinberg and Michael R. Landry. [Zooplankton and the Ocean Carbon Cycle](#). *Ann Rev Mar Sci*, 9(1):413–444, 2017. doi: 10.1146/annurev-marine-010814-015924.
- [5] Annegret Stuhr / GEOMAR. [Marine microplankton and mesoplankton](#), 2021. URL <https://www.geomar.de/entdecken/bilder-des-monats/bild-des-monats/bild-des-monats-september-2021>. [Online; accessed March 07, 2022].
- [6] Jennifer C. Prairie, Kelly R. Sutherland, Kerry J. Nickols, and Amanda M. Kaltenberg. [Biophysical interactions in the plankton: A cross-scale review](#). *Limnol. Oceanogr.*, 2(1): 121–145, 2012. doi: 10.1215/21573689-1964713.
- [7] U.S. JGOFS. [Biological pump](#). Image in Brochure, 2001. URL [http://usjgofs.whoi.edu/general\\_info/gallery\\_modeling/slide4.html](http://usjgofs.whoi.edu/general_info/gallery_modeling/slide4.html).
- [8] Stephen J. Giovannoni and Kevin L. Vergin. [Seasonality in Ocean Microbial Communities](#). *Science*, 335(6069):671–676, 2012. doi: 10.1126/science.1198078.
- [9] Nancy N. Rabalais, R. Eugene Turner, and William J. Wiseman. [Gulf of Mexico Hypoxia, A.K.A. “The Dead Zone”](#). *Annu Rev Ecol Evol Syst*, 33(1):235–263, 2002. doi: 10.1146/annurev.ecolsys.33.010802.150513.
- [10] Jesse Allen and Robert Simmon. [Algae bloom in Lake Erie](#), 2011. URL [https://commons.wikimedia.org/wiki/File:Toxic\\_Algae\\_Bloom\\_in\\_Lake\\_Erie.jpg](https://commons.wikimedia.org/wiki/File:Toxic_Algae_Bloom_in_Lake_Erie.jpg). [Online; accessed March 07, 2022].
- [11] Jacques Desclotres. [Coccolithophore bloom off Brittany, France](#), 2006. URL [https://commons.wikimedia.org/wiki/File:Algal\\_bloom\\_20040615.jpg](https://commons.wikimedia.org/wiki/File:Algal_bloom_20040615.jpg). [Online; accessed March 07, 2022].
- [12] Michael J. Behrenfeld and Emmanuel S. Boss. [Resurrecting the Ecological Underpinnings of Ocean Plankton Blooms](#). *Ann Rev Mar Sci*, 6(1):167–194, 2014. doi: 10.1146/annurev-marine-052913-021325.

- [13] Dennis J. McGillicuddy, Laurence A. Anderson, Nicholas R. Bates, Thomas Bibby, Ken O. Buesseler, Craig A. Carlson, Cabell S. Davis, Courtney Ewart, Paul G. Falkowski, Sarah A. Goldthwait, Dennis A. Hansell, William J. Jenkins, Rodney Johnson, Valery K. Kosnyrev, James R. Ledwell, Qian P. Li, David A. Siegel, and Deborah K. Steinberg. [Eddy/Wind Interactions Stimulate Extraordinary Mid-Ocean Plankton Blooms](#). *Science*, 316(5827):1021–1026, 2007. doi: 10.1126/science.1136256.
- [14] T. Kiørboe. *A mechanistic approach to plankton ecology*. Princeton University Press, 2008.
- [15] T. J. Pedley and J. O. Kessler. [Hydrodynamic Phenomena in Suspensions of Swimming Microorganisms](#). *Annu. Rev. Fluid Mech.*, 24(1):313–358, 1992. doi: 10.1146/annurev.fl.24.010192.001525.
- [16] G B Jeffery. [The motion of ellipsoidal particles immersed in a viscous fluid](#). *Proc. Math. Phys. Eng. Sci.*, 102(715):161–179, 1922. doi: 10.1098/rspa.1922.0078.
- [17] Rebekka E. Breier, Cristian C. Lalescu, Devin Waas, Michael Wilczek, and Marco G. Mazza. [Emergence of phytoplankton patchiness at small scales in mild turbulence](#). *Proc. Natl. Acad. Sci. U.S.A.*, 115(48):12112–12117, 2018. ISSN 0027-8424. doi: 10.1073/pnas.1808711115.
- [18] S Wang and A M Ardekani. [Unsteady swimming of small organisms](#). *J. Fluid Mech.*, 702:286–297, 2012. doi: 10.1017/jfm.2012.177.
- [19] William M Durham, Eric Climent, Michael Barry, Filippo De Lillo, Guido Boffetta, Massimo Cencini, and Roman Stocker. [Turbulence drives microscale patches of motile phytoplankton](#). *Nature communications*, 4(1):1–7, 2013. doi: 10.1038/ncomms3148.
- [20] Itzhak Fouxon and Alexander Leshansky. [Phytoplankton’s motion in turbulent ocean](#). *Phys. Rev. E*, 92:013017, 2015. doi: 10.1103/PhysRevE.92.013017.
- [21] François-Gaël Michalec, Sami Souissi, and Markus Holzner. [Turbulence triggers vigorous swimming but hinders motion strategy in planktonic copepods](#). *J R Soc Interface*, 12(106):20150158, 2015.
- [22] F G Michalec, I Fouxon, S Souissi, and M Holzner. [Zooplankton can actively adjust their motility to turbulent flow](#). *Proc. Natl. acad. Sci. U.S.A.*, 114(52):E11199–E11207, 2017. doi: <https://doi.org/10.1073/pnas.1708888114>.
- [23] N Pujara, M A R Koehl, and E A Variano. [Rotations and accumulation of ellipsoidal microswimmers in isotropic turbulence](#). *J. Fluid Mech.*, 838:356–368, 2018. doi: 10.1017/jfm.2017.912.
- [24] Caijuan Zhan, Gaetano Sardina, Enkeleida Lushi, and Luca Brandt. [Accumulation of motile elongated micro-organisms in turbulence](#). *J. Fluid Mech.*, 739:22–36, 2014. doi: 10.1017/jfm.2013.608.
- [25] A Roy, R J Hamati, L Tierney, D L Koch, and G A Voth. [Inertial torques and a symmetry breaking orientational transition in the sedimentation of slender fibres](#). *J. Fluid Mech.*, 875:576–596, 2019. doi: 10.1017/jfm.2019.492.

- [26] M Niazi Ardekani, G Sardina, L Brandt, L Karp-Boss, R Bearon, and E Variano. [Sedimentation of inertia-less prolate spheroids in homogenous isotropic turbulence with application to non-motile phytoplankton.](#) *J. Fluid Mech.*, 831:655–674, 2017. doi: 10.1017/jfm.2017.670.
- [27] Mehdi Niazi Ardekani, Pedro Costa, Wim Paul Breugem, and Luca Brandt. [Numerical study of the sedimentation of spheroidal particles.](#) *Int. J. Multiph. Flow*, 87:16–34, 2016. ISSN 0301-9322. doi: 10.1016/j.ijmultiphaseflow.2016.08.005.
- [28] K. Gustavsson, J. Jucha, A. Naso, E. Lévêque, A. Pumir, and B. Mehlig. [Statistical Model for the Orientation of Nonspherical Particles Settling in Turbulence.](#) *Phys. Rev. Lett.*, 119:254501, 2017. doi: 10.1103/PhysRevLett.119.254501.
- [29] Javier Ruiz, Diego Macías, and Francesc Peters. [Turbulence increases the average settling velocity of phytoplankton cells.](#) *Proc. Natl. Acad. Sci. U.S.A.*, 101(51):17720–17724, 2004. ISSN 0027-8424. doi: 10.1073/pnas.0401539101.
- [30] C. Siewert, R.P.J. Kunnen, M. Meinke, and W. Schröder. [Orientation statistics and settling velocity of ellipsoids in decaying turbulence.](#) *Atmospheric Research*, 142:45–56, 2014. ISSN 0169-8095. doi: 10.1016/j.atmosres.2013.08.011. The 16th International Conference on Clouds and Precipitation.
- [31] Matteo Borgnino, Jorge Arrieta, Guido Boffetta, Filippo De Lillo, and Idan Tuval. [Turbulence induces clustering and segregation of non-motile, buoyancy-regulating phytoplankton.](#) *Journal of The Royal Society Interface*, 16(159):20190324, 2019. doi: 10.1098/rsif.2019.0324.
- [32] Rachel N Bearon, AL Hazel, and GJ Thorn. [The spatial distribution of gyrotactic swimming micro-organisms in laminar flow fields.](#) *J. Fluid Mech.*, 680:602–635, 2011. doi: 10.1017/jfm.2011.198.
- [33] W M Durham, E Climent, and R Stocker. [Gyrotaxis in a steady vortical flow.](#) *Phys. Rev. Lett*, 106(23):238102, 2011. doi: 10.1103/PhysRevLett.106.238102.
- [34] F De Lillo, M Cencini, W M Durham, M Barry, R Stocker, E Climent, and G Boffetta. [Turbulent Fluid Acceleration Generates Clusters of Gyrotactic Microorganisms.](#) *Phys. Rev. Lett*, 112:044502, 2014. doi: 10.1103/PhysRevLett.112.044502.
- [35] F Santamaria, F De Lillo, M Cencini, and G Boffetta. [Gyrotactic trapping in laminar and turbulent Kolmogorov flow.](#) *Phys. Fluids*, 26(11):111901, 2014. doi: 10.1063/1.4900956.
- [36] K Gustavsson, F Berglund, P R Jonsson, and B Mehlig. [Preferential Sampling and Small-Scale Clustering of Gyrotactic Microswimmers in Turbulence.](#) *Phys. Rev. Lett*, 116:108104, 2016. doi: 10.1103/PhysRevLett.116.108104.
- [37] M Borgnino, F De Lillo, and G Boffetta. [Scale-dependent colocalization in a population of gyrotactic swimmers.](#) *Phys. Rev. E*, 95:023108, 2017. doi: 10.1103/PhysRevE.95.023108.
- [38] M Borgnino, G Boffetta, F De Lillo, and M Cencini. [Gyrotactic swimmers in turbulence: shape effects and role of the large-scale flow.](#) *J. Fluid Mech.*, 856:R1, 2018. doi: 10.1017/jfm.2018.767.

- [39] S. I. Heath Richardson, A. W. Baggaley, and N. A. Hill. [Gyrotactic suppression and emergence of chaotic trajectories of swimming particles in three-dimensional flows](#). *Phys. Rev. Fluids*, 3:023102, 2018. doi: 10.1103/PhysRevFluids.3.023102.
- [40] M Cencini, G Boffetta, M Borgnino, and F De Lillo. [Gyrotactic phytoplankton in laminar and turbulent flows: A dynamical systems approach](#). *Eur. Phys. J. E*, 42(3):31, 2019. doi: 10.1140/epje/i2019-11792-0.
- [41] Stephen B. Pope. *Turbulent Flows*. Cambridge University Press, 2000. doi: 10.1017/CBO9780511840531.
- [42] U. Frisch. *Turbulence: The Legacy of A. N. Kolmogorov*. Cambridge University Press, 1995. ISBN 9780521457132. doi: 10.1017/S0022112096210791.
- [43] J Z Wu, H Ma, and M D Zhou. *Vorticity and Vortex Dynamics*. Lecture notes in mathematics. Springer Berlin Heidelberg, 2007. doi: 10.1007/978-3-540-29028-5.
- [44] Peter Alan Davidson. *Turbulence: an introduction for scientists and engineers*. Oxford University Press, 2015. doi: 10.1093/acprof:oso/9780198722588.001.0001.
- [45] Lewis Fry Richardson. *Weather prediction by numerical process*. Cambridge university press, 1922.
- [46] Andrei Nikolaevich Kolmogorov. [The local structure of turbulence in incompressible viscous fluid for very large Reynolds numbers](#). *Proc. Math. Phys. Eng. Sci.*, 434(1890): 9–13, 1991. doi: 10.1098/rspa.1991.0075.
- [47] Andrei Nikolaevich Kolmogorov. The local structure of turbulence in incompressible viscous fluid for very large Reynolds numbers. *Dokl. Akad. Nauk SSSR*, (30):299–303, 1941.
- [48] Sualeh Khurshid, Diego A. Donzis, and K. R. Sreenivasan. [Energy spectrum in the dissipation range](#). *Phys. Rev. Fluids*, 3:082601, Aug 2018. doi: 10.1103/PhysRevFluids.3.082601.
- [49] Mickaël Bourgoïn and Haitao Xu. [Focus on dynamics of particles in turbulence](#). *New J. Phys.*, 16(8):085010, 2014. doi: 10.1088/1367-2630/16/8/085010.
- [50] Michael Junk and Reinhard Illner. [A new derivation of Jeffery’s equation](#). *J. Math. Fluid Mech.*, 9(4):455–488, 2007. doi: 10.1007/s00021-005-0208-0.
- [51] Greg A. Voth and Alfredo Soldati. [Anisotropic Particles in Turbulence](#). *Annu. Rev. Fluid Mech.*, 49(1):249–276, 2017. doi: 10.1146/annurev-fluid-010816-060135.
- [52] Edwin X. Berry and Richard L. Reinhardt. [An Analysis of Cloud Drop Growth by Collection: Part I. Double Distributions](#). *J Atmos Sci*, 31(7):1814 – 1824, 1974. doi: 10.1175/1520-0469(1974)031<1814:AAOCDG>2.0.CO;2.
- [53] Lian-Ping Wang, Anthony S. Wexler, and Yong Zhou. [Statistical mechanical descriptions of turbulent coagulation](#). *Phys. Fluids*, 10(10):2647–2651, 1998. doi: 10.1063/1.869777.

- [54] Michel Vosskuhle. *Particle collisions in turbulent flows*. PhD thesis, Lyon, École normale supérieure, 2013. URL <https://tel.archives-ouvertes.fr/tel-00946618>.
- [55] J. Jucha, A. Naso, E. Lévêque, and A. Pumir. [Settling and collision between small ice crystals in turbulent flows](#). *Phys. Rev. Fluids*, 3(1):014604, 2018. doi: 10.1103/PhysRevFluids.3.014604.
- [56] P. G. F. Saffman and J. S. Turner. [On the collision of drops in turbulent clouds](#). *J. Fluid Mech.*, 1(1):16–30, 1956. doi: 10.1017/S0022112056000020.
- [57] L.-P. Wang, A. S. Wexler, and Y. Zhou. [On the collision rate of small particles in isotropic turbulence. I. Zero-inertia case](#). *Phys. Fluids*, 10(1):266–276, 1998. doi: 10.1063/1.869565.
- [58] K Gustavsson, B Mehlig, and M Wilkinson. [Collisions of particles advected in random flows](#). *New J. Phys.*, 10(7):075014, jul 2008. doi: 10.1088/1367-2630/10/7/075014.
- [59] Barbara Schnitzer. [Collision rate of spheroids in turbulence](#). Master’s thesis, Chalmers University of Technology, Gothenburg, 2017. URL <https://hdl.handle.net/20.500.12380/253518>.
- [60] Xiaoyu Zheng, Wilder Iglesias, and Peter Palffy-Muhoray. [Distance of closest approach of two arbitrary hard ellipsoids](#). *Phys. Rev. E*, 79:057702, 2009. doi: 10.1103/PhysRevE.79.057702.
- [61] C. C Lalescu, B. Bramas, M. Rampp, and M. Wilczek. [An Efficient Particle Tracking Algorithm for Large-Scale Parallel Pseudo-Spectral Simulations of Turbulence](#). *Comput Phys Commun*, 278:108406, 2022. ISSN 0010-4655. doi: 10.1016/j.cpc.2022.108406.
- [62] M. Frigo and S.G. Johnson. [The Design and Implementation of FFTW3](#). *Proceedings of the IEEE*, 93(2):216–231, 2005. doi: 10.1109/JPROC.2004.840301.
- [63] Jeffrey S. Guasto, Roberto Rusconi, and Roman Stocker. [Fluid Mechanics of Planktonic Microorganisms](#). *Annu. Rev. Fluid Mech.*, 44(1):373–400, 2012. doi: 10.1146/annurev-fluid-120710-101156.
- [64] M Kim and A A Julius. *Microbiorobotics: Biologically Inspired Microscale Robotic Systems*. Micro and Nano Technologies. Elsevier Science, 2012. ISBN 9781455778942. doi: 10.1016/B978-0-32-342993-1.00020-3.
- [65] F G Schmitt and L Seuront. [Intermittent turbulence and copepod dynamics: Increase in encounter rates through preferential concentration](#). *J Mar Syst*, 70(3):263–272, 2008. doi: 10.1016/j.jmarsys.2007.01.008.
- [66] S Wang and A Ardekani. [Inertial squirmer](#). *Phys. Fluids*, 24(10):101902, 2012. doi: 10.1063/1.4758304.
- [67] G Li, A Ostace, and A M Ardekani. [Hydrodynamic interaction of swimming organisms in an inertial regime](#). *Phys. Rev. E*, 94:053104, 2016. doi: 10.1103/PhysRevE.94.053104.

- [68] B U Felderhof and R B Jones. [Effect of fluid inertia on swimming of a sphere in a viscous incompressible fluid.](#) *Eur J Mech B Fluids*, 75:312–326, 2019. doi: 10.1016/j.euromechflu.2018.10.012.
- [69] N Khurana and N T Ouellette. [Interactions between active particles and dynamical structures in chaotic flow.](#) *Phys. Fluids*, 24(9):091902, 2012. doi: 10.1063/1.4754873.
- [70] N Khurana and N T Ouellette. [Stability of model flocks in turbulent-like flow.](#) *New J. Phys.*, 15(9):095015, 2013. doi: 10.1088/1367-2630/15/9/095015.
- [71] A. Sengupta, F. Carrara, and R. Stocker. [Phytoplankton can actively diversify their migration strategy in response to turbulent cues.](#) *Nature*, 543(7646):555–558, 2017. doi: 10.1038/nature21415.
- [72] M Borgnino, K Gustavsson, F De Lillo, G Boffetta, M Cencini, and B Mehlig. [Alignment of Nonspherical Active Particles in Chaotic Flows.](#) *Phys. Rev. Lett*, 123:138003, 2019. doi: 10.1103/PhysRevLett.123.138003.
- [73] Alain Pumir and Michael Wilkinson. [Orientation statistics of small particles in turbulence.](#) *New J. Phys.*, 13(9):093030, 2011. doi: 10.1088/1367-2630/13/9/093030.
- [74] Laurent Chevillard and Charles Meneveau. [Orientation dynamics of small, triaxial–ellipsoidal particles in isotropic turbulence.](#) *J. Fluid Mech.*, 737:571–596, 2013. doi: 10.1017/jfm.2013.580.
- [75] Rui Ni, Nicholas T. Ouellette, and Greg A. Voth. [Alignment of vorticity and rods with Lagrangian fluid stretching in turbulence.](#) *J. Fluid Mech.*, 743:R3, 2014. doi: 10.1017/jfm.2014.32.
- [76] Shima Parsa, Enrico Calzavarini, Federico Toschi, and Greg A. Voth. [Rotation Rate of Rods in Turbulent Fluid Flow.](#) *Phys. Rev. Lett.*, 109:134501, 2012. doi: 10.1103/PhysRevLett.109.134501.
- [77] Nimish Pujara and Evan A. Variano. [Rotations of small, inertialess triaxial ellipsoids in isotropic turbulence.](#) *J. Fluid Mech.*, 821:517–538, 2017. doi: 10.1017/jfm.2017.256.
- [78] A Zöttl and H Stark. [Nonlinear Dynamics of a Microswimmer in Poiseuille Flow.](#) *Phys. Rev. Lett*, 108:218104, 2012. doi: 10.1103/PhysRevLett.108.218104.
- [79] R Chacón. [Chaotic dynamics of a microswimmer in Poiseuille flow.](#) *Phys. Rev. E*, 88:052905, 2013. doi: 10.1103/PhysRevE.88.052905.
- [80] A Zöttl and H Stark. [Periodic and quasiperiodic motion of an elongated microswimmer in Poiseuille flow.](#) *Eur. Phys. J. E*, 36(1):4, 2013. doi: 10.1140/epje/i2013-13004-5.
- [81] A Sokolov and I S Aranson. [Rapid expulsion of microswimmers by a vortical flow.](#) *Nat. Commun.*, 7:11114, 2016. doi: 10.1038/ncomms11114.
- [82] P A Jumars, J H Trowbridge, E Boss, and L Karp-Boss. [Turbulence-plankton interactions: a new cartoon.](#) *Mar. Ecol.*, 30(2):133–150, 2009. doi: 10.1111/j.1439-0485.2009.00288.x.

- [83] C Torney and Z Neufeld. [Transport and Aggregation of Self-Propelled Particles in Fluid Flows](#). *Phys. Rev. Lett*, 99:078101, 2007. doi: 10.1103/PhysRevLett.99.078101.
- [84] N Khurana, J Blawdziewicz, and N T Ouellette. [Reduced Transport of Swimming Particles in Chaotic Flow due to Hydrodynamic Trapping](#). *Phys. Rev. Lett.*, 106:198104, 2011. doi: 10.1103/PhysRevLett.106.198104.
- [85] M Tarama, A M Menzel, and H Löwen. [Deformable microswimmer in a swirl: Capturing and scattering dynamics](#). *Phys. Rev. E*, 90:032907, 2014. doi: 10.1103/PhysRevE.90.032907.
- [86] T Kaya and H Koser. [Characterization of Hydrodynamic Surface Interactions of Escherichia coli Cell Bodies in Shear Flow](#). *Phys. Rev. Lett*, 103:138103, 2009. doi: 10.1103/PhysRevLett.103.138103.
- [87] W J Devenport, M C Rife, S I Liapis, and G J Follin. [The structure and development of a wing-tip vortex](#). *J. Fluid Mech.*, 312:67—106, 1996. doi: 10.1017/S0022112096001929.
- [88] S H Strogatz. *Nonlinear Dynamics and Chaos: With Applications to Physics, Biology, Chemistry, and Engineering*. Studies in Nonlinearity. Avalon Publishing, 2014. ISBN 9780813349114.
- [89] David Liittschwager. [Marine microplankton and mesoplankton](#), 2006. URL [https://en.wikipedia.org/wiki/Plankton#/media/File:Marine\\_microplankton.jpg](https://en.wikipedia.org/wiki/Plankton#/media/File:Marine_microplankton.jpg). [Online; accessed March 07, 2022].
- [90] Anupam Gupta, Amal Roy, Arnab Saha, and Samridhi Sankar Ray. [Flocking of active particles in a turbulent flow](#). *Phys. Rev. Fluids*, 5:052601, 2020. doi: 10.1103/PhysRevFluids.5.052601.
- [91] T J Pedley. [Gyrotaxis in uniform vorticity](#). *J. Fluid Mech.*, 762:R6, 2015. doi: 10.1017/jfm.2014.666.
- [92] M Cencini, Marta Franchino, Francesco Santamaria, and Guido Boffetta. [Centripetal focusing of gyrotactic phytoplankton](#). *J. Theor. Biol.*, 399:62–70, 2016. ISSN 0022-5193. doi: 10.1016/j.jtbi.2016.03.037.
- [93] T B Oehmke, A D Bordoloi, E Variano, and G Verhille. [Spinning and tumbling of long fibers in isotropic turbulence](#). *Phys. Rev. Fluids*, 6:044610, 2021. doi: 10.1103/PhysRevFluids.6.044610.
- [94] M. Byron, J. Einarsson, K. Gustavsson, G. Voth, B. Mehlig, and E. Variano. [Shape-dependence of particle rotation in isotropic turbulence](#). *Phys. Fluids*, 27(3):035101, 2015. doi: 10.1063/1.4913501.
- [95] Nimish Pujara, José-Agustín Arguedas-Leiva, Cristian C Lalescu, Bérenger Bramas, and Michael Wilczek. [Shape-and scale-dependent coupling between spheroids and velocity gradients in turbulence](#). *J. Fluid Mech.*, 922, 2021. doi: 10.1017/jfm.2021.543.
- [96] Jonas Einarsson. *Angular dynamics of small particles in fluids*. PhD thesis, Göteborg, University of Gothenburg, 2015. URL <http://hdl.handle.net/2077/40830>.

- [97] Rui Ni, Stefan Kramel, Nicholas T. Ouellette, and Greg A. Voth. [Measurements of the coupling between the tumbling of rods and the velocity gradient tensor in turbulence](#). *J. Fluid Mech.*, 766:202–225, 2015. doi: 10.1017/jfm.2015.16.
- [98] Nimish Pujara, Theresa B. Oehmke, Ankur D. Bordoloi, and Evan A. Variano. [Rotations of large inertial cubes, cuboids, cones, and cylinders in turbulence](#). *Phys. Rev. Fluids*, 3:054605, 2018. doi: 10.1103/PhysRevFluids.3.054605.
- [99] M. Shin and D.L. Koch. [Rotational and translational dispersion of fibres in isotropic turbulent flows](#). *J. Fluid Mech.*, 540:143–173, 2005. doi: 10.1017/S0022112005005690.
- [100] K. Gustavsson, J. Einarsson, and B. Mehlig. [Tumbling of Small Axisymmetric Particles in Random and Turbulent Flows](#). *Phys. Rev. Lett.*, 112:014501, 2014. doi: 10.1103/PhysRevLett.112.014501.
- [101] E. Calzavarini, Y. X. Huang, F. G. Schmitt, and L. P. Wang. [Propelled microprobes in turbulence](#). *Phys. Rev. Fluids*, 3:054604, 2018. doi: 10.1103/PhysRevFluids.3.054604.
- [102] C. Siewert, R. P. J. Kunnen, and W. Schröder. [Collision rates of small ellipsoids settling in turbulence](#). *J. Fluid Mech.*, 758:686–701, 2014. doi: 10.1017/jfm.2014.554.
- [103] Alain Pumir and Michael Wilkinson. [Collisional Aggregation Due to Turbulence](#). *Annu. Rev. Condens. Matter Phys.*, 7(1):141–170, 2016. doi: 10.1146/annurev-conmatphys-031115-011538.
- [104] François-Gaël Michalec, Itzhak Fouxon, Sami Souissi, and Markus Holzner. [Efficient mate finding in planktonic copepods swimming in turbulence](#). *eLife*, 9:e62014, 2020. ISSN 2050-084X. doi: 10.7554/eLife.62014.
- [105] Andre W Visser and Thomas Kiørboe. [Plankton motility patterns and encounter rates](#). *Oecologia*, 148(3):538–546, 2006. doi: 10.1007/s00442-006-0385-4.
- [106] Anders Andersen and Julia Dölger. [Planktonic encounter rates with non-spherical encounter zones](#). *J. R. Soc. Interface*, 16(156):20190398, 2019. doi: 10.1098/rsif.2019.0398.
- [107] Walter John Moore. *Physical chemistry*. Orient Blackswan, 1972.
- [108] P. G. Falkowski, R. T. Barber, and V. Smetacek. [Biogeochemical controls and feedbacks on ocean primary production](#). *Science*, 281(5374):200–206, 1998. doi: 10.1126/science.281.5374.200.
- [109] A. Ryabov, O. Kerimoglu, E. Litchman, I. Olenina, L. Roselli, A. Basset, E. Stanca, and B. Blasius. [Shape matters: the relationship between cell geometry and diversity in phytoplankton](#). *Ecol. Lett.*, 24(4):847–861, 2021. doi: 10.1111/ele.13680.
- [110] W. R. Calvano, E. Boss, and L. Karp-Boss. [Inherent optical properties of non-spherical marine-like particles—from theory to observation](#). *Oceanogr. Mar. Biol. Ann. Rev.*, 45:1–38, 2007.
- [111] R. M. Letelier and D.M. Karl. [Role of \*Trichodesmium\* spp. in the productivity of the subtropical North Pacific Ocean](#). *Mar. Ecol. Prog. Ser.*, 133:263–273, 1996. doi: 10.3354/meps133263.

- [112] A. E. White, K. S. Watkins-Brandt, and M. J. Church. [Temporal variability of \*Trichodesmium\* spp. and diatom-diazotroph assemblages in the North Pacific subtropical gyre.](#) *Front. Mar. Sci.*, 5:27, 2018. doi: 10.3389/fmars.2018.00027.
- [113] K. W. Wirtz. [Non-uniform scaling in phytoplankton growth rate due to intracellular light and CO<sub>2</sub> decline.](#) *J. Plankton Res.*, 33(9):1325–1341, 2011.
- [114] M. Pančić and T. Kiørboe. [Phytoplankton defence mechanisms: traits and trade-offs.](#) *Biol. Rev.*, 93(2):1269–1303, 2018. doi: 10.1111/brv.12395.
- [115] L. Naselli-Flores and R. Barone. [Invited review-fight on plankton! Or, phytoplankton shape and size as adaptive tools to get ahead in the struggle for life.](#) *Cryptogam., Algal.*, 32(2):157–204, 2011. doi: 10.7872/crya.v32.iss2.2011.157.
- [116] J. S. Font-Muñoz, R. Jeanneret, J. Arrieta, S. Anglès, A. Jordi, I. Tuval, and G. Basterretxea. [Collective sinking promotes selective cell pairing in planktonic pennate diatoms.](#) *Proc. Natl. Acad. Sci. U. S. A.*, 116(32):15997–16002, 2019. doi: 10.1073/pnas.1904837116.
- [117] J. Słomka and R. Stocker. [On the collision of rods in a quiescent fluid.](#) *Proc. Natl. Acad. Sci. U. S. A.*, 117(7):3372–3374, 2020. doi: 10.1073/pnas.1917163117.
- [118] A. B. Burd and G. A. Jackson. [Particle aggregation.](#) *Ann. Rev. Mar. Sci.*, 1:65–90, 2009. doi: <https://doi.org/10.1146/annurev.marine.010908.163904>.
- [119] A. L. Alldredge and C. C. Gotschalk. [Direct observations of the mass flocculation of diatom blooms: characteristics, settling velocities and formation of diatom aggregates.](#) *Deep Sea Res. A*, 36(2):159–171, 1989. doi: [https://doi.org/10.1016/0198-0149\(89\)90131-3](https://doi.org/10.1016/0198-0149(89)90131-3).
- [120] P. W. Boyd, H. Claustre, M. Levy, D. A. Siegel, and T. Weber. [Multi-faceted particle pumps drive carbon sequestration in the ocean.](#) *Nature*, 568(7752):327–335, 2019. doi: 10.1038/s41586-019-1098-2.
- [121] Uria Alcolombri, François J Peaudecerf, Vicente I Fernandez, Lars Behrendt, Kang Soo Lee, and Roman Stocker. [Sinking enhances the degradation of organic particles by marine bacteria.](#) *Nat. Geosci.*, 14(10):775–780, 2021. doi: 10.1038/s41561-021-00817-x.
- [122] D. Thornton. [Diatom aggregation in the sea: mechanisms and ecological implications.](#) *Eur. J. Phycol.*, 37(2):149–161, 2002. doi: 10.1017/S0967026202003657.
- [123] T. A. Villareal, M. A. Altabet, and K. Culver-Rymsza. [Nitrogen transport by vertically migrating diatom mats in the North Pacific Ocean.](#) *Nature*, 363(6431):709–712, 1993. doi: 10.1038/363709a0.
- [124] D. G. Capone, J. P Zehr, H. W. Paerl, B. Bergman, and E. J. Carpenter. [Trichodesmium, a globally significant marine cyanobacterium.](#) *Science*, 276(5316):1221–1229, 1997. doi: 10.1126/science.276.5316.1221.
- [125] J. P. Zehr and D. G. Capone. [Changing perspectives in marine nitrogen fixation.](#) *Science*, 368(6492), 2020.

- [126] T. A. Villareal and E. J. Carpenter. [Buoyancy regulation and the potential for vertical migration in the oceanic cyanobacterium \*Trichodesmium\*](#). *Microb. Ecol.*, 45(1):1–10, 2003. doi: 10.1007/s00248-002-1012-5.
- [127] A. E. Walsby. [The properties and buoyancy-providing role of gas vacuoles in \*Trichodesmium\* Ehrenberg](#). *Brit. Phycol. J.*, 13(2):103–116, 1978. doi: 10.1080/00071617800650121.
- [128] J. M. C. Hutchinson and P. M. Waser. [Use, misuse and extensions of “ideal gas” models of animal encounter](#). *Biol. Rev.*, 82(3):335–359, 2007. doi: 10.1111/j.1469-185X.2007.00014.x.
- [129] T. Kiørboe, C. Lundsgaard, M. Olesen, and J. L. S. Hansen. [Aggregation and sedimentation processes during a spring phytoplankton bloom: a field experiment to test coagulation theory](#). *J. Mar. Res.*, 52(2):297–323, 1994. doi: 10.1357/0022240943077145.
- [130] M. Takabayashi, K. Lew, A. Johnson, A. L. Marchi, R. Dugdale, and F. P. Wilkerson. [The effect of nutrient availability and temperature on chain length of the diatom, \*Skeletonema costatum\*](#). *J. Plankton Res.*, 28(9):831–840, 2006. doi: 10.1093/plankt/fbl018.
- [131] V. Singh, D. L. Koch, and A. D. Stroock. [Ideal rate of collision of cylinders in simple shear flow](#). *Langmuir*, 27(19):11813–11823, 2011. doi: 10.1021/la202138t.
- [132] G. Falkovich, A. Fouxon, and M. G. Stepanov. [Acceleration of rain initiation by cloud turbulence](#). *Nature*, 419(6903):151–154, 2002. doi: 10.1038/nature00983.
- [133] S. T. Wilson, N. J. Hawco, E. V. Armbrust, B. Barone, K. M. Björkman, A. K. Boysen, M. Burgos, T. J. Burrell, J. R. Casey, E. F. DeLong, et al. [Kilauea lava fuels phytoplankton bloom in the North Pacific Ocean](#). *Science*, 365(6457):1040–1044, 2019. doi: 10.1126/science.aax4767.
- [134] W. M. Dunstan and J. Hosford. [The distribution of planktonic blue green algae related to the hydrography of the Georgia Bight](#). *Bull. Mar. Sci.*, 27(4):824–829, 1977.
- [135] M. Rodier and R. Le Borgne. [Population and trophic dynamics of \*Trichodesmium thiebautii\* in the SE lagoon of New Caledonia. Comparison with \*T. erythraeum\* in the SW lagoon](#). *Mar. Pollut. Bull.*, 61(7-12):349–359, 2010. doi: 10.1016/j.marpolbul.2010.06.018.
- [136] D. Spungin, U. Pfreundt, H. Berthelot, S. Bonnet, D. AlRoumi, F. Natale, W. R. Hess, K. D. Bidle, and I. Berman-Frank. [Mechanisms of \*Trichodesmium\* demise within the New Caledonian lagoon during the VAHINE mesocosm experiment](#). *Biogeosciences*, 13(14):4187–4203, 2016. doi: 10.5194/bg-13-4187-2016.
- [137] A. E. White, Y. H. Spitz, and R. M. Letelier. [Modeling carbohydrate ballasting by \*Trichodesmium\* spp.](#) *Mar. Ecol. Prog. Ser.*, 323:35–45, 2006. doi: 10.3354/meps323035.
- [138] M. Rouco, S. T. Haley, and S. T. Dyrman. [Microbial diversity within the \*Trichodesmium\* holobiont](#). *Environ. Microbiol.*, 18(12):5151–5160, 2016. doi: 10.1111/1462-2920.13513.

- [139] E. J. Carpenter, A. Subramaniam, and D. G. Capone. [Biomass and primary productivity of the cyanobacterium \*Trichodesmium\* spp. in the tropical N Atlantic ocean.](#) *Deep Sea Res. 1 Oceanogr. Res. Pap.*, 51(2):173–203, 2004. doi: <https://doi.org/10.1016/j.dsr.2003.10.006>.
- [140] Ò. Guadayol, F. Peters, J. E. Stiansen, C. Marrasé, and A. Lohrmann. [Evaluation of oscillating grids and orbital shakers as means to generate isotropic and homogeneous small-scale turbulence in laboratory enclosures commonly used in plankton studies.](#) *Limnol. Oceanogr. Meth.*, 7(4):287–303, 2009. doi: [10.4319/lom.2009.7.287](https://doi.org/10.4319/lom.2009.7.287).
- [141] A. Naso, J. Jucha, E. Lévêque, and A. Pumir. [Collision rate of ice crystals with water droplets in turbulent flows.](#) *J. Fluid Mech.*, 845:615–641, 2018. doi: [10.1017/jfm.2018.238](https://doi.org/10.1017/jfm.2018.238).
- [142] P. Anand, S. S. Ray, and G. Subramanian. [Orientation dynamics of sedimenting anisotropic particles in turbulence.](#) *Phys. Rev. Lett.*, 125(3):034501, 2020. doi: [10.1103/PhysRevLett.125.034501](https://doi.org/10.1103/PhysRevLett.125.034501).
- [143] S. Brizzolara, M. E. Rosti, S. Olivieri, L. Brandt, M. Holzner, and A. Mazzino. [Fiber Tracking Velocimetry for Two-Point Statistics of Turbulence.](#) *Phys. Rev. X*, 11:031060, 2021. doi: [10.1103/PhysRevX.11.031060](https://doi.org/10.1103/PhysRevX.11.031060).
- [144] J. Happel and H. Brenner. *Low Reynolds number hydrodynamics: with special applications to particulate media*, volume 1. Springer Science & Business Media, 2012. doi: [10.1007/978-94-009-8352-6](https://doi.org/10.1007/978-94-009-8352-6).
- [145] J. R. N. Lazier and K. H. Mann. [Turbulence and the diffusive layers around small organisms.](#) *Deep Sea Res. A*, 36(11):1721–1733, 1989. doi: [10.1016/0198-0149\(89\)90068-X](https://doi.org/10.1016/0198-0149(89)90068-X).
- [146] S. A. Thorpe. *An Introduction to Ocean Turbulence*. Cambridge University Press, 2007. doi: [10.1017/CBO9780511801198](https://doi.org/10.1017/CBO9780511801198).
- [147] M. Von Smoluchowski. Drei Vorträge über Diffusion, Brownsche Bewegung und Koagulation von Kolloidteilchen. *Z. Phys.*, 17:557–585, 1916.
- [148] G. A. Jackson. [A model of the formation of marine algal flocs by physical coagulation processes.](#) *Deep Sea Res. A*, 37(8):1197–1211, 1990. doi: [10.1016/0198-0149\(90\)90038-W](https://doi.org/10.1016/0198-0149(90)90038-W).
- [149] K. R. Sreenivasan. [Fluid turbulence.](#) *Rev. Mod. Phys.*, 71(2):S383, 1999. doi: [10.1103/RevModPhys.71.S383](https://doi.org/10.1103/RevModPhys.71.S383).
- [150] Alexandros Alexakis and Luca Biferale. [Cascades and transitions in turbulent flows.](#) *Phys. Rep.*, 767:1–101, 2018. doi: [10.1016/j.physrep.2018.08.001](https://doi.org/10.1016/j.physrep.2018.08.001).
- [151] Dieter Biskamp. *Magnetohydrodynamic turbulence*. Cambridge University Press, 2003. doi: [10.1017/CBO9780511535222](https://doi.org/10.1017/CBO9780511535222).
- [152] Giorgio Parisi, Uriel Frisch, et al. A multifractal model of intermittency. In *Turbulence and predictability in geophysical fluid dynamics and climate dynamics*, pages 84–88. North-Holland, Amsterdam, 1985.

- [153] Robert H Kraichnan. [Models of intermittency in hydrodynamic turbulence](#). *Phys. Rev. Lett.*, 65(5):575, 1990. doi: 10.1103/PhysRevLett.65.575.
- [154] Javier Jiménez. [Cascades in wall-bounded turbulence](#). *Annu. Rev. Fluid Mech.*, 44:27–45, 2012. doi: 10.1146/annurev-fluid-120710-101039.
- [155] Thomas Duriez, Steven L Brunton, and Bernd R Noack. [Machine learning control-taming nonlinear dynamics and turbulence](#). Springer, 2017. doi: 10.1007/978-3-319-40624-4.
- [156] Francesco Ragone, Jeroen Wouters, and Freddy Bouchet. [Computation of extreme heat waves in climate models using a large deviation algorithm](#). *Proc. Natl. Acad. Sci. U.S.A.*, 115(1):24–29, 2018. doi: 10.1073/pnas.1712645115.
- [157] L. Biferale, F. Bonaccorso, I. M. Mazzitelli, M. A. T. van Hinsberg, A. S. Lanotte, S. Musacchio, P. Perlekar, and F. Toschi. [Coherent Structures and Extreme Events in Rotating Multiphase Turbulent Flows](#). *Phys. Rev. X*, 6:041036, 2016. doi: 10.1103/PhysRevX.6.041036.
- [158] Charles L Fefferman. Existence and smoothness of the Navier-Stokes equation. *The millennium prize problems*, 57:67, 2006.
- [159] C. Meneveau and J. Katz. [Scale-invariance and turbulence models for large-eddy simulation](#). *Annu. Rev. Fluid Mech.*, 32:1, 2000. doi: 10.1146/annurev.fluid.32.1.1.
- [160] Richard J. A. M. Stevens, Michael Wilczek, and Charles Meneveau. [Large-eddy simulation study of the logarithmic law for second- and higher-order moments in turbulent wall-bounded flow](#). *J. Fluid Mech.*, 757:888–907, 2014. doi: 10.1017/jfm.2014.510.
- [161] Luca Biferale. [Shell models of energy cascade in turbulence](#). *Annu. Rev. Fluid Mech.*, 35(1):441–468, 2003. doi: 10.1146/annurev.fluid.35.101101.161122.
- [162] Tomas Bohr, Mogens H Jensen, Giovanni Paladin, and Angelo Vulpiani. [Dynamical systems approach to turbulence](#). Cambridge University Press, 2005. doi: 10.1017/CBO9780511599972.
- [163] Marcel Lesieur. [Turbulence in fluids](#), volume 40. Springer Science & Business Media, 2012. doi: 10.1007/978-1-4020-6435-7.
- [164] Zhen-Su She and Eric Jackson. [Constrained Euler system for Navier-Stokes turbulence](#). *Phys. Rev. Lett.*, 70:1255–1258, 1993. doi: 10.1103/PhysRevLett.70.1255.
- [165] Luca Biferale, Fabio Bonaccorso, Michele Buzzicotti, and Kartik P. Iyer. [Self-Similar Subgrid-Scale Models for Inertial Range Turbulence and Accurate Measurements of Intermittency](#). *Phys. Rev. Lett.*, 123:014503, 2019. doi: 10.1103/PhysRevLett.123.014503.
- [166] Vladimir E Zakharov, Victor S L’vov, and Gregory Falkovich. [Kolmogorov spectra of turbulence I: Wave turbulence](#). Springer Science & Business Media, 2012. doi: 10.1007/978-3-642-50052-7.
- [167] Sergey Nazarenko. [Wave turbulence](#), volume 825. Springer Science & Business Media, 2011. doi: 10.1007/978-3-642-15942-8.

- [168] Michele Buzzicotti, Brendan P Murray, Luca Biferale, and Miguel D Bustamante. [Phase and precession evolution in the Burgers equation](#). *Eur Phys J E Soft Matter*, 39(3):1–9, 2016. doi: 10.1140/epje/i2016-16034-5.
- [169] J. M. Reynolds-Barredo, D. E. Newman, P. W. Terry, and R. Sanchez. [Fourier signature of filamentary vorticity structures in two-dimensional turbulence](#). *EPL (Europhysics Letters)*, 115(3):34002, 2016. doi: 10.1209/0295-5075/115/34002.
- [170] Michael Wilczek, Dimitar G. Vlaykov, and Cristian C. Lalescu. *Emergence of Non-Gaussianity in Turbulence*, pages 3–9. Springer International Publishing, Cham, 2017. doi: 10.1007/978-3-319-57934-4\_1.
- [171] Jose-Agustin Arguedas-Leiva. [Phase coherence and intermittency of a turbulent field based on a system of coupled oscillators](#). Master’s thesis, Georg-August-Universität, Göttingen, 2017. URL <http://hdl.handle.net/21.11116/0000-0008-B2C8-D>.
- [172] Brendan P. Murray and Miguel D. Bustamante. [Energy flux enhancement, intermittency and turbulence via Fourier triad phase dynamics in the 1-D Burgers equation](#). *J. Fluid Mech.*, 850:624–645, 2018. doi: 10.1017/jfm.2018.454.
- [173] Michael G Rosenblum, Arkady S Pikovsky, and Jürgen Kurths. [Phase synchronization of chaotic oscillators](#). *Phys. Rev. Lett.*, 76(11):1804, 1996. doi: 10.1103/PhysRevLett.76.1804.
- [174] Stefano Boccaletti, Jürgen Kurths, Grigory Osipov, DL Valladares, and CS Zhou. [The synchronization of chaotic systems](#). *Phys. Rep.*, 366(1-2):1–101, 2002. doi: 10.1016/S0370-1573(02)00137-0.
- [175] Oleg Zikanov, Andre Thess, and Rainer Grauer. [Statistics of turbulence in a generalized random-force-driven Burgers equation](#). *Phys. Fluids*, 9(5):1362–1367, 1997. doi: 10.1063/1.869250.
- [176] E Balkovsky, G Falkovich, I Kolokolov, and V Lebedev. [Intermittency of Burgers’ turbulence](#). *Phys. Rev. Lett.*, 78(8):1452, 1997. doi: 10.1103/PhysRevLett.78.1452.
- [177] Jérémie Bec and Konstantin Khanin. [Burgers turbulence](#). *Phys. Rep.*, 447(1-2):1–66, 2007. doi: 10.1016/j.physrep.2007.04.002.
- [178] G Da Prato, A Debussche, and R Temam. [Stochastic Burgers’ equation](#). *Nonlinear Differ. Equ. Appl.*, 1(4):389–402, 1994. doi: 10.1007/BF01194987.
- [179] Alexei Chekhlov and Victor Yakhot. [Kolmogorov turbulence in a random-force-driven Burgers equation](#). *Phys. Rev. E*, 51(4):R2739, 1995. doi: 10.1103/PhysRevE.51.R2739.
- [180] Gregory L Eyink and Theodore D Drivas. [Spontaneous stochasticity and anomalous dissipation for Burgers equation](#). *J. Stat. Phys.*, 158(2):386–432, 2015.
- [181] Zhen-Su She, Erik Aurell, and Uriel Frisch. [The inviscid Burgers equation with initial data of Brownian type](#). *Commun. Math. Phys.*, 148(3):623–641, 1992. doi: 10.1007/BF02096551.

- [182] Jean-Philippe Bouchaud, Marc Mézard, and Giorgio Parisi. [Scaling and intermittency in Burgers turbulence](#). *Phys. Rev. E*, 52(4):3656, 1995. doi: 10.1103/PhysRevE.52.3656.
- [183] E Weinan, Konstantin Khanin, Alexander Mazel, and Ya Sinai. [Invariant measures for Burgers equation with stochastic forcing](#). *Ann. Math.*, pages 877–960, 2000. doi: 10.2307/121126.
- [184] Michele Buzzicotti, Luca Biferale, Uriel Frisch, and Samriddhi Sankar Ray. [Intermittency in fractal Fourier hydrodynamics: Lessons from the Burgers equation](#). *Phys. Rev. E*, 93(3):033109, 2016. doi: 10.1103/PhysRevE.93.033109.
- [185] Giovanni Gallavotti. [Non equilibrium in statistical and fluid mechanics. Ensembles and their equivalence. Entropy driven intermittency](#). *J. Math. Phys.*, 41(6):4061–4081, 2000. doi: 10.1063/1.533335.
- [186] Giovanni Gallavotti. [Entropy, Thermostats and Chaotic Hypothesis](#). *Chaos*, 16:043114 (+6), 2006. doi: 10.1063/1.2372713.
- [187] L. Biferale, M. Cencini, M. DePietro, G. Gallavotti, and V. Lucarini. [Equivalence of Non-Equilibrium Ensembles in Turbulence Models](#). *Phys. Rev. E*, 98:012201, 2018. doi: 10.1103/PhysRevE.98.012202.
- [188] Vishwanath Shukla, Bérengère Dubrulle, Sergey Nazarenko, Giorgio Krstulovic, and Simon Thalabard. [Phase transition in time-reversible Navier-Stokes equations](#). *Phys. Rev. E*, 100:043104, 2019. doi: 10.1103/PhysRevE.100.043104.
- [189] HA Rose and PL Sulem. [Fully developed turbulence and statistical mechanics](#). *J. Phys.*, 39(5):441–484, 1978. doi: 10.1051/jphys:01978003905044100.
- [190] F. Ginelli, P. Poggi, A. Turchi, H. Chaté, R. Livi, and A. Politi. [Characterizing Dynamics with Covariant Lyapunov Vectors](#). *Phys. Rev. Lett.*, 99(13):130601, 2007. ISSN 0031-9007. doi: 10.1103/PhysRevLett.99.130601.
- [191] James L Kaplan and James A Yorke. [Chaotic behavior of multidimensional difference equations](#). In *Functional differential equations and approximation of fixed points*, pages 204–227. Springer, 1979. doi: 10.1007/BFb0064319.
- [192] Paul Frederickson, James L Kaplan, Ellen D Yorke, and James A Yorke. [The Liapunov dimension of strange attractors](#). *J. Differ. Equ.*, 49(2):185–207, 1983. doi: 10.1016/0022-0396(83)90011-6.
- [193] IA Shepelev, GI Strelkova, and VS Anishchenko. [Chimera states and intermittency in an ensemble of nonlocally coupled Lorenz systems](#). *Chaos*, 28(6):063119, 2018. doi: 10.1063/1.5020009.
- [194] Catherine Sulem, Pierre-Louis Sulem, and Hélène Frisch. [Tracing complex singularities with spectral methods](#). *J. Comput. Phys.*, 50(1):138–161, 1983. ISSN 0021-9991. doi: 10.1016/0021-9991(83)90045-1.

- [195] Miguel D. Bustamante and Marc Brachet. [Interplay between the Beale-Kato-Majda theorem and the analyticity-strip method to investigate numerically the incompressible Euler singularity problem.](#) *Phys. Rev. E*, 86:066302, 2012. doi: 10.1103/PhysRevE.86.066302.
- [196] A D Bordoloi, E Variano, and G Verhille. [Lagrangian Time Scale of Passive Rotation for Mesoscale Particles in Turbulence.](#) *Front. Mar. Sci.*, 7:199–8, 2020. doi: 10.3389/fmars.2020.00473.
- [197] K Spurny. *Aerosol Chemistry and Its Environmental Effects*, chapter Atmospheric Contamination by Fibrous Aerosols. Lewis Publishers, 2000.
- [198] A J Mehta. *An introduction to hydraulics of fine sediment transport*. World Scientific Publishing Company, 2013. doi: 10.1142/8708.
- [199] K Gustavsson and B Mehlig. [Statistical models for spatial patterns of heavy particles in turbulence.](#) *Advances in Physics*, 65:1–57, 2016. doi: 10.1080/00018732.2016.1164490.
- [200] K Gustavsson, M Z Sheikh, A Naso, A Pumir, and B Mehlig. [Effect of particle inertia on the alignment of small ice crystals in turbulent clouds.](#) *J. Atmos. Sci.*, 2021. doi: 10.1175/JAS-D-20-0221.1.
- [201] C Li, K Lim, T Berk, A Abraham, M Heisel, M Guala, F Coletti, and J Hong. [Settling and clustering of snow particles in atmospheric turbulence.](#) *J. Fluid Mech.*, 912:A49, 2021. doi: 10.1017/jfm.2020.1153.
- [202] O Samant, J K Alageshan, S Sharma, and A Kuley. [Dynamic mode decomposition of inertial particle caustics in Taylor–Green flow.](#) *Sci. Rep.*, 11:10456, 2021. doi: 10.1038/s41598-021-89953-3.
- [203] F Lundell, L D Söderberg, and P H Alfredsson. [Fluid Mechanics of Papermaking.](#) *Annu. Rev. Fluid Mech.*, 43:195–217, 2011. doi: 10.1146/annurev-fluid-122109-160700.
- [204] R Clift, J R Grace, and M E Weber. *Bubbles, drops, and particles*. Dover publications, 2005.
- [205] M Niazi Ardekani, P Costa, W-P Breugem, F Picano, and L Brandt. [Drag reduction in turbulent channel flow laden with finite-size oblate spheroids.](#) *J. Fluid Mech.*, 816:43–70, 2017. doi: 10.1017/jfm.2017.68.
- [206] M Niazi Ardekani and L Brandt. [Turbulence modulation in channel flow of finite-size spheroidal particles.](#) *J. Fluid Mech.*, 859:887–901, 2018. doi: 10.1017/jfm.2018.854.
- [207] L Schneiders, K Fröhlich, M Meinke, and W Schröder. [The decay of isotropic turbulence carrying non-spherical finite-size particles.](#) *J. Fluid Mech.*, 875:520–542, 2019. doi: 10.1017/jfm.2019.516.
- [208] J B Will, V Mathai, S G Huisman, D Lohse, C Sun, and D Krug. [Kinematics and dynamics of freely rising spheroids at high Reynolds numbers.](#) *J. Fluid Mech.*, 912:A16, 2021. doi: 10.1017/jfm.2020.1104.

- [209] M E Rosti, A A Banaei, L Brandt, and A Mazzino. [Flexible Fiber Reveals the Two-Point Statistical Properties of Turbulence](#). *Phys. Rev. Lett*, 121:044501, 2018. doi: 10.1103/PhysRevLett.121.044501.
- [210] B Hejazi, M Krellenstein, and G A Voth. [Using deformable particles for single-particle measurements of velocity gradient tensors](#). *Exp. Fluids*, 60:153, 2019. doi: 10.1007/s00348-019-2796-0.
- [211] M Cavaiola, S Olivieri, and A Mazzino. [The assembly of freely moving rigid fibres measures the flow velocity gradient tensor](#). *J. Fluid Mech.*, 894:A25, 2020. doi: 10.1017/jfm.2020.288.
- [212] L A Leppin and M Wilczek. [Capturing Velocity Gradients and Particle Rotation Rates in Turbulence](#). *Phys. Rev. Lett*, 125:224501, 2020. doi: 10.1103/PhysRevLett.125.224501.
- [213] C Meneveau and T S Lund. [On the Lagrangian nature of the turbulence energy cascade](#). *Phys. Fluids*, 6:2820–2825, 1994. doi: 10.1063/1.868170.
- [214] M Chertkov, A Pumir, and B I Shraiman. [Lagrangian tetrad dynamics and the phenomenology of turbulence](#). *Phys. Fluids*, 11:2394–2410, 1999. doi: 10.1063/1.870101.
- [215] B Lüthi, S Ott, J Berg, and J Mann. [Lagrangian multi-particle statistics](#). *J. Turbul.*, 8:N45, 2007. doi: 10.1080/14685240701522927.
- [216] H Xu, A Pumir, and E Bodenschatz. [The pirouette effect in turbulent flows](#). *Nat. Phys.*, 7:709–712, 2011. doi: 10.1038/nphys2010.
- [217] C Meneveau, T S Lund, and W H Cabot. [A Lagrangian dynamic subgrid-scale model of turbulence](#). *J. Fluid Mech.*, 319:353–385, 1996. doi: 10.1017/S0022112096007379.
- [218] F van der Bos, B Tao, C Meneveau, and J Katz. [Effects of small-scale turbulent motions on the filtered velocity gradient tensor as deduced from holographic particle image velocimetry measurements](#). *Phys. Fluids*, 14:2456–2474, 2002. doi: 10.1063/1.1472506.
- [219] F Toschi and E Bodenschatz. [Lagrangian Properties of Particles in Turbulence](#). *Annu. Rev. Fluid Mech.*, 41:375–404, 2009. doi: 10.1146/annurev.fluid.010908.165210.
- [220] M Cisse, H Homann, and J Bec. [Slipping motion of large neutrally buoyant particles in turbulence](#). *J. Fluid Mech.*, 735:R1, 2013. doi: 10.1017/jfm.2013.490.
- [221] S Parsa and G A Voth. [Inertial Range Scaling in Rotations of Long Rods in Turbulence](#). *Phys. Rev. Lett*, 112:024501, 2014. doi: 10.1103/PhysRevLett.112.024501.
- [222] T. Y. Hou and R. Li. [Computing nearly singular solutions using pseudo-spectral methods](#). *J. Comput. Phys.*, 226:379–397, 2007. doi: 10.1016/j.jcp.2007.04.014.
- [223] C C Lalescu and M Wilczek. [Acceleration statistics of tracer particles in filtered turbulent fields](#). *J. Fluid Mech.*, 847:R2, 2018. doi: 10.1017/jfm.2018.381.
- [224] A D Bordoloi and E Variano. [Rotational kinematics of large cylindrical particles in turbulence](#). *J. Fluid Mech.*, 815:199–222, 2017. doi: 10.1017/jfm.2017.38.

- [225] S Bounoua, G Bouchet, and G Verhille. [Tumbling of Inertial Fibers in Turbulence](#). *Phys. Rev. Lett.*, 121:124502, 2018. doi: 10.1103/PhysRevLett.121.124502.
- [226] N Pujara, G A Voth, and E A Variano. [Scale-dependent alignment, tumbling, and stretching of slender rods in isotropic turbulence](#). *J. Fluid Mech.*, 860:465–486, 2019. doi: 10.1017/jfm.2018.866.
- [227] A Pumir, E Bodenschatz, and H Xu. [Tetrahedron deformation and alignment of perceived vorticity and strain in a turbulent flow](#). *Phys. Fluids*, 25:035101, 2013. doi: 10.1063/1.4795547.
- [228] M Danish and C Meneveau. [Multiscale analysis of the invariants of the velocity gradient tensor in isotropic turbulence](#). *Phys. Rev. Fluids*, 3:044604, 2018. doi: 10.1103/PhysRevFluids.3.044604.
- [229] C Meneveau. [Lagrangian Dynamics and Models of the Velocity Gradient Tensor in Turbulent Flows](#). *Annu. Rev. Fluid Mech.*, 43:219–245, 2011.
- [230] P L Johnson and C Meneveau. [Predicting viscous-range velocity gradient dynamics in large-eddy simulations of turbulence](#). *J. Fluid Mech.*, 837:80–114, 2018. doi: 10.1017/jfm.2017.838.
- [231] L Zhao and H I Andersson. [Why spheroids orient preferentially in near-wall turbulence](#). *J. Fluid Mech.*, 807:221–234, 2016. doi: 10.1017/jfm.2016.619.